Short GAmma Ray Front Air Cherenkov Experiment (SGARFACE) analysis and cross-calibration with Whipple 10 m

by

Bagmeet Behera

A thesis submitted to the graduate faculty

in partial fulfillment of the requirements for the degree of

MASTER OF SCIENCE

Major: Astrophysics

Program of Study Committee:
Frank Krennrich, Major Professor
E. Walter Anderson
David A. CarterLewis
Steven D. Kawaler

Iowa State University

Ames, Iowa

2005

Graduate College
Iowa State University

This is to certify that the master's thesis of

Bagmeet Behera

has met the thesis requirements of Iowa State University

Major Professor

For the Major Program

TABLE OF CONTENTS

LIST OF TABLES

LIST OF FIGURES

ACKNOWLEDGEMENTS

I would like to take this opportunity to express my gratitude towards everyone I had the fortunate chance to work-with and learn-from at Iowa State University. I am greatly indebted for the guidance and help of Frank Krennrich who made my first attempt at research in Astrophysics a rewarding and enlightening experience. Many thanks to Frank Krennrich and Dave CarterLewis for their insightful advice and patience in explaining the details of the various aspects of gamma ray astronomy. A special thanks to Dave CarterLewis for helping me keep my research on track throughout this work. Thanks to Steven Kawaler for helping me out with Fortran codes time and again, for the wonderful learning experience in the course he taught, and for sharing his wisdom on practical aspects of graduate life. Many thanks to Walter Anderson for his delightful classes and the lively discussions, especially on the theoretical aspects of my research work, which lead me to appreciate the vast spectrum of modern physics. Thanks to Stephan LeBohec and Michael Daniel for all the help with codes and electronics during my research, and also for the wonderful company during my trips to Arizona.

To Asif Imran, Supriyo Das, Oleg Antipin, Maja Vuckovic, Qian Wang, Jhongbo Kang, Peter Peroncik, Shuang Jia, Jason Brown and all other friends here at Iowa State as well as all my colleagues, thankyou for making my stay here such a pleasurable and fruitful experience. Things would have been painfully dull, had it not been the many hours of discussion on problem sets and other fun things, the tennis, the movies and the frequent afternoon luncheons with many of you.

I am deeply indebted to my parents, Trilochan and Uma for standing by me and

supporting me in my every venture in life. Thanks to my brother, and Bhauja for the many moments of joy, and my new born niece. To Payeli, thankyou for putting up with me through all these years while I experimented with life; and to my friends back home in India, thanks for making life so enjoyable.

ABSTRACT

In this work the Short GAmma Ray Front Air Cherenkov Experiment (SGARFACE) instrument is calibrated against the Whipple TeV system as a reference to get a measure of the sensitivity of the instrument. The electronics gain of the system is quantified by the digital counts to photo-electron (d.c./p.e.) ratio, and is a measure of the system's response to a photo-electron collected by the photo-detectors. This ratio is required to reconstruct the number of Cherenkov photons collected by the telescope. The Cherenkov light density and angular distribution in the focal plane of an Imaging Atmosphere Cherenkov Telescope (IACT) allows us to reconstruct the atmospheric-shower parameters. Thus the d.c./p.e. is an important characteristic measure for the instrument. To calculate this measure, an event analysis software for the SGARFACE instrument is prepared, complete with image parameter calculation and event display. Then cosmic-ray events that simultaneously triggered both Whipple and SGARFACE are used to compare the charges (d.c.) given by both instruments. The known (previously calibrated) d.c. to p.e. ratio of the Whipple, is then used to get an estimate of the d.c./p.e. for SGARFACE.

The SGARFACE on the Whipple 10 m telescope, at Mt. Hopkins Arizona, is an instrument designed to detect bursts of low energy $\sim 250\ MeV$ gamma-rays which could be the result of the last stage of PBH evaporation. It has been taking data, concurrently with the Whipple TeV system for more than two years now. The existence of Primordial Black Holes and their evaporation mechanism can only be ascertained by detecting and identifying radiations that might be their signature. Previous attempts to measure the

radiation from PBH have put rough upper limits at various energies. SGARFACE is designed to search for PBH radiation at previously unexplored lower energies. The results of this work would enable the data taken by the instrument to be interpreted and analyzed to search for long duration bursts that might be signature of the final explosive stage of PBH evaporation.

CHAPTER 1. INTRODUCTION

The broad scientific objective of SGARFACE is to search for short duration ($\sim 0.1\ \mu s$ to $\sim 30\ \mu s$) bursts of $\gamma-$rays, emitted during the final stages of evaporating primordial black holes (PBH). In the late sixties and early seventies [19], it was shown that black holes of a wide mass range ($10^{-5}\ M_{\odot}$ upwards) could have been formed due to fluctuations in the very early universe. These are called Primordial Black Holes (PBH). It is supposed that PBH could have been formed with masses as small as $10^{-5}\ g$ (the Planck mass), forming at $10^{-43}\ s$ (Planck time) after the Big Bang, to masses as big as $10^{5}\ M_{\odot}$ forming at 1 s. Subsequently, since the path breaking discovery by Stephen Hawking in 1974 [20] that black holes should radiate thermally, a lot of interesting theoretical and observational work has been done in the field of black holes. With the discovery of Hawking radiation and the subsequent theoretical work, the fields of Quantum Mechanics, Gravitation and Thermodynamics have been brought together to shed some light on the interesting mechanism involved in the process of PBH evaporation.

In the observational field a number of attempts have been made to detect radiation from black holes. It is thought that PBH in their last stages of evaporation, should end their lives in an intense burst of $\gamma-$rays. The duration and the energy of this radiation, as well as the luminosity are governed by the particle physics models used, i.e. depend on the number of degrees of freedom available for particle creation. Thus to ascertain whether PBH actually exist and which model correctly explains the radiation from black holes, searches in multiple energy ranges, with the ability to detect bursts of $\gamma-$rays of variable durations are necessary. There have been a number of searches using ground-

based telescopes and satellite borne instruments to look for bursts of $\gamma-$rays, which might be the signature of this explosive final stage of a PBH. These experiments operated in various energy ranges and some upper limits in various energy ranges have been given (see Chapter 2). The Short GAmma Ray Front Air Cherenkov Experiment (SGARFACE) is an instrument designed to detect short duration (from 100 ns to about $\approx$ 35 μs) bursts of $\gamma-$rays. It has maximum sensitivity in the energy range of around 0.2 GeV to 10 GeV. It is installed on the Whipple 10 m Imaging Atmospheric Cherenkov Telescope (IACT), situated at Mt. Hopkins, Arizona. The SGARFACE instrument has been operational since late 2003, and has been taking data concurrently with the standard Whipple 10 m TeV system. This work involves the analysis of SGARFACE data, cross-calibration of SGARFACE with the Whipple 10 m, and a preliminary search for long duration bursts of $\gamma-$rays within a subset of the SGARFACE data.

The remaining part of this chapter gives a brief account on the theoretical background of PBH formation and evaporation, followed by a note on the scope and organization of this study.

1.1 Motivation

Under the current cosmic conditions, black holes forming by self-gravitating collapse, cannot have mass less than a few solar mass ($M_\odot$). Masses between $\sim$ 0.5 $M_\odot$ and $\sim$ 3 $M_\odot$, when cold can collapse to form stable white-dwarfs or neutron stars. To form black-holes the collapsing star needs to have an initial mass greater than $\sim 10 M_\odot to 25 M_\odot$. However during the very early universe PBH could have formed with considerably smaller masses. The arguments leading to the formation of PBH rely on fluctuation in the early universe.

1.1.1 Primordial black hole (PBH) formation

The essence of the argument given by Hawking in his 1971 paper [19], is presented below. If we accept that there should have been large random fluctuations on all length scales during the early universe, that were later damped out by some dissipation mechanisms. One could explain the highly isotropic nature of the present universe, and the existence of galaxies.

In the early universe if we consider a comoving volume V (assumed spherical for simplicity) with a density ρ. Then we would get

$$mass: \; M \; = \; V\rho$$

$$radius: \; R \; \sim \; V^{\frac{1}{3}}, \; since \, V \; \sim \; R^3$$

$$The \; Gravitational \; Binding \; Energy \; is \; given \; by: - U_g \; \sim \; \frac{GM^2}{R}$$

$$\implies U_g \; \sim \; \frac{GV^2\rho^2}{V^{\frac{1}{3}}} \; \sim \; G\rho^2 V^{\frac{5}{3}}$$

The kinetic energy due to expansion of matter (T_{exp}) in the same volume is given by

$$expansion \; rate \; = \; \dot{V}$$

$$velocity \; of \; expansion: \; v = \; \dot{R}$$

$$we \; had \, V \; \sim \; R^3, \; thus \, \dot{V} \; \sim \; 3R^2\dot{R} \; \sim \; R^2\dot{R}$$

$$thus \; we \; get \, v \; = \; \dot{R} \; \sim \; \frac{\dot{V}}{R^2} \; = \; \frac{\dot{V}}{V^{\frac{2}{3}}}$$

$$So \; finally, \; T_{exp} \; \sim \; Mv^2 \; = V\rho \left(\frac{\dot{V}}{V^{\frac{2}{3}}}\right)^2$$

$$\implies T_{exp} \; \sim \; V^{\frac{5}{3}}\rho \left(\frac{\dot{V}}{V}\right)^2$$

The potential energy due to relativistic pressure (U_P) would be of the order of the rest mass energy

$$U_P \; \sim \; Mc^2 \; = \; \rho c^2 V$$

If there would be random fluctuations in all length scales, it might be possible for many regions to have conditions such that the gravitational binding energy (U_g) could be greater than the Kinetic Energy of expansion (T_{exp}). Assuming that we are looking at such volumes the potential energy due to relativistic pressure (U_P) can be neglected compared to U_g if $U_g \gg U_P$. Thus

$$if\ U_g \gg U_P,\ We\ have\ G\rho^2 V^{\frac{5}{3}} \gg \rho c^2 V$$

$$\implies V^{\frac{2}{3}} \gg \left(\frac{c^2}{G\rho}\right)$$

$$\implies V \gg \left(\frac{c^2}{G\rho}\right)^{\frac{3}{2}};\ corresponding\ to\ a\ mass\ M\ of\ \left(\frac{c^6}{G^3\rho_\circ}\right)^{\frac{1}{2}}$$

Therefore given the conditions that U_g is able to overcome both the T_{exp} and the U_P effects, this volume would no longer expand with the rest of the universe but collapse gravitationally. The mass of this collapsed object would be of the order of $\left(\frac{c^6}{G^3\rho_\circ}\right)^{\frac{1}{2}}$, where $\rho_\circ$ is the density of the volume (or the universe) at the time of maximum expansion (of the volume in consideration). If the cosmological density at time t (the age of the universe) is also $\rho_\circ$, by comparing the density associated with black-holes with this density ($\rho_\circ$), we get an expression for the mass of the PBH formed as a function of the age of the universe, given by 't'.

$$M(t) \approx \frac{c^3 t}{G} \approx 10^{15}\left(\frac{t}{10^{-23}s}\right) g$$

According to this relationship, considering that gravitational collapse is essentially a classical process, the lower limit of $M(t)$ can be found by assuming that the first black-holes formed at the Planck time (t_P) of $\sim 10^{-43}s$. After this time we can consider gravitational collapse as a classical process and the arguments leading to the formation of PBH might be plausible. Thus with the smallest value of $t = t_P \approx 10^{-43}s$ we get a lower limit for the mass, $M(t_P) \approx 10^{-5}g$. On the other hand using the same expression at $t = 1s$ we would get $M(t = 1s) = 10^5 M_\odot$, which would correspond to the mass of black-holes thought to be at the center of galactic nuclei.

1.1.2 PBH evaporation and Hawking radiation

The above mentioned assumptions about the nature of early universe that would lead to the existence of PBH, as well as the mechanisms involved in the actual formation, can be put to test only by detecting such objects. It is believed that black-holes can radiate particles and photons. This mechanism is known as Hawking-radiation [20]. The mechanism of Hawking-radiation can be qualitatively explained by analogy with the production of particle anti-particle pairs (e.g. e^+e^-) in the presence of a strong electric field (see F. Halzen et al. [18]). In quantum mechanics, we deal with virtual particles such as e^+e^-, which are thought to be continuously created and destroyed. Ordinarily the virtual particle annihilates with its corresponding anti-particle within a very short time and are never detected. But in the presence of a strong electric field, the virtual particles can be separated and have a finite probability of tunneling through the quantum barrier, popping out as a real particle. In the same way, in a strong gravitational field such as one near the event-horizon of a black-hole, a virtual particle with positive energy can overcome the gravitational potential barrier and escape to infinity, where as the particle with negative energy would fall back into it to fill a negative energy state. The particle escaping to infinity would not need to annihilate with its anti-particle and will appear outside the black-hole as radiation coming from the black-hole.

In our electric field analogy we consider that the threshold electric field for particle formation would be

$$eE\lambda \; > \; 2m_e c^2$$

where $eE\lambda$ is the work done in separating the particle anti-particle pair by their Compton wavelengths (λ), and the right hand side is the rest mass energy of the pair, i.e. the energy required to create a pair of such species. The energy of a particle can be found by

$$E \; = \; kT \; \propto \; pc \; \propto \; \frac{\hbar}{\lambda}c \; \propto \; \frac{\hbar c^3}{2G}M^{-1}$$

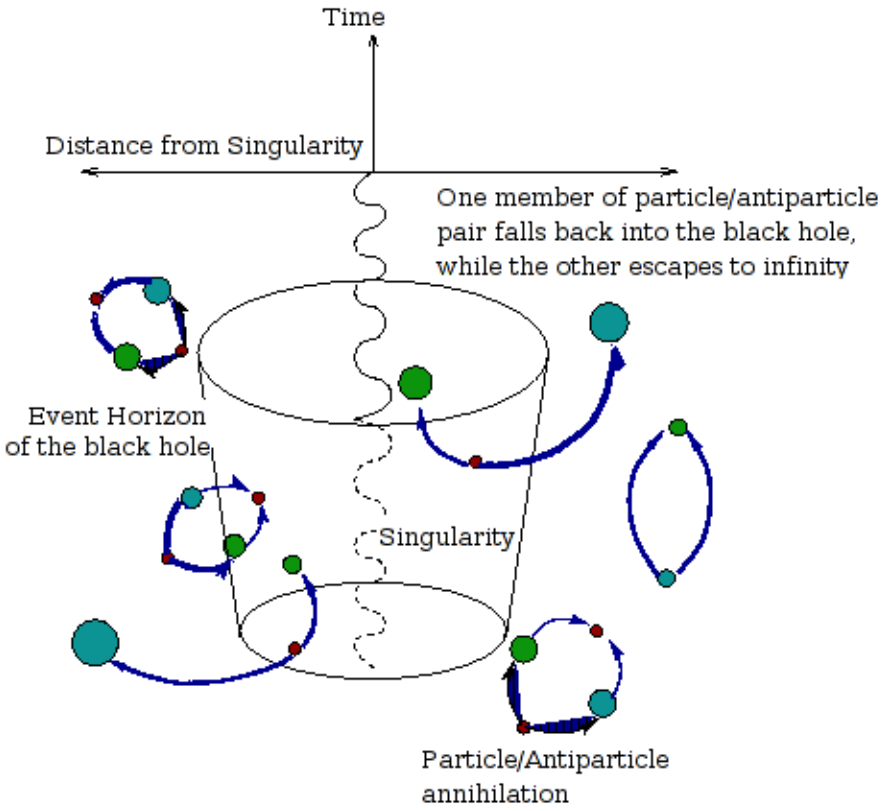

Figure 1.1 Schematic representation of Hawking radiation, in the presence of a strong gravitational field near a black hole

$$\implies T \propto \frac{1}{M};\ and \implies \lambda \propto M$$

Here the two relations for Energy $E = nkT$, (with n=1 for a single particle) and the relativistic energy momentum relationship $\frac{E}{c} = p$, where p is momentum have been used. The relation between λ and p is given by the de-Broglie relation $\lambda = \frac{\hbar}{p}$. Finally the Schwarzschild radius ($R_{sch} = \frac{2GM}{c^2}$) is taken to be the appropriate Compton wavelength λ for this situation.

From above we see that the temperature, T of an uncharged, non-rotating, radiating black-hole is inversely proportional to its mass. Which implies that as a black-hole radiates, it loses energy, thus its net mass decreases, which in turn increases its temperature (hence luminosity).

Thus the black body temperature $T \propto M^{-1}$, and the luminosity, L can be defined as the rate of mass loss of the black hole, $\frac{dM}{dt}$. Thus we get

$$L \equiv \frac{dM}{dt} = (4\pi\lambda^2)(\sigma T^4) \propto (M^2)(M^{-4}) = M^{-2}$$

Here the Luminosity is the area $(4\pi\lambda^2)$ times the flux, which is given by the Stefan-Boltzmann relation ($flux = \sigma T^4$).

The time scale for this radiation is obtained by integrating the result of the above equation.

$$\frac{dM}{dt} \propto M^{-2} \implies \int M^2 \, dM \propto \int dt \implies t \propto M^3$$

Putting in the units and constants we get

$$T \approx 100 \; MeV \left(\frac{10^{15}g}{M}\right)$$

$$L = 10^{20} \; erg \; s^{-1} \left(\frac{10^{15}g}{M}\right)^{-2}$$

$$t = 10^{10} \; yr \left(\frac{M}{10^{15}g}\right)^{3}$$

A proper calculation by Hawking shows that an uncharged, non-rotating black hole emits particles in the energy range (E,E+dE) at the rate (see Halzen et al. [18])

$$\frac{d^2N}{dtdE} = \frac{\Gamma_s}{2\pi\hbar}\left[exp\left(\frac{8\pi GME}{\hbar c^3}\right) - (-1)^{2s}\right]^{-1}$$

per state of angular momentum and spin. Here M is the mass of the black hole, s is the particle spin, and Γ_s is the absorption coefficient. Γ_s is in general a function of s, E and M, and represents the probability that a particle at this state incident on the black hole would be absorbed by it. The instantaneous emission would be a function of ME only, if $ME \gg 1$. Under such conditions the black body radiation of the black hole will be given by (obtained from a more detailed calculation than the one given from the above analogy)

$$T \approx 1.06 \times 10^{13} \left[\frac{1g}{M}\right] \; GeV$$

To see radiation at γ-ray energies, of $0.1 - 1GeV$ the black hole should have an initial mass range ($M_\circ$) below $10^{14}g$. The γ-ray emission from black holes would appear in two different forms. One would be the result of emission of black holes (with $M < M_\circ$) during their normal evaporation life times (except the explosive final stage), which might appear as a relatively low but more or less uniform component of the diffuse γ-ray background. The second would be the explosive and short signature from the final stage.

1.1.3 Final stage emission for different models

The rate of mass loss of a black hole can be described as

$$\frac{dM}{dt} = \frac{-\alpha(M)}{M^2}$$

where the term $\alpha(M)$ denotes the degrees of freedom available for particle creation at any instance. Integrating the above equation gives the time required for the complete evaporation of a black hole with a certain initial mass. As the black hole evaporates and loses mass, its temperature rises and subsequently more energy (degrees of freedom) is available for particle creation, as each higher energy threshold is attained.

However the value of $\alpha(M)$ is also highly dependent on the particle physics model used. The degrees of freedom for particle creation is only well known for energies achievable using current accelerators. These energies are far less than the energies under consideration here. The value of $\alpha(M)$ is derived by extrapolating to the energies reached in the final stages of evaporation, using some particle physics model and the known behavior at accelerator energies. To get an idea about the luminosity, energy of emitted radiation and the duration of the emission in the final stage, we consider two extreme models, the standard model and the Hagedorn model.

1.1.3.1 Standard Model

According to the standard model, the value of $\alpha(M)$ increases smoothly with temperature as each rest mass energy threshold is crossed. Thus with a constant maximum number of degrees of freedom, as suggested by the standard model, α reaches a constant limiting value at very high energies ($T \approx 100GeV$), equal to $\alpha \geq 7.8 \times 10^{26} g^3 s^{-1}$ (as recently recalculated by Halzen et al. [18]). With this value, the final explosion is predicted to release a total energy of $\approx 10^{28} erg$, lasting for about 1 second dominated by photons of average energy of $1TeV$. This gives us a rough upper limit for the duration as well as the energy of the photons. However it should be pointed out that these predicted values can only be true if the standard model is still valid at these very high temperatures.

1.1.3.2 Hagedorn Model

The other extreme model is the Hagedorn model which is a statistical thermodynamics model. According to this model the particle creation at high energies can only be predicted by taking into account all the resonances (even the undetected ones) of all possible particles that can be formed at a given energy. This model gives a basic postulate valid in the limit of very high energies, that says that there are lumps of hadronic matter, called fireballs defined (in a boot-strap manner) as

> *''a statistical equilibrium (hadronic black−body radiation) of an undetermined number of all kinds of fireballs, each of which, in turn, is considered to be"*

Sparing the details (see R. Hagedorn [16]) the essence of the model is that the mass spectrum (or equivalently $\alpha(M)$) behaves exponentially when the energies are high. In other words the number of degrees of freedom N, varies with particle mass as

$$N \approx m^{-\frac{5}{2}} exp\left(\frac{m}{T_\circ}\right)$$

where m is the particle mass, and $T_\circ$ ($\approx 160\ MeV$) is the asymptotic upper limit for the temperature of a fireball. The temperature $T_\circ$ is the highest possible temperature, and is similar to a "boiling point" for hadronic matter, in whose vicinity the creation of particle increases explosively such that the temperature cannot increase any more. In the context of PBH evaporation, this means that as the black hole (considered as a fireball) evaporates, the degrees of freedom for particle creation starts to grow exponentially as the temperature approaches $T_\circ$. In the final stage the temperature might reach a value so near to $T_\circ$ that the remaining mass of the PBH will evaporate explosively in a small time giving out highly energetic radiation. Calculations show that PBH with initial mass a few less than $10^{14}\ g$, will be in this explosive final state at the present epoch, and may radiate away as much as $6 \times 10^{34}\ erg$ within a time of 100 ns. A significant fraction of this energy will be in the form of γ-ray photons with an average energy of 250 MeV.

Apart from the above two extreme models there are some intermediate models, such as the inclusion of quark gluon plasma (QGP) phase transition effect in the fireball model, see Cline et al. [6, 7]. According to this model, as a radiating PBH evaporates and approaches the quark gluon phase transition temperature, the QGP interaction around the evaporating PBH might result in an expanding fireball of hadronic matter (mostly pions). After the pions in the initial fireball decay, it converts to a fireball consisting of photons, leptons and baryons. The photons would be trapped in the fireball, until the photon optical depth is thin enough to allow their escape. On reaching this optically thin stage the photons would be released as a short γ-ray burst with duration of the order of milliseconds. Some bursts less than around 100 ms duration have been found in the BATSE data (see Cline et al. [7]), which might be consistent with such phenomena.

1.2 Scope and organization of this work

We thus see that depending on which particle physics model is actually applicable at high energies, the detection of burst of γ-rays from the final stage emission of PBH, would require detection over a wide range of energies as well as duration of bursts.

The SGARFACE instrument is intended to extend the scope of such burst searches to previously unexplored energy and duration ranges. The two major objective of this work are (1) to prepare a data-analysis software that does a single-time-scale [1] analysis, of events detected by the SGARFACE instruments, and (2) to cross calibrate the SGARFACE instrument with the Whipple 10 m TeV instrument using coincident cosmic-ray events. After these two objectives are satisfactorily achieved a subset of the SGARFACE data collected till date, would be analyzed to look for events that might be due to long duration bursts of γ-rays. It should be pointed out here that to get any reasonable estimate for upper limits to the flux from PBH at SGARFACE energies, two years (or more) of SGARFACE data has to be analyzed in detail. Such an analysis would be beyond the scope of this work, and the intention here is to prepare the necessary analysis and software tools to be able to do so in the near future.

The organization of the remaining chapters is as follows. Chapter 2 gives a brief historical perspective on the development of TeV astronomy and the recent advances made in the field of γ-ray astronomy. It also gives an account of the searches for PBH evaporation made in the γ-ray regime as well as other frequencies, with various instruments. Readers familiar with the subject can safely skip chapter 2 without any loss of continuity. Chapter 3 describes the SGARFACE instrument and its electronics; followed by the results of simulations of burst images which would possibly be detected by the SGARFACE instrument, done by Krennrich et al. [29]. The bulk of the work done by the author is

[1] The term "single time scale" here refers to the number of data samples taken together as one data unit. The data samples from SGARFACE instrument can be integrated over different time scales and analyzed, to detect extended air showers at various energy ranges. See LeBohec et al. [32] for details.

described in detail in chapters 4 and chapter 5. The analysis technique for SGARFACE events is explained in chapter 4. In chapter 5 the method used to cross-calibrate the two instruments is explained. The results of this work, the suggested improvements and possible future enhancements are described in the concluding chapter. An outline of the technique to search for long duration bursts of γ-rays within SGARFACE data is also given in the concluding chapter.

CHAPTER 2. BACKGROUND

High energy astronomy and in particular Very High Energy (VHE) γ-ray astronomy with ground based telescopes is a relatively new field of science. Starting with the first reliable detection of cosmic γ-rays from space in 1961, by the Explorer 11 satellite (Kraushaar et al. [27]); to the new generation IACT arrays like VERITAS (under construction, Krennrich et al [31]), γ-ray astronomy has come a long way, and is now a well established field. The high energy Universe is being probed by a variety of instruments, at various energy regimes. Cosmic gamma ray energies cover a wide range of energies from $\sim$ 500 keV to at least 100 TeV. Based on the instruments used, the study of this high energy radiation can be divided into two broad categories, viz. space-borne and ground-based. Space-borne γ-ray astronomy covers energy ranges from 500 keV to around 30 GeV, and is accomplished by satellite and high altitude balloon experiments. The other domain of energies greater than above 100 GeV is covered by ground-based γ-ray astronomy through atmospheric Cherenkov telescopes and air-shower arrays. In this energy range an incident γ-ray interacts with a nuclei in the atmosphere to produce an electromagnetic cascade, which in turn produces Cherenkov light beamed along the direction of the primary γ-ray. This Cherenkov flash can be detected by air Cherenkov telescopes, and the 2-dimensional images formed at the focal plane of the telescopes, can be analyzed to reject the background due to cosmic-ray events.

In this chapter a brief history of the development of observational γ-ray astronomy is given, with an emphasis on the search for bursts of γ-rays (for a detailed history of the general field of γ-ray astronomy, see Schönfelder, V. [45]). A short description of the

underlying physics of IACTs is given in section 2.2, followed by the results of searches for last stage PBH evaporation.

2.1 History of gamma ray astrophysics, and bursts

The earliest attempts to detect γ-rays, as a component of cosmic radiation, were made in the 1940s and early 1950s, using balloon and rocket experiments (Hulsizer et al. [23]; Perlow et al [42]; Rest at al. [44]). Though these attempts involved tremendous amount of effort and ingenuity, unfortunately the low sensitivity of these instruments and the high back-ground rate of cosmic-rays, made it virtually impossible to get any reliable detection of γ-rays. However these early attempts made essential contributions to the development of this field.

Most of the early milestones in observational γ-ray astronomy were made with satellite-borne experiments. The first reliable detections of γ-rays from space were made by the Explorer 11 satellite in 1961 (Kraushaar et al. 1965 [27]), and the by OSO-III in 1968 (Kraushaar et al. 1965 [28]).

The cosmic γ-ray burst phenomena was discovered around 1967, by the VELA satellites, of the U.S. Department of Defense. These satellites were looking for violation of the Nuclear Test Ban Treaty, and hence the results of these detections of Gamma Ray Bursts (GRBs) from outer space, was made public much later in 1973 (Klebesadel et al [25]).

In the 1960s and early 1970s several satellites with omni directional scintillation γ-ray detectors, were launched, e.g. the Apollo 15. The first direct evidence for specific γ-ray lines associated with solar flares were obtained, in 1972, with the OSO-VII satellite experiment (Chupp et al. [5]). This experiment recorded emission for strong annihilation (511 keV), neutron capture lines at 2.23 MeV, and nuclear interaction lines from carbon and oxygen nuclei (4.4 and 6.1 MeV).

SAS-2 launched in 1972 ($E > 30\ MeV$), and COS-B launched in 1975 ($E > 70\ MeV$) provided the first accurate maps of γ-ray emission from the Milky Way (Kniffen and Fichtel [26]). These were also the first instruments to give source detections, the strongest of which were the Crab and Vela pulsars, and an unknown source (at that time) called Geminga, which was later identified as a pulsar (Halpern and Holt [17]).

There were some other satellite missions between 1979 and 1990, e.g. the HEAO-C (Mahoney et al. [38]), SMM (Leising and Share [36]) and SIGMA which observed in the hard X-ray and soft γ-ray regimes.

The period after 1990 is dubbed by some, as the "golden epoch" for γ-ray astronomy. Two important satellite experiments operational during this period were the French SIGMA telescope on board the French/Russian GRANAT mission, and the Compton Gamma Ray Observatory (CGRO). SIGMA had unprecedented angular resolution of 10 arc minutes, and observed mainly around 100 keV, the transition region between X-ray and γ-ray. It detected around 30 sources mostly around the Galactic Center (Vargas et al. [48]). These sources were from a variety of objects and most of these were highly variable. Some of the objects were the so called X-ray novae, which are believed to be accreting binaries with a stellar black hole, producing X/γ-ray emissions with huge outbursts, and the so called "Galactic micro quasars" which have a double-sided jet like structure emanating from a compact cone visible at radio frequencies.

The CGRO, operational from April 1991 to June 2000, had four instruments, one of those being the Burst And Transient Source Experiment (BATSE). As the name suggests this experiment was designed primarily to detect γ-ray bursts and get directional information of such events (Fishman et al. [14]). Gamma-ray bursts is a term used for short duration (ranging from a few ms to a few 100 s), but intense flashes of γ-rays that occur in BATSE at a rate of approximately one per day and come from all directions in the sky. The BATSE detected 2704 GRBs, in its operation period of nine years.

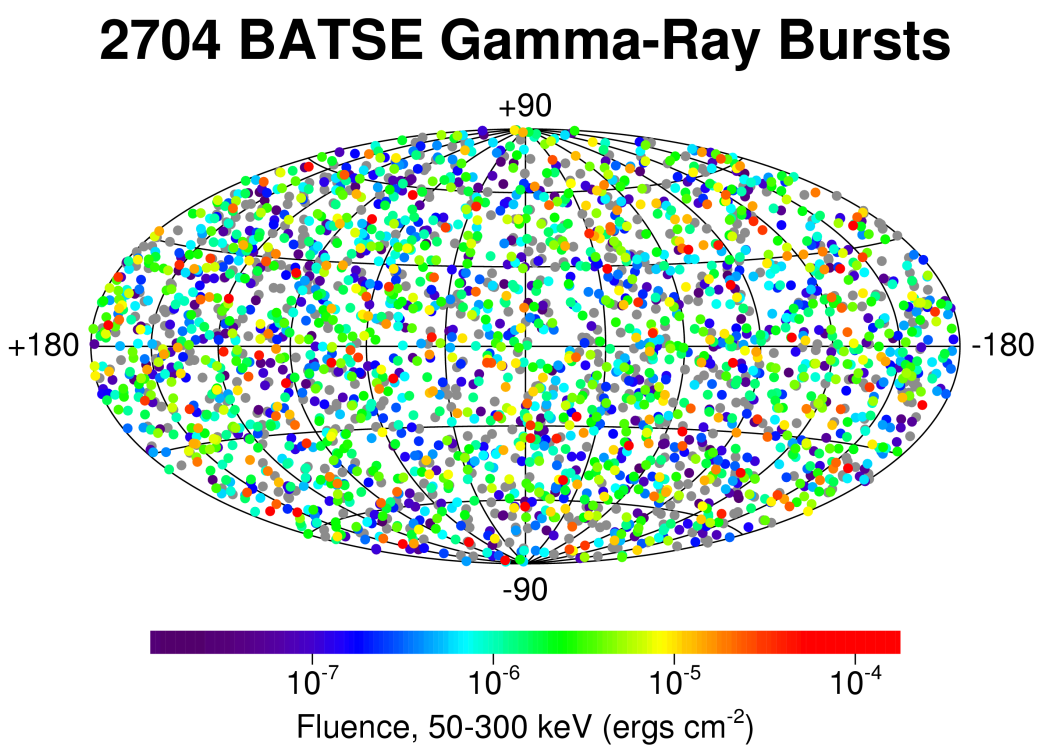

Figure 2.1 The locations of a total of 2704 Gamma-Ray Bursts recorded with the BATSE on board NASA's CGRO during the nine-year mission, from [http://www.batse.msfc.nasa.gov/batse/grb/skymap/].

In 1997, the Italian/Dutch Beppo-Sax satellite made a break through in the study of GRBs by successfully observing the X-ray afterglows from a few burst sources (Costa et al. [9]). Subsequently there were observations in the optical and in some cases radio wavelengths, that clearly established the extragalactic origin of the GRB sources (Kouveliotou [24]). Another breakthrough in 1999 was the first optical observation of GRB 990113 burst while it was still in progress (Akerlof et al. [1]). Multi-wavelength observations of GRB sources not only help in establishing the distance of these sources, but also help to estimate the total energy output of these sources.

Currently operational satellite experiment SWIFT (see Gehrels [15]), is continuously monitoring the sky for GRBs, while making it possible for other space and ground based

telescopes to do quick follow up observations of the burst sources at other wavelengths. The GLAST experiment scheduled to be launched in August 2007 (see McEnery et al. [39, 40], vonKienlin et al. [49]), will further augment the study of the gamma-ray sky.

In the field of ground based observations, air shower arrays, and air Cherenkov telescopes (ACTs) are used to detect γ-ray, indirectly through the Cherenkov flash of the shower of secondary particles. Air shower array are not discussed here (see R. A. Ong [41] for an overview of different instruments). The first direct images of Cherenkov light from air showers, was recorded by Hill and Porter [21] in 1960, using an image intensifier camera system on a small mirror. This instrument used photographic films, but its slow read out and limited size, made such instruments impractical to be mounted on large optical telescopes. These photographic instruments at the focal plane have been replaced by arrays of photo multiplier tubes (PMTs) in modern ACTs. A major break through was made in 1989 in the field of TeV γ-ray astronomy, by the Whipple collaboration (see Weekes et al. [51]), with the first definite detection of TeV gamma rays from the Crab Nebula using the Cherenkov-imaging technique developed by Hillas [22]. Since then a lot of advances have been made in IACT γ-ray observations. Presently there are a number of air Cherenkov telescopes in operation and under construction (table 2.1 gives a partial list of ACT experiments).

2.2 TeV gamma rays, Imaging Atmospheric Cherenkov Telescopes (IACT), bursts

Satellite experiments have been used to detect γ-rays below $\sim 40\ GeV$, but at higher energies the low flux and limited collection area of these instruments severely limits their use. Compounded to this as energies increase, the cascade of secondary particles cannot be contained within the limited size of the satellite detectors, thus rendering it difficult to accurately calculate the primary γ-ray energy. Above $\sim 50\ GeV$, the atmosphere acts as a

Table 2.1 Previously existing, existing and planned ACT and next generation ACT arrays (last three), Adapted from Weekes [52]

Experiment	Location	Elevation (km)	Collectors	Mirror area (m^2)	Pixels/Camera	Energy (GeV)
Whipple	Arizona, USA	2.3	1	75	467	250
GT-48	Crimea, Ukraine	0.6	2	27	37	1000
CANGAROO	Woomera, Australia	0.2	1	75	256	400
SHALON	Tien-Shan, Russia	3.3	1	10	144	1000
HEGRA	La Palma, Spain	2.2	6	9	271	500
CAT	Pyrenees, France	1.6	1	18	600	250
TACTIC	Mt. Abu, India	1.3	4	10	349	500
HESS	Gamsberg, Namibia	1.8	4(16)[a]	100	900	50
VERITAS	Arizona, USA	1.5	4(7)[1]	100	499	50
CANGAROO-III	Woomera, Australia	0.2	4	75	577	50
MAGIC	La Palma, Spain	2.2	1(2)[1]	236	576	30[b]

[a]The first number is the number of telescopes existing or under construction, and the number in parentheses is the final number of telescopes planned to be constructed

[b]Less than 30 GeV is the target sensitivity for this instrument.

calorimeter and interaction of the primary γ-ray with the atmosphere produces extended air showers (EAS), of secondary particles (via pair-production) and secondary photons (via bremsstrahlung). The primary γ-ray interacts with a nucleus in the atmosphere and produces a particle anti-particle pair (e^- and e^+). These particles are relativistic and are strongly beamed in the primary γ-ray direction. These secondary particles produce secondary γ-ray photons via bremsstrahlung, and these in turn can produce more particle-antiparticle pairs see figure 2.2 (a). This process continues and the shower size (measured by the number of secondary particles, mostly e^-) increases geometrically, until the mean energy of the particles falls below the critical energy of $\sim 85\ MeV$, where ionization loss is a more efficient way to lose energy than bremsstrahlung. After this point the shower size is past its maximum size, and decreases exponentially, see figure 2.2 (b).

The EAS starts to form typically around 10 *to* 15 km altitude and for a 1 TeV primary γ-ray reaches shower maximum at $\sim 8\ km$. The particles in the EAS move at a speed greater than the speed of light in air, and produce Cherenkov photons. Maximum Cherenkov photons are produced within a few km lengths around the shower maximum. These Cherenkov photons can be detected by ACTs in a $\sim 150\ m$ radius from the shower core, thus giving a collection area of the order of $100,000\ m^2$ for ACTs, see figure 2.2(c). The opening angle for Cherenkov radiation is around 1.3°, at sea level, and decreases with the density of the medium. The imaging technique (Hillas [22]) makes it possible to exclude most of the cosmic-ray events, which are on the average 500 times more numerous than γ-ray events. In the case of bursts of γ-rays incident on the top of the atmosphere, even if the energy of individual primaries is $\sim 100\ MeV$, the collective glow of the Cherenkov flash from the wave front of γ-rays, can still be detected by an IACT (see section 3.3).

Simulations are an essential part of ground based γ-ray astronomy, since there are no particle-accelerators in space to let us study EAS and images formed from primary γ-rays at known energies. It is therefore the only way to predict the nature of the images that will

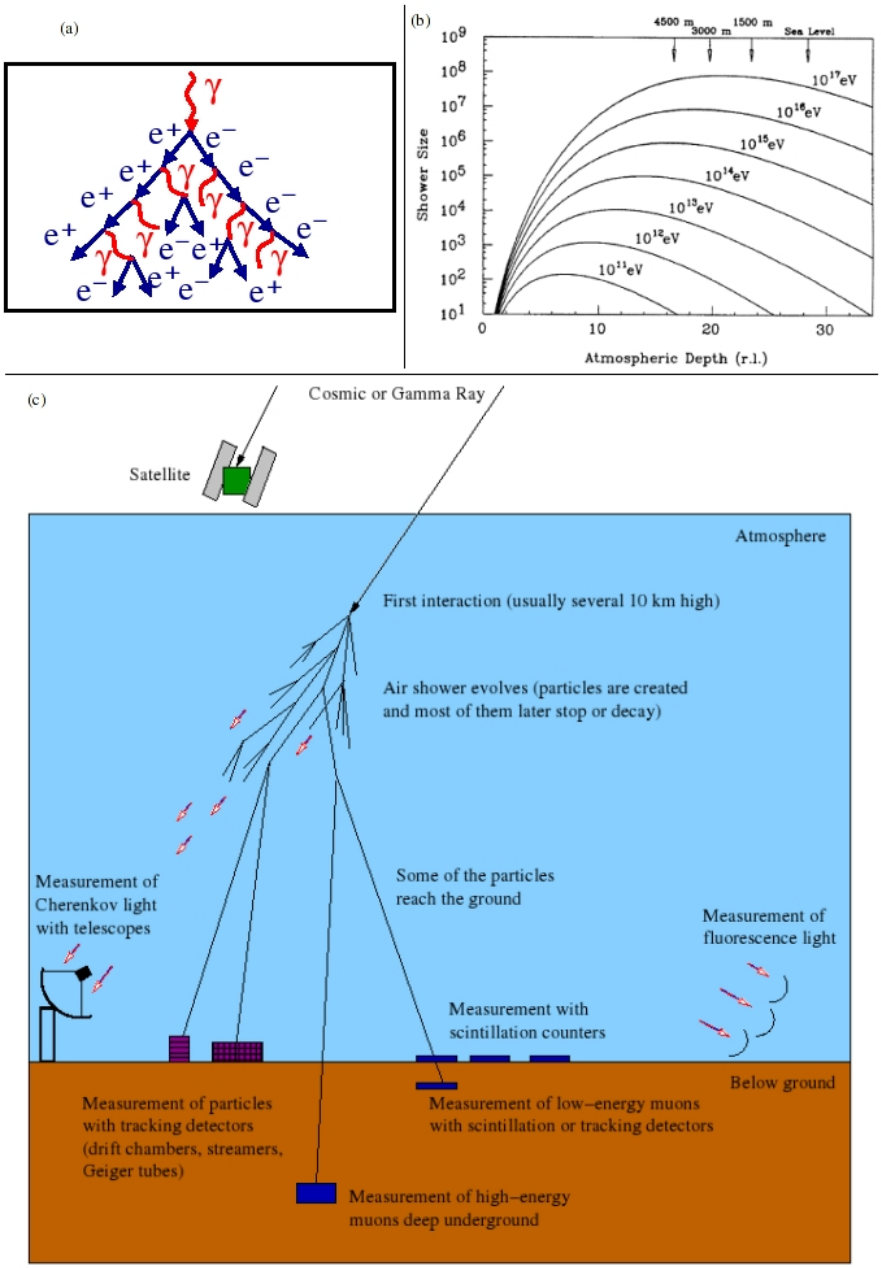

Figure 2.2 (a) Development of an extended air shower from a γ-ray. (b) The shower size versus the depth in the atmosphere, given in radiation length (r.l.) Radiation length in air is $\sim$ 37 gcm^{-2}, and atmospheric depth at sea level is $\sim$ 28 $r.l.$ (c) Methods of measuring cosmic and gamma rays (Figure (a) and (c) from Schroedter [46], and (b) from Ong [41]).

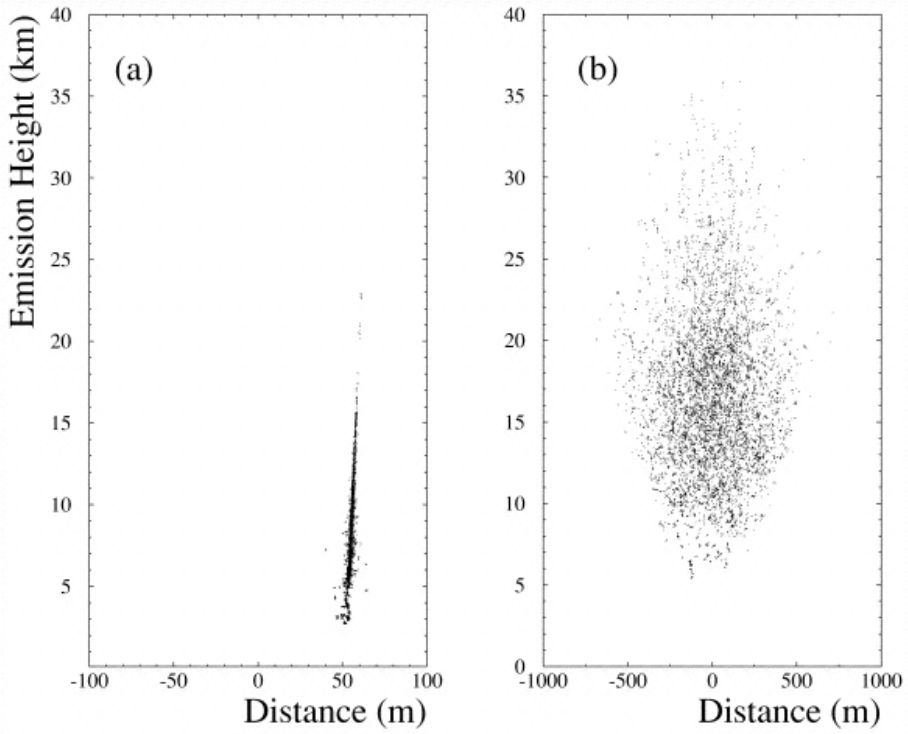

Figure 2.3 Figure from Krennrich et al. [29]. (a) Longitudinal and lateral distribution of the electromagnetic component of a single gamma-ray-initiated shower of 1 TeV. The dots indicate the origin of emission of individual Cerenkov photons that are detected with a Whipple-type telescope. (b) A multi-gamma-ray-initiated shower. For the multi-gamma-ray-initiated shower, Cerenkov photons that originate up to 600 m away in the lateral scale can contribute to the Cerenkov flash detected in a telescope.

be seen with an IACT. Electromagnetic shower physics and Cherenkov photon production is quite well understood, and hence Monte-Carlo simulations are extensively used to model and study the images formed in the focal plane instruments due to cosmic/γ-rays at different energies. An example of such a simulation result is shown in figure 2.3, for a single γ-ray initiated shower, and for a shower formed due to a front of γ-rays.

2.3 Search and detection of PBHs

To conclude this chapter the results for the various searches for PBH are given briefly.

2.3.1 Satellite experiments

Though earlier satellites like the SAS-2 might have been able to detect some bright burst (that is, from the relatively nearby regions of the galaxy) from PBH evaporation, here the results from the searches for bursts in the BATSE and Energetic Gamma-Ray Experiment Telescope (EGRET) data, are given. Both these instruments were on-board the CGRO, but whereas EGRET might have been sensitive to sub-microsecond bursts, the BATSE events were typically of the order of 1 *second* or greater. To remind the reader, the standard model of particle physics predicts bursts of $\sim 1\ TeV$ energies, of $\sim 1\ s$ duration from final stage PBH evaporation, where as the Hagedorn model predicts $\sim 250\ MeV$ γ-rays with the typical duration of 0.1 μs. The EGRET data was searched for sub-microsecond bursts by Fichtel et al. [12], and they found no evidence of such bursts. Based on this, they put an upper limit for PBH decays, at $5 \times 10^{-2}\ pc^{-3}yr^{-1}$, for the Hagedorn model. In a study by Cline et al. [6, 7] on the data from BATSE, it was pointed out that there were a distinct class of GRBs that had an increasing hardness with decreasing time duration, below a few hundred milliseconds. They suggested that this should be the expected result from PBH evaporation via a QGP fireball model. They however did not claim that any PBH were observed, and only suggested that such behavior should be studied in detail by future experiments.

2.3.2 Air shower arrays and air Cherenkov telescopes

Air shower arrays have been used to search for burst of Ultra High Energy γ-rays, of duration around 1 s. These instruments operate above $10 - 50\ TeV$, and upper limits have been given by Alexandreas et al (in 1993, [2]), and Amenomori et al (in 1995, [3]) as $6.1 \times 10^5\ pc^{-3}yr^{-1}$ for $1s$ duration, and $4.6 \times 10^5\ pc^{-3}yr^{-1}$ at $10TeV$ for 1 s duration respectively (for the standard model).

In 1978, Porter and Weekes [43], used two systems of separated atmospheric Cherenkov

telescopes to search for coincident high energy γ-rays. In one system, four 1.5 m reflectors with maximum separation of 2.5 km were used, and in the other two reflectors of $70-80$ m^2 area were used with a separation of 400 km. Using the Hagedorn model they put an upper limit for PBH evaporation of 0.04 $pc^{-3}yr^{-1}$ events within the galaxy, and according to standard model a limit of 7×10^5 $pc^{-3}yr^{-1}$, based on zero coincidences. Later in 1998 Connaughton et al. [8], used 4 years of archival data (between 1988 - 1992) from the Whipple 10 m telescope to search for 400 GeV gamma-ray bursts on a 1 s time scale. Based on a null result they gave an upper limit of $3 \pm 1 \times 10^6$ $pc^{-3}yr^{-1}$ for the standard model.

2.3.3 Searches at other frequencies

Apart from γ-rays, it has been suggested that detectable radio and optical emission can also be produced during the last stage evaporation of PBH (see Halzen et al.[18] and the references therein). According to this model, in the presence of an ambient magnetic field, the relativistically expanding charged-particle shell from the last explosive stage could be braked and thus produce electromagnetic radiation. However the conditions for such pulse production is highly model-dependent. Null results from such searches give the lowest upper-limit of 2×10^{-7} $pc^{-3}yr^{-1}$, for the standard model plus radio emission, and 0.3 $pc^{-3}yr^{-1}$ for standard model plus optical emission.

In this work, the Hagedorn model is considered, to prepare the analysis tools to search for bursts of γ-rays from final stage of PBH evaporation, within the SGARFACE data. Here, it should be pointed out that the detection or conversely the non-detection of random micro-second bursts would not be a decisive evidence for the presence or absence of PBH, since microsecond bursts could also be produced by certain GRB phenomena, and other astrophysical objects. However the detection of even few microsecond or sub-microsecond bursts, having a consistently small range of duration and a well defined range of energy would be a strong evidence for PBH detection. This is because PBHs

evaporating at the present epoch, would have a specific mass, and hence would correspond to a narrow range for the energy and duration for the bursts of γ-rays emitted in its final stage. By combining data from SGARFACE with GLAST data, which is predicted to be sensitive to bursts between 100 μs to several ms, and further results from the archival BATSE data; in the near future the time scale regime between 100 ns to 1 s can be fully covered with unprecedented sensitivity.

Detail study of both, the energy distribution and the time-profile has to be done to constrain any detected bursts as per the particle physics model. For this different techniques and observation at various energies have to be used.

CHAPTER 3. SGARFACE, THE EXPERIMENT

The imaging atmospheric Cherenkov technique has made it possible to detect very high energy (VHE) γ-rays using ground based instruments, and advanced our understanding of the TeV sky. Correspondingly in the last decade (first detection of TeV source in 1989, by Weekes et al. [51]) we have witnessed tremendous development in the field of Imaging Atmospheric Cherenkov Telescopes (IACT). Apart from detection of TeV sources, the imaging technique could be used for other applications such as detecting bursts of γ-rays using single or array of IACTs. The last stages in the evaporation of a PBH could involve explosive mechanisms, and might result in ≈ 0.1 μs or longer duration bursts of γ-rays, with individual γ-ray energies around 250 MeV or so. Though such γ-rays are typically too low in energy to be individually detected by IACTs, the combined cherenkov photon yield of numerous such γ-rays incident within a short period of time would be detectable. This possibility was first suggested by Porter and Weekes [43]. They had attempted to detect simultaneous flashes, by using two telescopes with single Photo Multiplier Tube (PMT) at the telescope focus, with a telescope separation of around 400 km. More recently in Krennrich et al. [29], it is shown that a single modern IACT like the Whipple 10 m, can be used to detect multiple γ-ray initiated showers with primary energies as low as 100 MeV, when equipped with the appropriate trigger electronics.

The SGARFACE instrument is installed on the Whipple 10 m IACT, located at Mt. Hopkins, Arizona. Thus the physical telescope structure, optics, and the initial focal-plane electronics are the same for the standard Whipple 10 m instrument and

Figure 3.1 Whipple 10m and its focus-box. Left:Whipple 10m. Right: The 490 pixel camera in the focus-box, inner 379 PMTs are 0.5 inch in diameter, and outer 111 are 1 inch in diameter. The light-cones (absent when this picture was taken) are usually attached in front of the inner PMTs (figure taken from [11], Page 37).

the SGARFACE instrument. Hence it is possible to cross-calibrate the SGARFACE instrument with the standard Whipple 10 m electronics using cosmic-ray events simultaneously detected by both instruments. The SGARFACE electronics is separated from the standard Whipple TeV electronics using a splitter summer circuit, which is the first component of the SGARFACE electronics. This chapter gives a short description of the Whipple 10 m telescope, the SGARFACE instrument, and the imaging of potential burst like events.

3.1 The Whipple 10m gamma ray telescope

The Whipple 10m telescope was constructed in 1968, and has undergone many transformations since. Descriptions of the telescope with its different upgrades can be found in various sources such as [50, 4, 37, 13], etc. The telescope structure and optics have remained almost unchanged over the years, but the focal plane instrument with its PMTs has changed many times in the last couple of decades.

The Whipple 10m has a spherically shaped reflector of the Davies-Cotton design, with

249 spherical mirror facets, with a maximum diameter of 10m, covering a surface area of ≈ 75 m^2. The field of view (FOV) is $\approx 2.4°$. There is an inherent time-spread, between light rays incident on the edge of the telescope and the light-rays incident at the center of the telescope, as shown in figure 3.2.

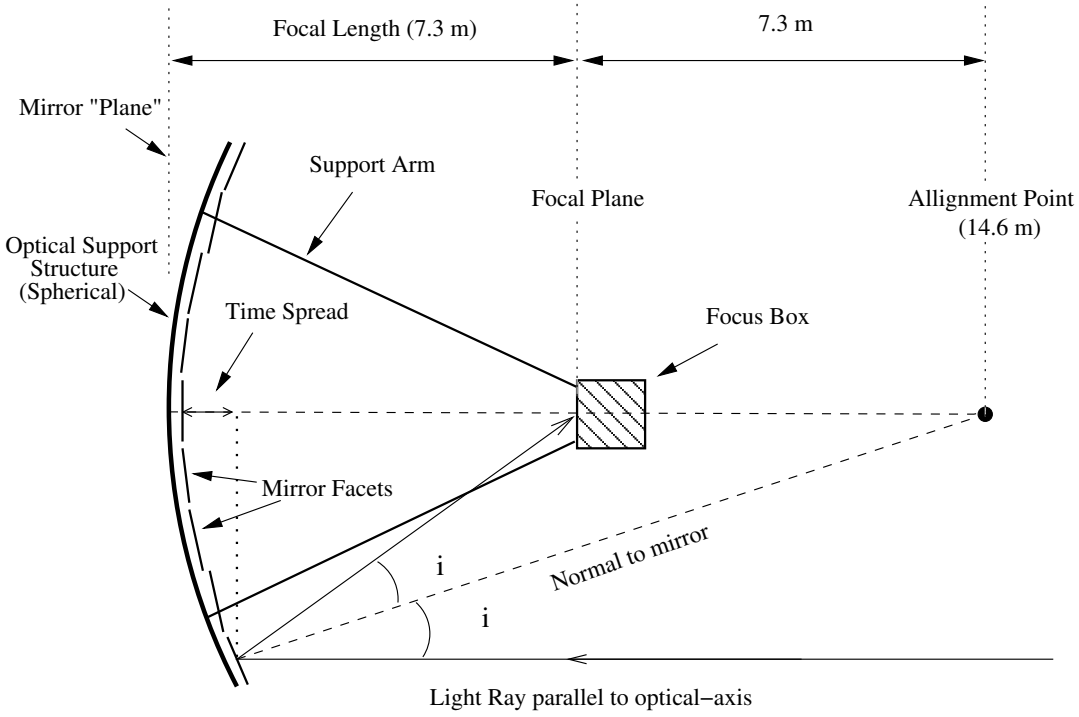

Figure 3.2 2-D Ray Diagram of Whipple 10m with mirror-facets, showing the Davis-Cotton configuration; also note the time-spread between the photons reflected at the center and edge of the optical-structure (figure taken from [11], Page 37).

Since the development of the imaging technique, which was pioneered by the Whipple Collaboration using the Whipple 10 m in 1989; the camera has been improved by increasing the number of PMTs, as well as reducing the pixel size. This improves the angular resolution of images measured in the focal plane. At present the camera has 379, 0.5 inch PMTs arranged in a hexagonal grid. The SGARFACE channels are constructed by summing up the Whipple tubes in Hexagonal sets of 7 neighboring tubes, see figure 3.3. the focal-plane instrument thus defined, covers a total diameter of $\approx 2.4°$ (field of

view in the sky), with center-to-center SGARFACE pixel spacing of $\approx 0.3^{\circ}$.

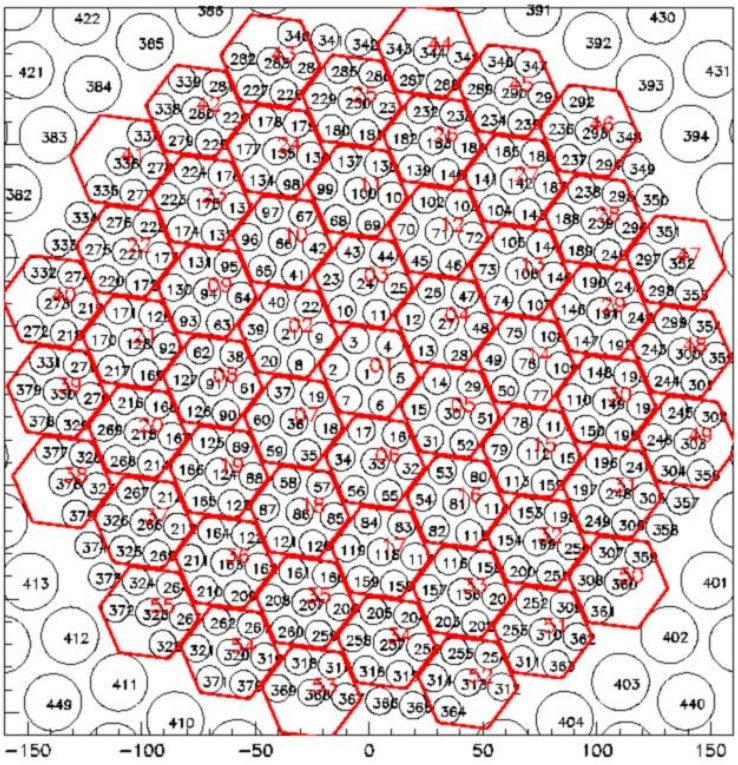

Figure 3.3 The mapping of the 379 tubes of the Whipple 10 m camera to form 55 SGARFACE pixels. The small circles are the actual Whipple PMTs, whereas the hexagons constitute the SGARFACE pixels. Figure from Frank Krennrich (private communication).

3.2 SGARFACE electronics

The individual PMTs in the focal-plane instrument are usually run with a voltage gain $\sim 10^6$ (see Krennrich et al.[30], LeBohec et al. [32]), and the signal from PMTs is transferred via $\approx$ 70 ft length of RG-58 cables. The SGARFACE electronics essentially has three electronic-hardware units, viz. the splitter-summer module, the Multi-Time-Scale (MTS) discriminator, and the Pattern Sensitive Coincidence (PSC) unit, along with the software to control these units, see figure 3.4. These sub-systems and their respective

functions are described in brief here. For a more detailed description see LeBohec et al. [32].

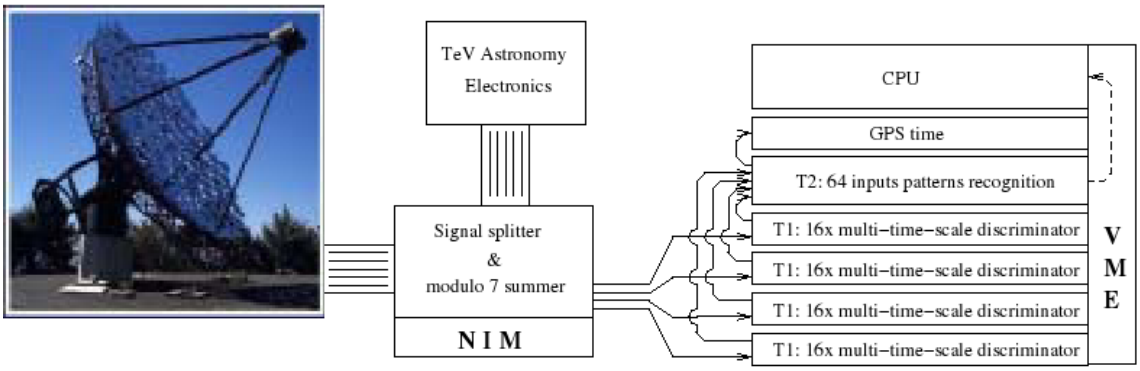

Figure 3.4 The schematic diagram of the different components of the SGARFACE electronics (figure taken from [35]).

In the splitter-summer circuit the analog signals from the 379 inner tubes are split by a passive signal splitter, which causes 11 % signal attenuation, but preserves the bandwidth for the standard Whipple TeV system. The analog signals of the neighboring Whipple PMTs forming a SGARFACE pixel are summed before being digitized. Information loss for short pulses during digitization of the signal in the typical range of 10 ns - 40 ns is avoided by shaping the signal to a width of more than 20 ns before it is digitized. The digitization is handled by 8-bit FADCs at 50 MHz (hence the sampling-time of 20 ns). Corresponding to the 55 SGARFACE channels, 55 splitter-adder boards are used and a voltage gain of 3 is applied to the signals going to the trigger modules.

These sub-systems and their and their respective functions are described in brief here. For a more detailed description see LeBohec et al. [32]. The next component, the MTS discriminator based on Xilinx Field Programmable Gate Arrays (FPGAs), integrates the digital signals, on different time-scales and then applies a threshold to each individual time-scale. Since the duration of burst due to PBHs is not known in advance, the multi time scale design makes the instrument sensitive to bursts of a wide range of durations, starting from around 60 ns to up to 35 μs. For a particular time-window the instrument

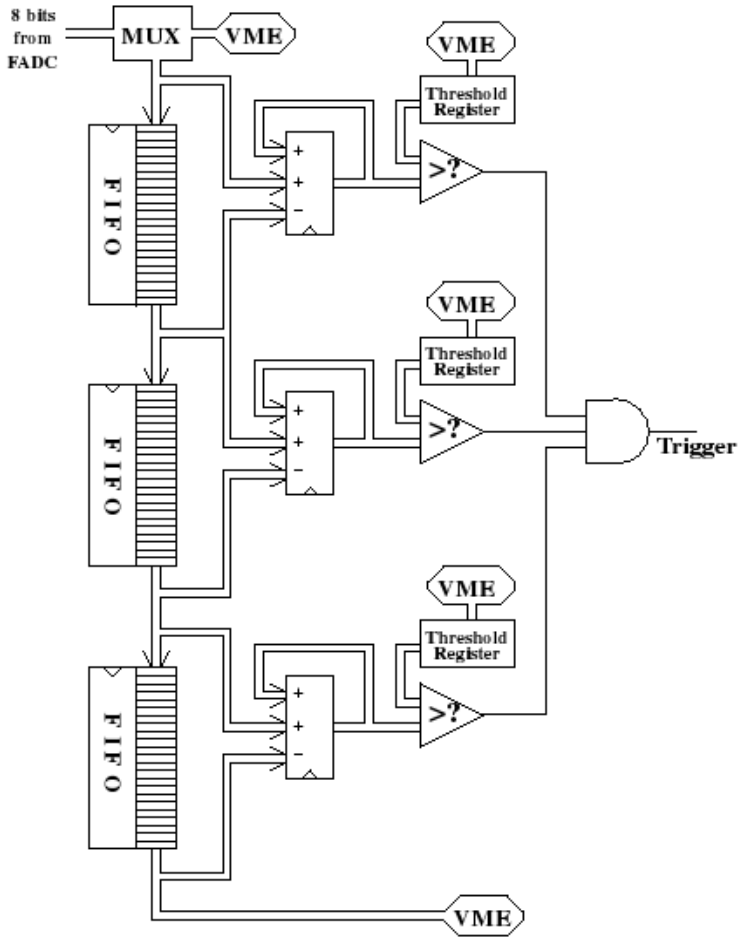

Figure 3.5 The schematic diagram of the MTS module, over three sectioned time windows in cascade (figure taken from [32]).

triggers if the sum of the signals in three consecutive time-slices exceeds a particular threshold. This summation is implemented in the FIFO (first in first out) register stacks by taking the difference between the input and the output of the stack. This logic is implemented in a cascade (see figure 3.5), by integrating three time-slices in each stage, forming time-windows of 60 ns, 180 ns, 540 ns, 1620 ns, 4860 ns, and finally 14580 ns. Thus the instrument is sensitive to bursts of at least 60 ns duration to more than 14.58 μs duration. This FIFO stack is implemented in $3^6 = 729$ registers, which gives 729×20 ns $= 15580$ ns of signal-data for each event. The maximum duration of signals that can be recorded is further increased by adding an extra stack of 1024 registers, which

give us an additional time of 20.48 μs, resulting in a maximum recording duration of $\approx$ 35 μs.

Level-2 trigger consists of a pattern sensitive coincidence (PSC) unit. It uses the fact that burst images are typically extended over 1° in diameter, as explained in the next section. It takes 64 asynchronous inputs, from 64 different overlapping subsets of the 55 SGARFACE channels. Each of these subsets groups a programmable number of neighboring pixels into a roughly circular unit. Thus the PSC unit fires, if a programmable number of pixels (typically 7 neighboring pixels is a good number) simultaneously give a level-1 trigger.

When a level-2 trigger occurs (this is a global trigger), the on-board computer is given a hard-ware interrupt; the CPU (Central Processing Unit) reads the data in the FIFO stacks and the extra 1024 memory registers in the MTS unit, the time-stamp from the VME based GPS (Global Positioning System) clock, and the trigger information from the PSC unit. The acquisition software, written in C, runs on the VME control, and communicates with the MTS and the PSC VME boards. Via a network connection it also gets the high-voltage values of the PMTs, the telescope tracking information, etc. of the standard Whipple 10 m TeV computer. All this information is written on the disk of the SGARFACE instrument, and a log-book is also updated. This now constitutes the SGARFACE event data, which is analyzed to search for burst like events. A skeleton of the SGARFACE analysis was developed in 2003 to check the integrity of the data. During this work a more extensive SGARFACE analysis software was developed by the author. This software-analysis is described in detail in the next chapter.

3.3 Imaging of bursts

Simulations show that (see Krennrich et al. [29]), the multi γ-ray initiated atmospheric cherenkov showers with individual energies above 200 MeV, incident on top of

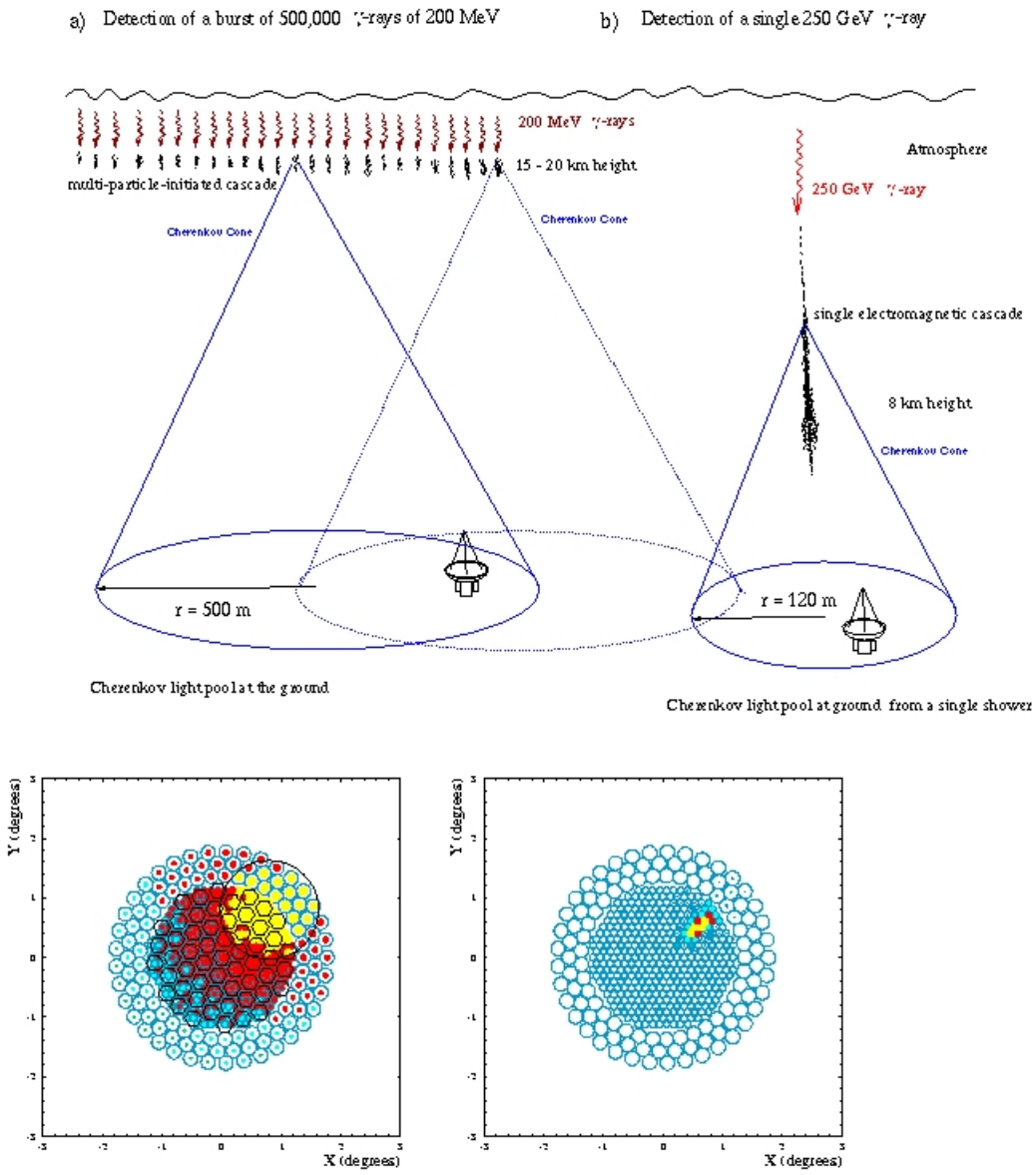

Figure 3.6 (a) The schematic representation of the formation and extent of multi-photon-initiated showers, bottom panel shows the image formed on the focal plane of the Whipple/SGARFACE camera. (b) The schematic representation of a single γ-ray shower and its image. Figure from Frank Krennrich (private communication).

the atmosphere within a short time window (around 0.1 μs to a few tens of μs), have very unique shower features and time structure. These spatial and temporal characteristics of multi-photon-initiated showers make these events ideally suited for detection using IACTs. Though best detected by an array of IACTs, the SGARFACE instrument on-board the Whipple 10 m, has been specifically designed to detect μs duration of γ-rays, and uniquely identify them as bursts. Using the trigger electronics described previously; and the off-line analysis of the SGARFACE events, described in the next chapter, a search for μs bursts can be carried out. The characteristics of multi-photon-initiated showers are described here.

From figure 2.3 it is clear that the lateral and the longitudinal distribution of the Cherenkov photons in a multi-photon-initiated is different from a single γ-ray initiated shower.

There are three noteworthy characteristics. Firstly, the large extent of the γ-ray wave-front means that the secondary particles (or electrons) and hence the Cherenkov photons are spread out over a large surface area of the earth. This makes it possible to simultaneously detect (neglecting the effect due to earth's curvature on the arrival time) the bursts with multiple telescopes which can be widely separated. If we assume that most of the primary γ-rays (have almost similar energies) are essentially incident parallel to each other; the showers formed by the individual primaries, will have a similar range of angular-size and orientation. Thus an array of IACTs would basically see identical shower images, almost simultaneous in time, but without any parallactic displacement. This property by itself would give short bursts a unique signature when detected by IACT arrays like VERITAS.

Secondly, the time profile of bursts like events will have an inherent width typically longer than the duration of Cherenkov flashes from cosmic-ray showers, or single γ-ray initiated showers, see figure 3.7. This width of the γ-ray front, as well as the difference in

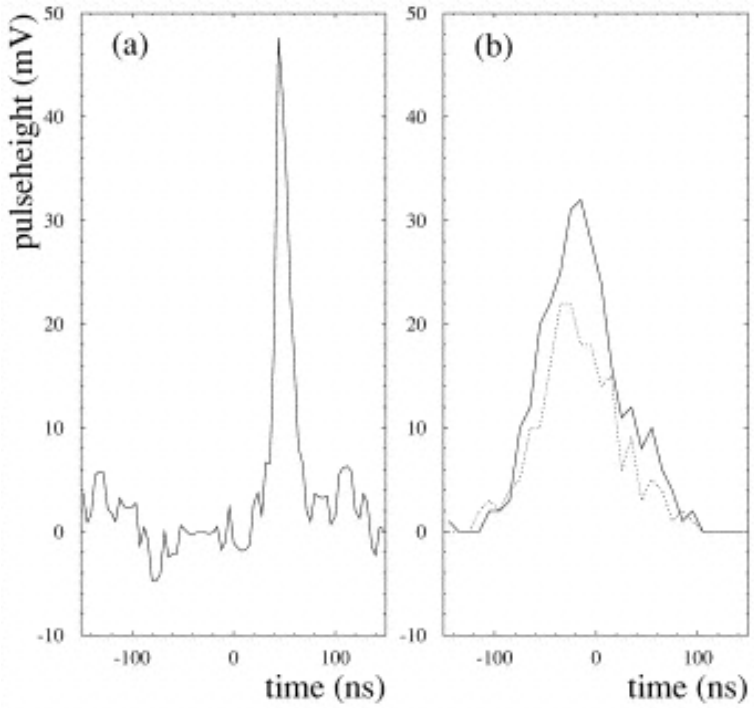

Figure 3.7 Figure and caption from [29]. "(a) Pulse shape for a cosmic-ray event recorded with the Whipple 10 m telescope is shown. The noise is the result of fluctuations from the night-sky background light. (b) The pulse profile of a simulated multi-photon-initiated cascade for two photomultipliers, one in the center of the image (solid line) and one by 1° off-center (dotted line), are show. The burst timescale is 100 ns. Here the night-sky background noise is not included ..."

the time-of-flight of Cherenkov photons coming from right above the telescope and the photons incident from the outermost limit of the FOV of the telescope, gives such events a longer time profile than single particle initiated showers.

Lastly, the image formed on the focal-plane-instrument will be roughly circular in shape, with a bright central region surrounded by a smooth diminishing halo. From simulations Krennrich et al. [29], it is shown that ultra-short-burst images have eccentricity of ≈ 0.1 to 0.4, and a radius of $\approx 1°$, see figure 3.8. This slight eccentricity is due to the effect of earth's magnetic field, and varies with the orientation of the shower axis with respect to the magnetic field, see LeBohec et al. [32].

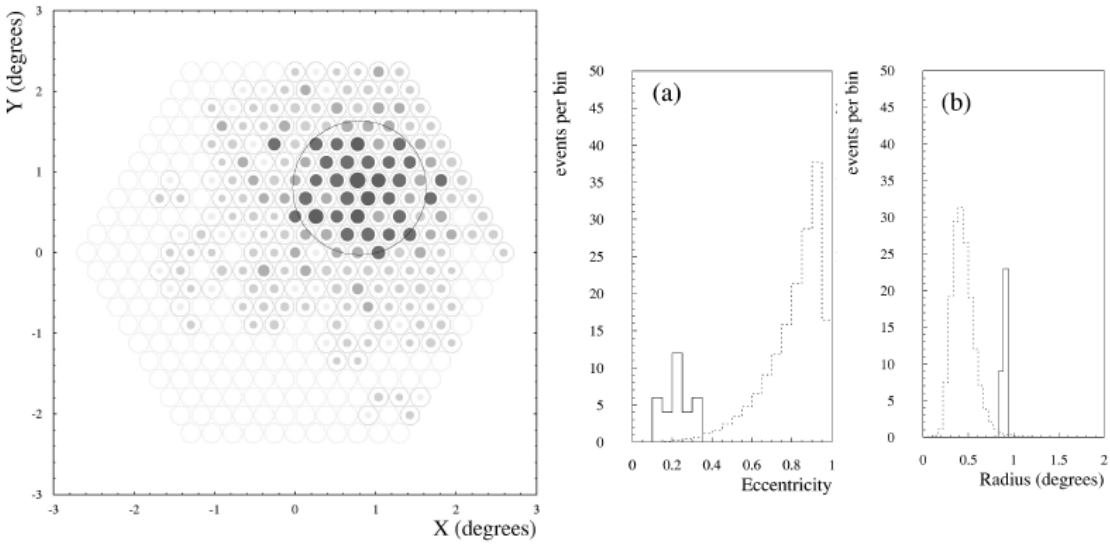

Figure 3.8 Figure from [29]. Extreme Left: "Simulated image of a burst of 300 MeV gamma rays lasting for 100 ns with a photon density of fluence $4.8 \times 10^8 ergs/cm^2$..."; Middle: "Eccentricity $[(1-[Width^2/Length^2)^{1/2}]$ of images from wave front events are shown. The distribution for wave front events peaks at 0.2, as expected for almost circular images. The dotted curve represents cosmic-ray showers recorded with the Whipple Observatory 10 m telescope..."; Right "The estimated Radius of simulated wave front events (solid line) is compared with the radius of detected cosmic-ray background events (dashed line). Only cosmic-ray events with the same or larger light content (size) in the image as for the simulated wave front events are accepted. The average Radius of the images from 500 MeV bursts is approximately 0.8°, which corresponds to the half-width in the radial profile.".

All these unique features of burst-like images are exploited in the analysis-software, which is described in the following chapter.

CHAPTER 4. SGARFACE ANALYSIS

This chapter describes the steps in the analysis of SGARFACE data. The SGARFACE data for an observing run consist of the following. A log file of all events recorded during the run, and event files containing signal data from all pixels for each recorded event. In the analysis of a SGARFACE event, the first step is to properly scale the data/signal from each individual pixel, and the calculate noise distribution. A cleaning cut, representative of the noise in the channel is then applied to the data. Then the pulse in the signal data due to the Cherenkov flash is identified and the charge under the pulse calculated. At this point another cleaning cut on is applied based on the charge in the pixel. The various image parameters, viz. the length, width, image center, image orientation, and total charge is found (see Appendix B). The event parameters and charges are written out to a file for further analysis, and an image display is created. Note that, SGARFACE is designed for detection of long duration and weak intensity bursts from PBHs and other bursts of γ-rays. However in this work cosmic ray events are analyzed to cross-calibrate Whipple and SGARFACE.

Here a brief description of the operation and data acquisition of the SGARFACE system is given, followed by a detailed description of the processes involved in the analysis of SGARFACE events.

It can also be stopped at any time and the programmable IC chips[1] in the trigger electronics reconfigured, if needed. During a run, for each event that triggers the instrument, an entry is made into a log book file and the signal data of all the 55 channels are

[1]Xilinx FPGAs (Field Programmable Gate Arrays)

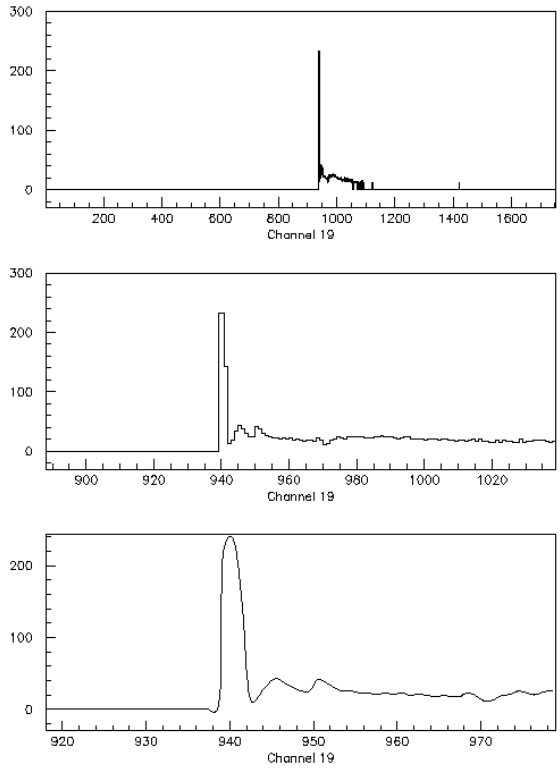

Figure 4.1 The signal profile in a particular channel for a SGARFACE event is shown here. Top panel is the entire data length $1753 samples \times 20 ns \approx 35 \mu$s, the middle and bottom panels zoom in on the pulse in the data. Note the apparent increase in the pedestal level after the pulse, also referred to as the signal tail, in the text. Y-axis is in d.c. (digital counts), X-axis gives time samples.

written into a separate event file. The log book file contains information about events, such as the GPS clock time stamp, the event file name, the telescope pointing information, pixel settings (pixel x and y coordinates in the camera, diameter in degrees), and trigger settings (threshold for different time scales of the MTS, and threshold information for the PSC unit). A SGARFACE event file has the GPS clock time stamp up to microsecond precision, and the signal stream for each channel. The data (signal stream) in each channel consist of 1753, 8-bit (corresponding to a dynamic range of 0 d.c. to 255 d.c.) numbers in units of d.c., with a gap of 20 ns between each sample.

This data is used for the analysis of the SGARFACE events. Figure 4.1 shows the actual signal data of a particular channel.

The software analysis proceeds in the following steps. The major functions and the sequence of operations involved in the software analysis is shown in figure 4.2.

4.1 Pedestal and noise calculation

The noise in the events consists of fluctuations from the average night sky background, as well as the electronic noise. The signal carrying circuit between the PMT and the FADC is ac coupled at the Splitter-Summer module to remove the d.c. component due to the night sky background (and the small dark current in the PMT). A small biasing current is artificially injected into the ADCs in order to allow negative fluctuations from the average night sky background to be recorded. This biasing current is referred to as the "pedestal". In order to calculate the actual amount of light detected by the PMTs this pedestal has to be subtracted from the signal, thus correctly scaling the signal. After pedestal subtraction the charge under the pulse in the signal, gives the amount of light detected. The variation about the mean of the pedestal gives a measure of the noise in the data.

When a trigger occurs in the electronics an additional 800 clock ticks (a look forward of 800 data samples) are recorded to ensure that enough data is taken for the processing of long duration bursts. The processing of the level-2 PSC trigger (see section 3.2) takes another $\approx$ 15 (300 ns)CPU clock ticks. Thus in the SGARFACE channels the signal data has the pulse at around 800 time samples from the end of the signal data. We can see from figure 4.1 that the pulse due to the Cherenkov photons detected by the PMT occurs at around $1753 - 815 = 938^{th}$ time sample. The signal data recorded before the pulse (i.e. before the trigger occurred) allows us to estimate the pedestal and the noise.

The pedestal for a channel is calculated in two iterations. In the first iteration the

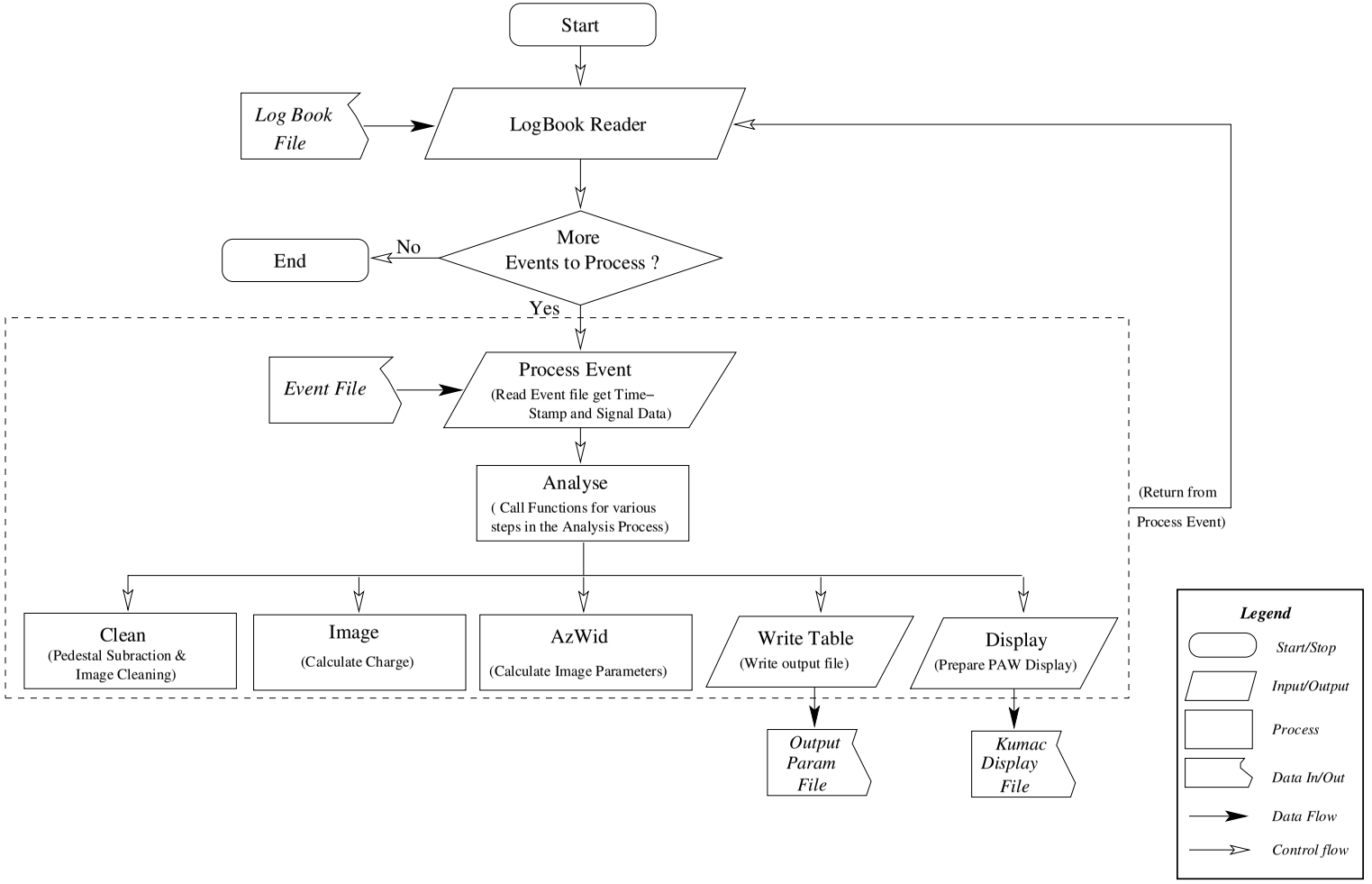

Figure 4.2 The major steps in the analysis of SGARFACE events. See section 4.1 for details.

mean and standard deviation of the first 700 samples of data is calculated. In the second iteration, only those samples in the first 700 data points that lie within 4 times the standard deviation (calculated in the first iteration) are taken to calculate the mean and the standard deviation. The mean is the pedestal, ped_i in the particular channel (i^{th}) and the standard deviation, σ_i is the measure of noise. Doing this in two iterations was designed to eliminate any incidental extremely noisy samples and give us a sharp distribution for the pedestal and thus a more accurate estimation of the noise. In practice, however (see figure A.1 to A.5) most of the cosmic ray events recorded had a well defined pedestal distribution. Thus we have for n samples in the second iteration:

$$ped_i \equiv \langle signal \rangle_i = \frac{\sum_{j=1}^{n} signal_{ij}}{n} \quad ; \quad \begin{array}{l} where\ signal_{ij}\ is\ the\ j^{th}\ data\ sample\ in\ the \\ i^{th}\ channel,\ and\ n\ is\ number\ of\ samples \end{array}$$

$$\sigma_i \equiv \sqrt{(\langle signal^2 \rangle_i - \langle signal \rangle_i^2)} \quad ; \ where\ \langle signal^2 \rangle_i = \frac{\sum_{j=1}^{n} signal_{ij}^2}{n}$$

Another way to calculate the pedestal would be to plot the histogram of the signal in a channel and fit a curve (e.g. a Gaussian) to this histogram. The x-axis would be the signal values in d.c., and the y-axis would be the number of data points. Thus for a Gaussian that fits the histogram, the x-position of the peak of the curve would give the ped_i, and 1/2 times the full-width-at-half-maximum (FWHM) would give the $sigma_i$. To check that both methods gave consistent results, the pedestal calculated by both methods was compared, see Appendix A. The typical value of pedestal ranges between roughly 9 d.c. to 30 d.c., and the σ_i ranges between 0.5 d.c. to 3.5 d.c.. The noise which we define as $4 \times \sigma_i$ for the cleaning procedure is therefore between 2.0 d.c. to 14 d.c.

In the analysis of Whipple events a process called flat fielding is carried out, in which a nitrogen flasher is used to illuminate the entire focal plane evenly, and the relative gains in the PMTs are normalized. The nitrogen flasher is relatively bright and since we are summing 7 Whipple pixels into 1 SGARFACE pixel, the SGARFACE electronics is saturated by the nitrogen flasher. Thus a direct relative gain calculation for SGARFACE pixels is not possible with nitrogen flasher events. However, the cosmic

ray cross calibration (see Chapter 5) allows to link the SGARFACE gains to the gains from Whipple.

4.2 Charge calculation

The pedestal in a channel is subtracted from each data point. Also at this point a cleaning cut of $4\sigma_i$ can be applied to each sample, setting the signal to zero where the d.c. value falls below $4\sigma_i$. The resulting signal is then used for charge calculation. The charge is given by the area under the pulse in the signal. Thus we need to define the pulse properly. A set of criteria is needed to identify the pulse by defining the beginning and end of the pulse. The trigger for a cosmic ray event, occurs at around the 938^{th} data sample and the signal usually peaks either at the 938^{th} or the 939^{th} sample. The pulse in the signal corresponding to the Cherenkov flash detected, is around this point. The beginning of the pulse is defined where the signal exceeds $4\sigma_i$, to the left of the peak in the pulse. Establishing the end of the pulse is slightly more difficult, since the falling part of the pulse is contaminated by noise from the electronics.

In LeBohec et al. [32], section 4.1 it is explained that for all time scales except the 14.58 μs time scale there is a tail after the small pulses, which is due to a reflection from the Whipple 10 m TeV electronics as a result of a capacitive feed back in the splitter module. In practice this is visible even in pulses that are near the saturation level (maximum dynamic range of 255 d.c. of the FADC). This might be confused as an apparent shift in the pedestal level. Therefore we calculated the pedestal from only the first 700 samples in the signal which comes well before the trigger. This makes it necessary to define the end of the pulse by carefully excluding this tail. Cutting off the pulse when it falls below $4\sigma_i$, to the right of the pulse peak, and/or decreases by less than 15 d.c. between two consecutive samples, proves to be reasonable criteria for defining the end of the pulse. These criteria work well as will be evident later on, by comparing

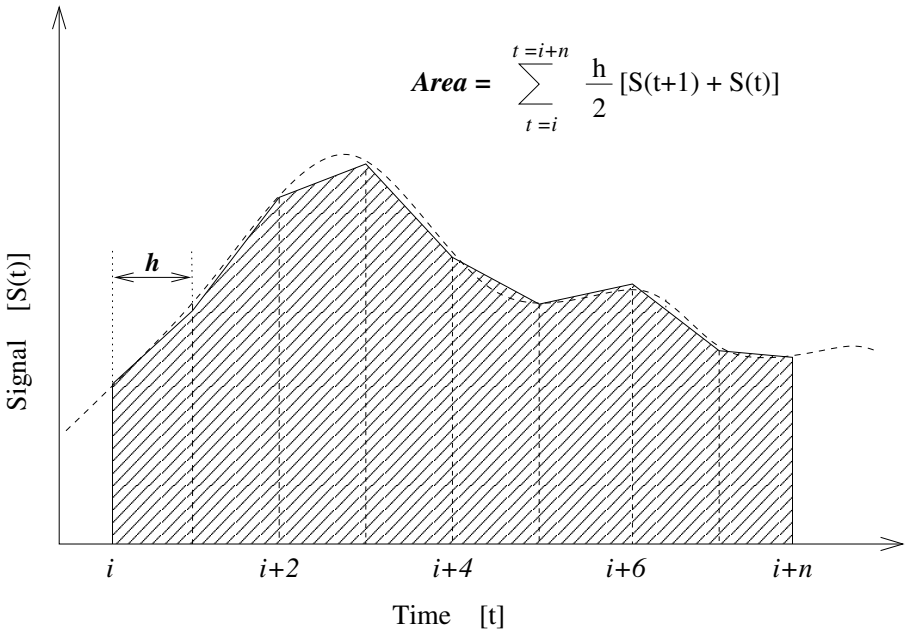

Figure 4.3 The *Trapezoidal rule*, a well known numerical technique for evaluating area under a curve. Here area is evaluated for n data points from sample t to $t+n$, and h is 20 ns, but for evaluating the charge we take it as 1 time sample in our case. The unit of *S(t)* and the *Area* is d.c.

images of coincident events between the Whipple 10 m and the SGARFACE instrument, (see figure 5.3).

Once the pulse is clearly identified using the above mentioned criteria, the charge is found by calculating the area under the pulse by using the "Trapezoidal rule" (see figure 4.3). The unit of charge is also d.c., since it is nothing but the sum of d.c. values under the pulse. Thus we have:

$$charge_i \;=\; Area \;\equiv\; \sum_{t\,=\,i}^{t\,=\,i+n} \frac{h}{2}\,[S(t+1)+S(t)]$$

4.3 Saturated channels

The procedure described above works well for signals that do not exceed the digitizer range of 255 d.c., the saturation limit. In practice it is seen that for bright cosmic-

ray events the signals in many channels are saturated. Various methods were tried out to calculate the charge for saturated pulses. The methods involve trying to estimate the pulse shape above the saturation level, which would enable us to get calculate the additional charge in the saturated part of the signal. This would give us better values for the net charge under the pulse.

For example, we can make reasonable assumptions about the pulse and find out certain characteristics of the pulse shape that scale with pulse height. The rising slope, the falling slope (slopes before and after the pulse peak respectively), and the charge over an artificial threshold are characteristics that were investigated.

The first method assumes that the pulse shape, and hence the rising and falling slopes scale with pulse amplitude. Once this average or limiting value of the slope is obtained from unsaturated signals, the shape of the saturated pulse can be extrapolated using these slopes. First the slope between the left most saturated data sample, and the data sample to its left was found, we call this 'first slope before peak' ($s1$). The slope between the next two data samples was called the 'second slope before peak' ($s2$). Then the average of these two values gives us the 'average rising slope'. Similarly for the falling part of the pulse we get the 'first slope after peak' ($s3$), 'the 'second slope after peak' ($s4$), and the 'average falling slope', see figure 4.4, top panel. These values for all channels in around 200 events is shown in figure 4.4, bottom panel. We could now in principle use either the average rising/falling slopes or the limiting values as defined by the maximum and minimum of the 'first slope' and 'second slope' to extrapolate the pulse shape in the saturated region. However in practice it is seen that the corresponding values of first slope before peak and first slope after peak for a saturated channel are well beyond these values for the unsaturated channels. Hence the assumption that the rising/falling slopes remain constant with signal amplitude does not seem to hold good, and we cannot use this method.

The second method tried out, was to estimate the charge-over-threshold for unsatu-

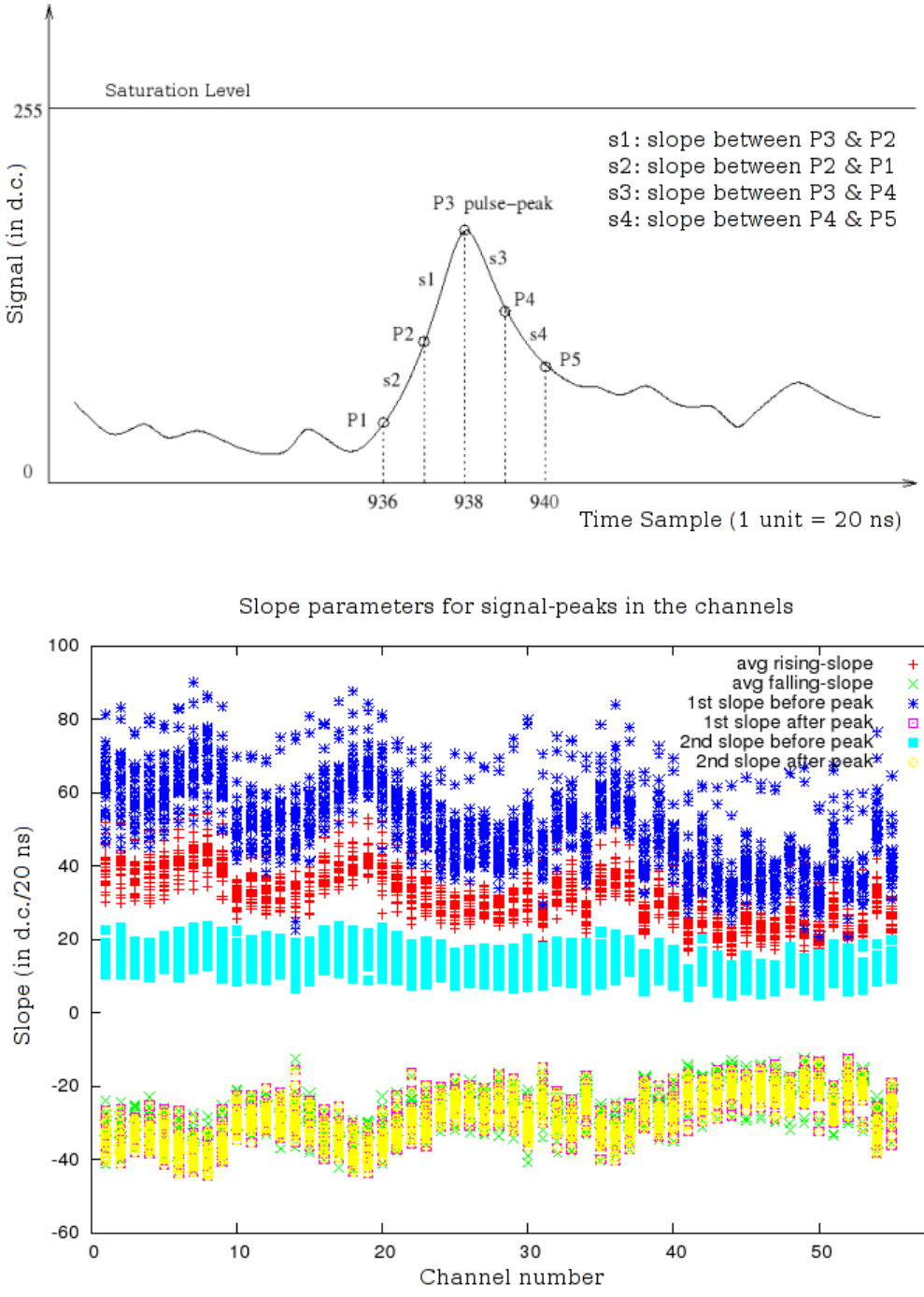

Figure 4.4 (Top) A schematic representation of a Pulse in an unsaturated channel, with various slopes defined. s1 is the 'first slope before peak', s2 is the 'second slope before peak', s3 is the 'first slope after peak', and s4 is the 'second slope after peak'.(Bottom) Slope parameters for pulse shape.

rated channels, by setting and artificial saturation level, well below 255, as a function of the 'threshold-intercept' (see figure 4.5, top panel).

Using two different values for artificial threshold and plotting the charge-over-threshold, we get figure 4.5, bottom panel. There are two features to note in this plot. Firstly the charge-over-threshold rises with an approximately linear slope and peaks at some value that is inversely proportional to the saturation level. This can be explained by the fact that we are taking pulses that have a maximum height of 255 d.c., thus the charge-over-threshold will peak at some value depending on the artificial threshold level chosen. Secondly the distribution has two components almost parallel to each other one starting near the threshold-intercept of 0 ns and the second one starting at threshold-intercept of 20 ns. This is clearly a digitization effect. Since the FADC digitizes the signals at 20 ns intervals, the threshold-intercept also reflects this, and so does the calculated value for the charge-above-threshold.

This means that the digitization rate is too low for signals from cosmic-ray events. Thus the threshold intercept cannot be calculated accurately. Using the correlation in the plot, figure 4.5 (lower panel) to extrapolate over saturated pulses, it was found that the limitations due to low digitization rate make this method inefficient. Therefore this method was not implemented in the code.

Another simple method to extrapolate the pulse shape in the saturated part, was to draw straight lines along the rising part and falling part of the saturated channel, get their intercept, and treat it as the approximate pulse shape above the saturation limit. To estimate the charge of the saturated part we can calculate the area of the triangle formed by the first saturated point, the last saturated point and the intercept of the straight lines from these (the extrapolated pulse peak), see figure 4.6. The total charge is the sum of the estimated charge above the saturation and the charge below saturation. This method can be used to get a first approximation for calculating charges for saturated signals and is implemented as an optional part in the analysis code.

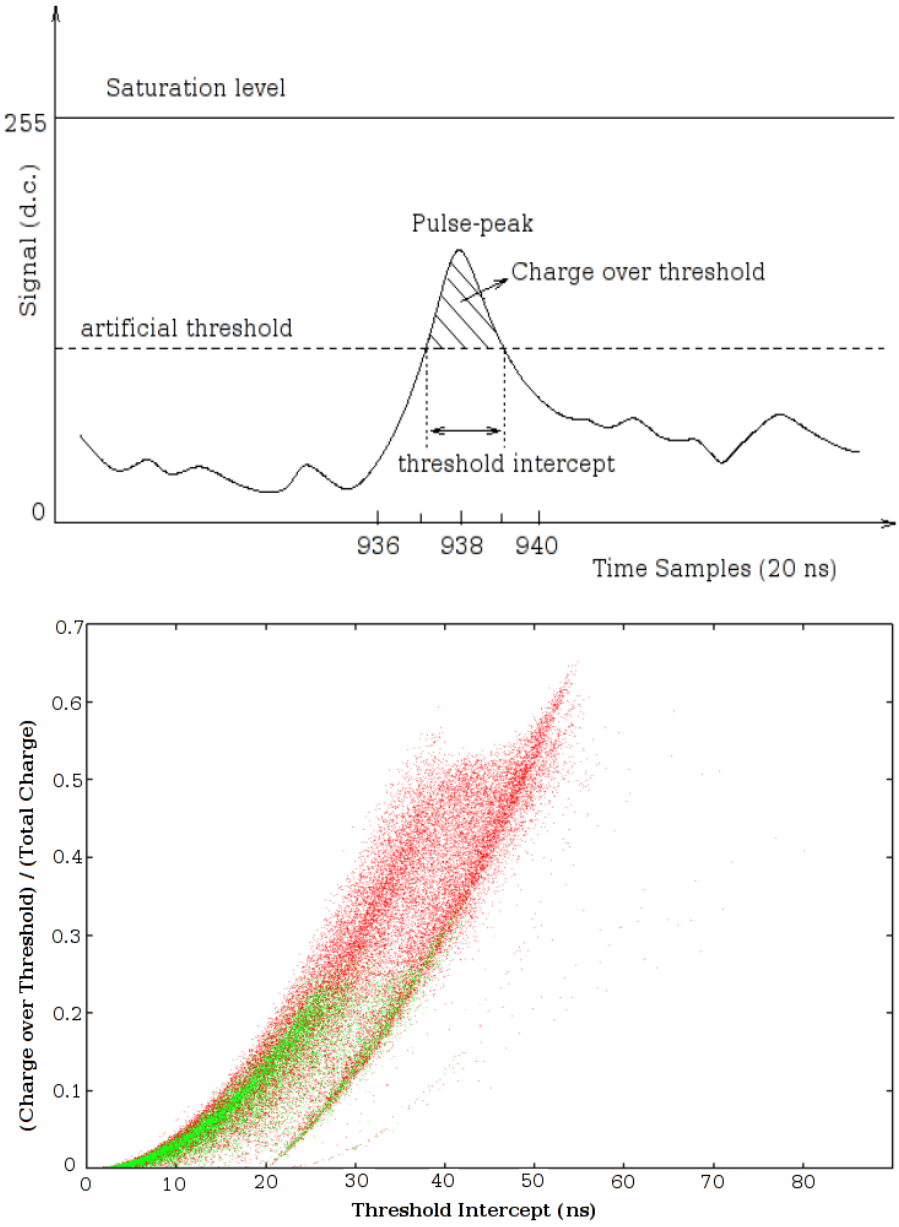

Figure 4.5 (Top)A schematic representation of a Pulse in an unsaturated channel, showing the artificial threshold level, the charge-over-threshold, and the threshold-intercept. (Bottom) The plot of the ratio of the charge-over-threshold to the total charge. The red points are for saturation level set at 60 d.c., and the green ones for 120 d.c.

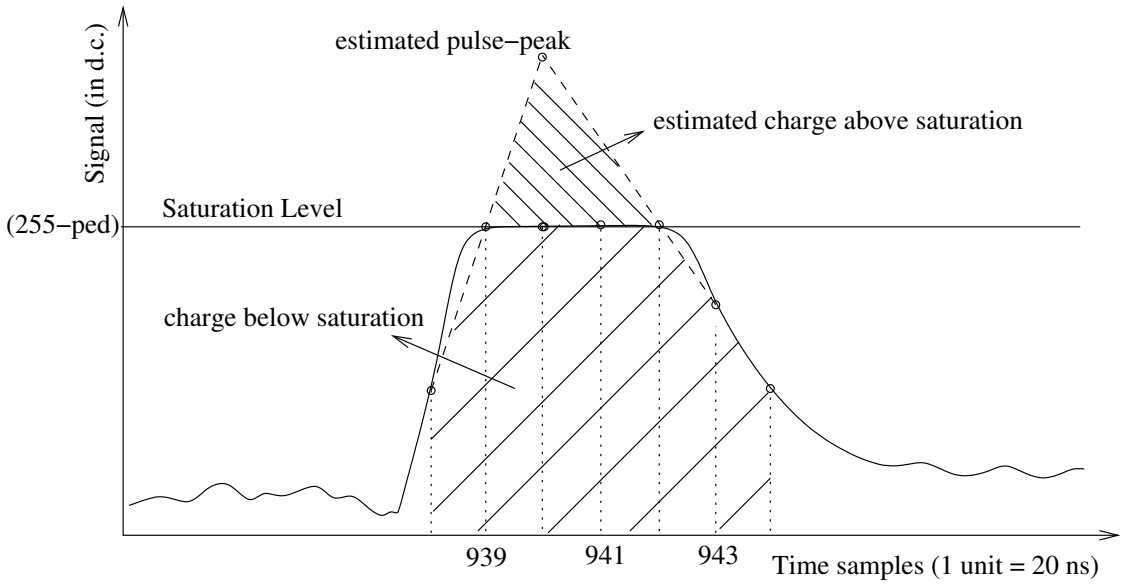

Figure 4.6 The extrapolation of points to find the pulse peak, and calculate the charge above saturation level.

The other method tried out for estimating the charge above the saturation level involved estimation of the actual pulse peak and shape from the reflection in the signal. In an electronic circuit if the different components in a circuit are not properly terminated (impedance mismatch), then the signal is reflected back and forth within the circuit. If the impedance of the different components are accurately calculated, the reflection coefficient (ratio of the reflected signal to the input signal) can be estimated, as well as the time delay between the signal and its reflection. Using this coefficient, the reflected signal (which has smaller amplitude and hence not saturated) can be re-scaled and compared with the unsaturated section of the actual signal to estimate the shape and amplitude of part of the signal that was lost, see figure 4.7. In practice calculating the impedance of the electronic components, and the cable is not trivial. The theoretical impedance calculated from the electronic schematics involves a number of approximation for the response of operational amplifiers in the circuit, cable impedance and time profiles in the capacitive couplings. In actual practice most of these parameters also have a temperature dependence. Thus

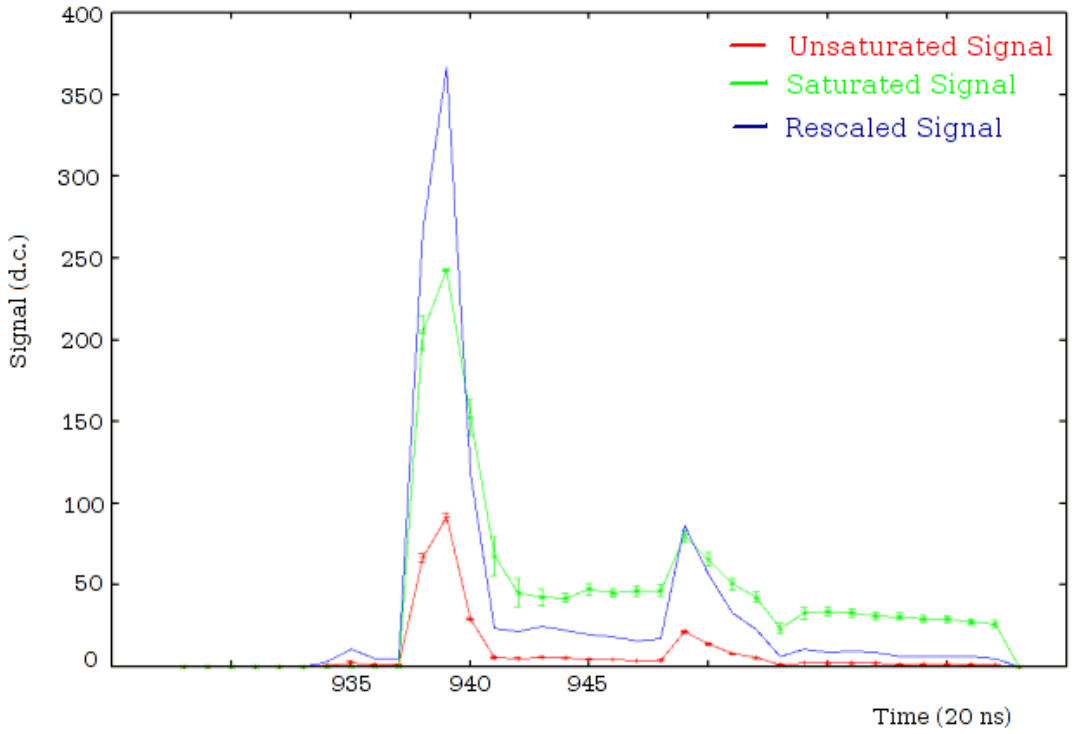

Figure 4.7 Reflection of the signal used to re-scale the saturated signal. The reflection coefficient was obtained from averaged profile of unsaturated signals(red). This was used to re-scale saturated signals (in green). The re-scaled signal (blue), is clearly inconsistent with the tail of the saturated signal. Also, note that the reflection pulse is after $\approx$ 200 ns of the signal pulse, where as the theoretically calculated value for the time gap was $\approx$ 67 ns

these parameters have to be measured by experimental means by measuring the current and voltages across various components. Such measurements were not available and the theoretically calculated parameters were inconsistent with the data. Thus this method cannot be applied until accurate measurements of the circuit parameters are made.

4.4 Image parameters

Once the charge for all the channels in an event is calculated, the image formed on the focal plane can be reconstructed. An image cleaning procedure can also be implemented

at this stage. Traditionally, image analysis for Whipple events (see Mohanty [37]) use a 'picture threshold' and a 'boundary threshold' to select pixels that are to be excluded in forming the image. Pixels that have charge/pulse-height greater than a certain threshold, called the picture threshold are included in the image analysis. We can call these picture pixels. Also pixels adjacent to a picture pixel, but with charge/pulse height lower than the picture threshold are included in the image analysis, provided their charge is higher than another threshold value, called the boundary threshold. We can call these boundary pixels. However, in the SGARFACE analysis only a picture threshold is sufficient to extract the relevant image information. The nature of the bursts of γ-rays is such that we expect most of the light to be concentrated within an angular size of $\approx\ 1^{\circ}$, in the sky. Beyond this there will be a halo, with a smoothly decreasing intensity. Most of the information about the burst, such as the arrival direction, average energy of γ-rays can be effectively derived from the bright central region. Also the timing characteristics of the bright central region would give the relevant information about the duration of the burst. Thus having a boundary threshold does not add any useful information for the image analysis, and can be ignored.

The image constructed after a picture threshold of 4σ (4 times the standard deviation of the pedestal, see section 4.1) is applied to the charges in the channels, can be displayed using PAW. The various image parameters are also calculated and displayed along with the color coded charge in the various channels, see figure 4.8. The explanation of different image parameters is given in Appendix B. The ISU analysis software for the Whipple 10 m TeV system also calculates most of these values for events detected by that system. Thus we have a well defined set of parameters to compare events that are simultaneously detected by both the SGARFACE and Whipple 10 m instruments. After the parameters are calculated an output file is updated with the information such as charges in all the 55 channels, the MJD (modified Julian date) of the event, and the image parameters.

4.5 SGARFACE event display

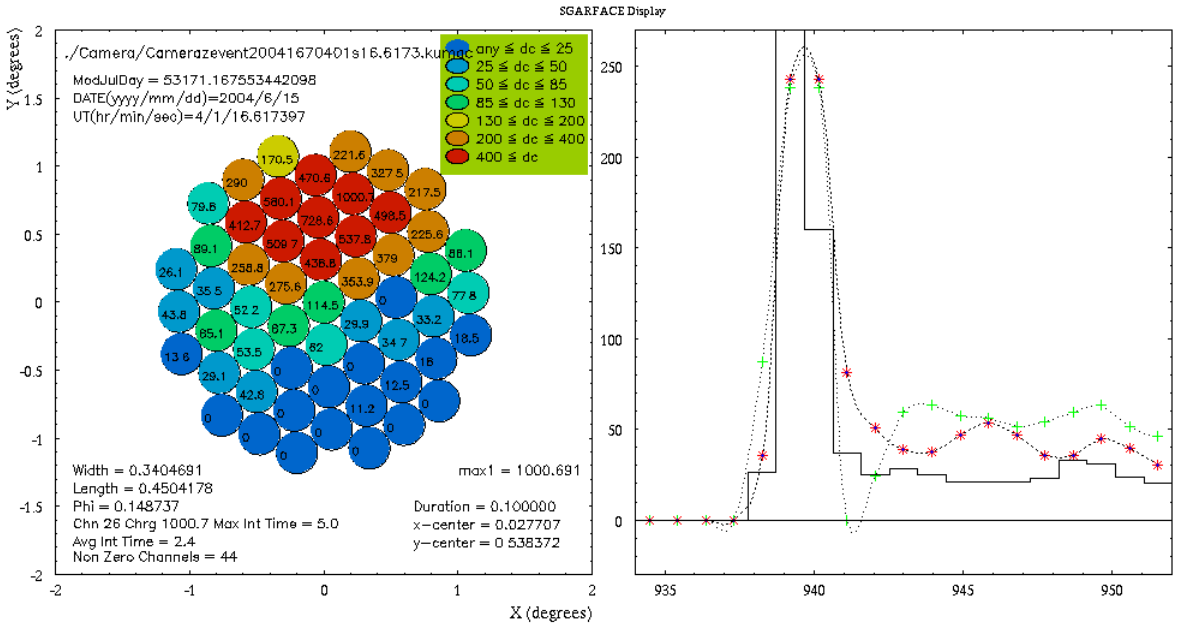

Figure 4.8 Shown here (left) is the SGARFACE event display, with the different image parameters, and (right) the pulse profile of the 3 hottest (greatest charge) channels in this event.

The objective of the imaging technique is to reconstruct the shower from the image parameters obtained from the software analysis of the events detected by the instrument. The technique extracts useful information such as the energy of the primary γ-ray (or cosmic-ray), the direction it was incident from, and the flux at different energies and directions. The event display of the images formed at the focal plane gives us a feel of these aspects. The event display also gives a visual confirmation that the different steps in the image analysis, and the calculated image parameters are consistent with the charges detected in the pixels.

For example, the left panel of the display shown in figure 4.8, represents the camera in the correct scale in units of degrees in the sky. It shows the charge in each pixel by their value in d.c. as well as a color coded scheme. Also the MJD of the event, and the image parameters are given here. The right panel shows the pulse profile of the three

hottest (largest charges) pixels. Some other displays were developed during the course of this work, each was designed to check a different aspect of analysis and cross calibration.

In Appendix D a number of examples of the different SGARFACE event displays are shown. For example in figure D.3 stages in the SGARFACE analysis are shown. This display is ideal for a quick look at the effect of different analysis steps such as pedestal subtraction and signal cleaning.

Calculation of image parameters and construction of the event display completes the SGARFACE analysis stage. The second stage of this work to analyze coincident events and cross-calibrate SGARFACE against the Whipple TeV instrument is discussed in Chapter 5.

CHAPTER 5. CROSS CALIBRATION

To cross-calibrate the SGARFACE instrument with the Whipple TeV system, events simultaneously triggering both instruments are analyzed. Then the charges in each SGARFACE pixel is compared to the sum of charges in the corresponding constituent Whipple pixels. The Whipple 10 m telescope has been carefully calibrated before, and the gain in terms of d.c. (digital counts) to p.e. (photo-electron) ratio was $\sim 3.3\ \frac{d.c.}{p.e}$, measured in 2001. The gain of the Whipple 10 m has been monitored for subsequent seasons (see Daniel et al. [10]). The ratio of charges and the known conversion factor between d.c. and p.e. for Whipple is then used to derive the d.c./p.e. value for SGARFACE.

To look for long-duration events in the SGARFACE data, the aggregate signal profile for the event is found by adding up the signals in all the SGARFACE pixels at each data-point. The width of the signal-pulse due to the Cherenkov flash in the aggregate profile is calculated. A set of criteria based on this pulse-width, and the image-parameter is then used to select possible events that might be due to bursts of γ-rays.

In this chapter the procedure for finding and analyzing coincident events for cross calibration is explained, followed by the preliminary attempt to search for long duration bursts of γ rays. It should be pointed out that the objective of this work is accomplished with the cross-calibration of the instruments. The preliminary search for burst-like events and the analysis of such events is beyond the scope of this work. The intention here was to prepare the skeleton of the software tools that might be used in the near future to search the SGARFACE data for burst-like events.

5.1 Coincident events between SGARFACE and Whipple

To find events coincident in time in both SGARFACE and Whipple TeV instruments, the SGARFACE event analysis output file and a similar output file for Whipple events are used. If the event-time, expressed in Modified Julian Date(MJD)[1], of a SGARFACE event matches (within a specific time-window), with that of the Whipple event, we call this pair of events a coincident event. Since the SGARFACE events time stamp is has only μs level precision, the minimum time window is 1.0 μs. The program that searches for coincident events then writes down the relevant event information such as the MJD, charges in channels, image-parameters for the coincident pair to another output file, which can later be used to analyze and display these events.

5.1.1 Coincident event analysis

Coincident events are analyzed to see the time-overlap for events that trigger both the instrument, as well as how well the image parameters match.

First of all we need to check if we are looking at actual coincident events, and not chance-coincidences[2].

This can be done in two ways. One would be to calculate the expected chance-coincidence rate and then compare it to the measured coincidence rate. Note that, the Whipple event rate is $\sim 20\ Hz$, or in other words Whipple events occur after every 50 ms (assuming Whipple produces events at constant-rate) with a typical event duration of 20 ns; and SGARFACE event rate is $\sim 0.5\ Hz$, i.e. one SGARFACE event every 2 s with

[1]Modified Julian Date, $MJD = JD - 2400000.5$; where JD is the Julian Date, which is an integer counter of the days beginning at noon $January\ 1^{st}$ 4713 $B.C.$, which is defined as Julian Day Number 0. The 0.5 part in the conversion to MJD implies that it starts from Mid-night Universal Time (UT). The fractional part of the MJD is the fraction of the day passed since last mid-night UT.

[2]Here by 'actual-coincident event', it is meant that the same cosmic-ray initiated air shower triggered both instruments, hence its an 'actual' or a real coincidence. Whereas, it might so happen that the time-window (which is kept constant for a run), that is chosen to capture coincidences could capture a random set of events that are not triggered by the same air-shower, and hence the term 'chance-coincidence' or a random coincidence.

a duration of $\sim$ 60 ns. Thus, the chance of catching a random Whipple event within a SGARFACE event seems slim, since the SGARFACE duration of 60 ns, is around 6 orders of magnitude smaller than the approximate gap of 50 ms between Whipple events. If the time-window for coincidences in the program is chosen judiciously, the actual coincidence rate should be much greater than the chance coincidence rate.

A second way of testing whether a coincident event is due to two different origins (e.g. two different air-showers offset by several 100 ns), is to compare the images in Whipple and SGARFACE (see figure 5.3).

Assuming that both Whipple and SGARFACE instruments produce constant-rate events (i.e. assume, events repeat after constant time gaps) is not absolutely true, since cosmic-ray-events happen randomly. However, we can go ahead with this assumption and get a first estimate for the coincident event rate. The chance coincident rate is calculated as follows. We have

$$\begin{aligned} &\textit{the SGARFACE event rate} && : R_S \sim 0.5\ Hz, \\ &\textit{the SGARFACE event duration} && : \Delta_S \approx 60\ ns, \\ &\textit{the Whipple event duration} && : \Delta_W \approx 20\ ns,\ \textit{and} \\ &\textit{the Whipple event rate} && : R_W \sim 20\ Hz. \end{aligned}$$

$$\textit{Thus, probability of no whipple events within a SGARFACE event} = e^{-R_W \Delta_S}$$

$$\textit{probability of at least one whipple event within a SGARFACE event} = (1 - e^{-R_W \Delta_S})$$

$$\textit{Now, } (1 - e^{-R_W \Delta_S}) \approx R_W \Delta_S \ (\textit{upto } 1^{st} \textit{ order}) = 1.2 \times 10^{-6}$$

$$\Rightarrow \textit{ chance coincidence rate } = R_S(1 - e^{-R_W \Delta_S}) \sim 6 \times 10^{-7}\ Hz$$

This is the approximate lower limit for chance coincidences. It is therefore apparent, that the rate from random coincidences is very low (1 in 200,000 s, which means 1 in 70 hours). Now, instead of Δ_S, if we use the width of the time-window (Δ_t) used to capture coincident events in the data, we can have an estimate for what values we should

be getting for chance coincidences for a given time window. Then we can compare this to the results we get from the code to get coincidences form SGARFACE and Whipple event data. As the time-window is made larger it becomes more likely to catch random coincidences. This is in fact what we get in practice, see Table 5.1. From the table it can be seen that the chance-coincidences start to dominate when the time-window is a few $\sim 10^3 \mu s$ wide.

As a practical matter, it should be noted that the precision of the GPS clock to record the time at which an event occurs, is 1 μs. Thus, in the code we cannot have a time-window less than a μs.

Table 5.1 Calculated chance-coincidence rate, and coincidence rates obtained from the data for various width of the time-window.

Time-window (μs)	Calculated chance coincidence, R_{cal} (Hz)	Coincidence from Code, R_{cod} (Hz)	R_{cod}/R_{cal}
1.0	10^{-5}	0.049 ± 0.003	4.9×10^3
2.0	2.0×10^{-5}	0.119 ± 0.007	5.95×10^3
4.0	4.0×10^{-5}	0.171 ± 0.009	4.27×10^3
10.0	10^{-4}	0.174 ± 0.010	1.74×10^3
25.0	2.5×10^{-4}	0.174 ± 0.010	6.96×10^2
100.0	0.001	0.175 ± 0.010	1.75×10^2
10^3	0.010	0.181 ± 0.010	1.81×10^1
10^4	0.100	0.228 ± 0.012	2.28

The coincident event analysis code gives a coincidence rate of $\sim$ 0.05 Hz for the smallest time-window. This lower limit for the coincidence rate from the analysis is $\sim 5.0 \times 10^4$ times greater than the estimated chance coincidence rate. This by itself confirms that we actually have true coincidence events, which can be used for cross calibration.

Figure 5.1 shows how the coincident rate varies with the width of the time window. We can see the coincident rate rising till about the width is $4.0 \mu s$, and then it

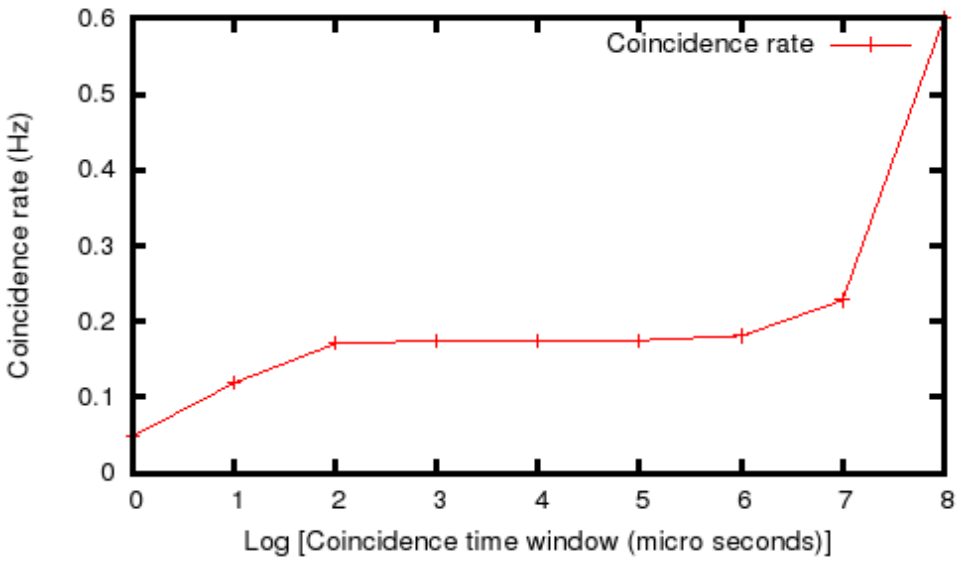

Figure 5.1 Coincidence rate versus time-window. The time-window is in units of $\pm\mu s$, and the rate is in Hz. X-axis is in log scale.

remains flat till the width is a few $10^3\mu s$, where it again rises, where the chance coincident events start to dominate. To find coincident events for cross calibration, we set the time window at $\pm 10.0\mu s$, i.e. a width of $20.0\mu s$. It has been confirmed visually from the coincident event display that these images show the same event (see figure 5.3). Once the window-width is fixed we need a set of selection criteria to choose events for cross calibration, and reject events that might be chance coincidences. To ascertain that both instruments triggered on the same Cherenkov shower, we compare the image parameters such as length, width, and the coordinates of the image-center. From figure 5.2 we see that the image parameters from both instruments match very closely. The ratio of the total-signal (sum of charges in all channels) is also fairly constant. Again, this confirms that events due to the same Cherenkov flash are being captured.

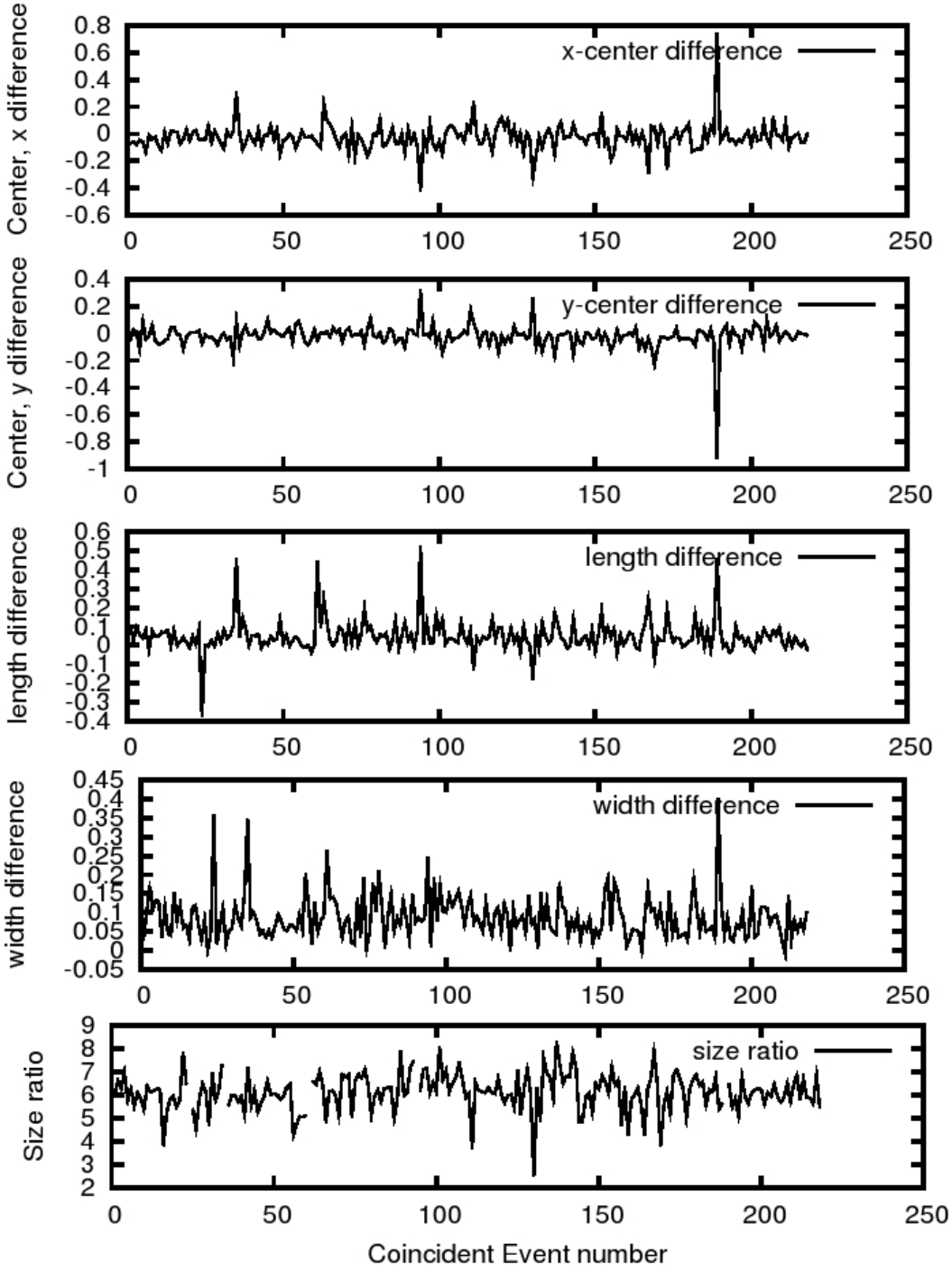

Figure 5.2 Ratio of image parameters of coincident pairs of SGARFACE and Whipple events.

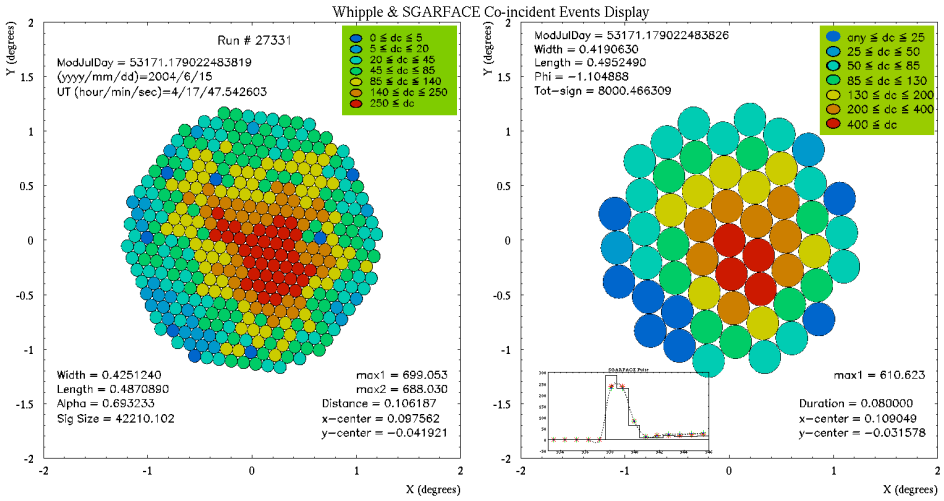

Figure 5.3 The display of a coincident event between the Whipple and the SGARFACE instrument. The left panel is the Whipple event display and the right one is the SGARFACE event display.

5.1.2 Coincident event display

A few coincident displays were developed, to visualize the images formed in the camera of both the instruments. Apart from the color coded charges in different pixels, some of the image parameters and the MJD of the event are also displayed, similar to the SGARFACE event displays. The total signal detected in the image, i.e. the sum of charges in all the channels is also displayed in the respective panels.

Figure 5.3 shows one of the coincident event displays. To visualize the steps in the SGARFACE software analysis, the pedestal and noise levels in the SGARFACE channels, as well as the image in the corresponding Whipple event the display shown in figure 5.4 is used.

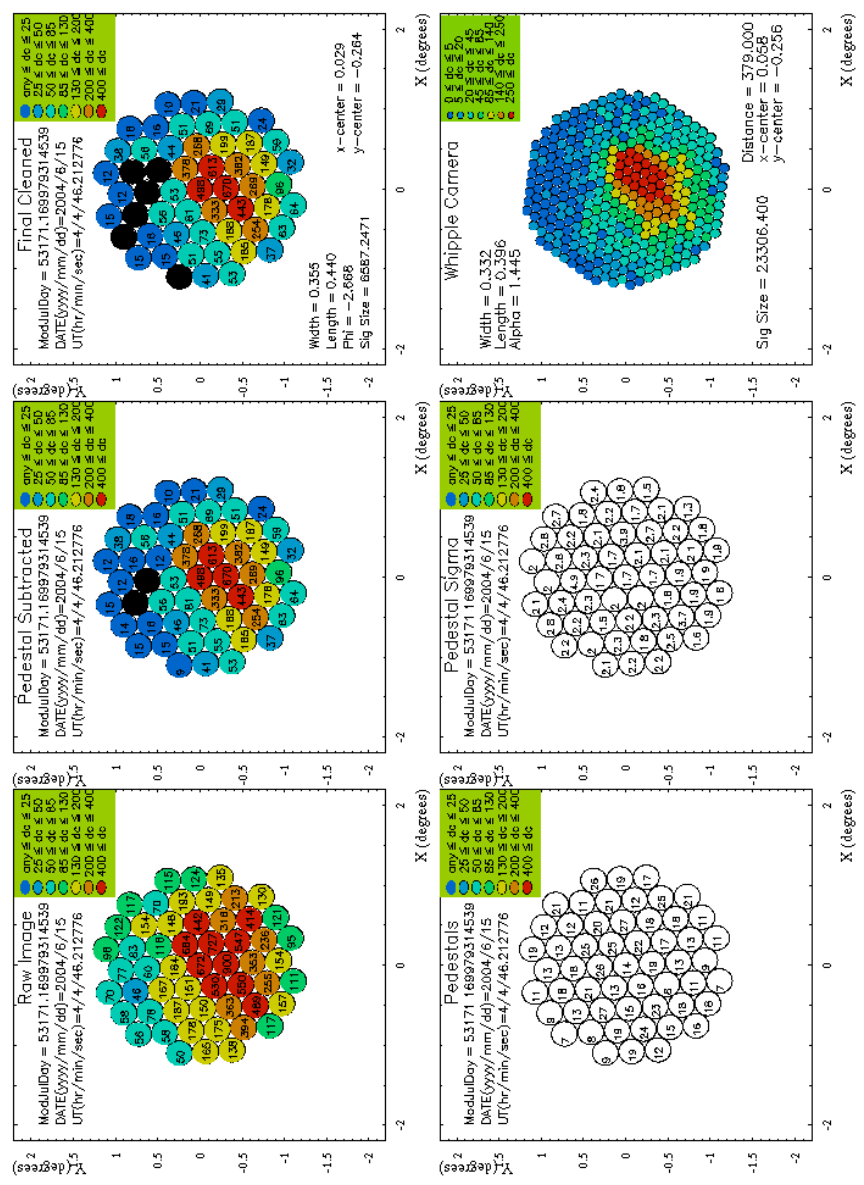

Figure 5.4 A coincident event display with different steps in the SGARFACE analysis shown. Top left panel is the SGARFACE charges without any pedestal subtraction or cleaning, top middle panel is with pedestal subtraction done, top right is with pedestal subtraction and cleaning. Bottom left and middle are the pedestal and sigma (noise) in the SGARFACE channels respectively, and bottom right is the Whipple display.

5.2 Calibration of SGARFACE using cosmic-ray events

From coincident events the comparison of charges and derivation of a d.c./p.e. for the SGARFACE instrument is described in this section.

5.2.1 Comparing SGARFACE and Whipple events

To reject chance coincidences, a selection criteria based on the image parameters, x-center and y-center is used. Image analysis gives us the center coordinates of the images formed in the two instruments. Over an entire day of data (of June 15, 2004), the difference in the x and y coordinates of the image-center in the two instruments, was found to have a standard deviation of $\approx$ 0.13° and $\approx$ 0.11°, respectively. A pair of coincident events, that had the difference of x-coordinate greater than 0.26°, and the difference in y-coordinates greater than 0.22°, were rejected. This selection cut rejects $\approx$ 2.3 % of the events. However, from the table 5.1, for a time window of 10 μs, we can estimate around 1 chance-coincidence for every 1740 coincident events, or 0.06 %. The 2.3 % events that we reject is $\approx$ 40 times greater than this. On visual inspection of the images of the rejected events, two characteristics were noted. A fraction of these events had extended images in the SGARFACE instrument with a wide dispersion in the arrival time (greater than 20 ns) of the signal in the pixels. Therefore these showers had a too large a time-dispersion to allow Whipple to record the full shower profile, with its limited integration time of 20 ns. Whereas SGARFACE with its longer integration time captured the entire shower profile, resulting in a extended image with different image characteristics. The other fractions of the rejected events showed hardly any charge detected in SGARFACE. This suggests that these could be accidental coincidences. On top of this, since we already reject events which saturate SGARFACE pixels, the number of cosmic-ray showers that could be potentially trigger both instruments simultaneously is further reduced.

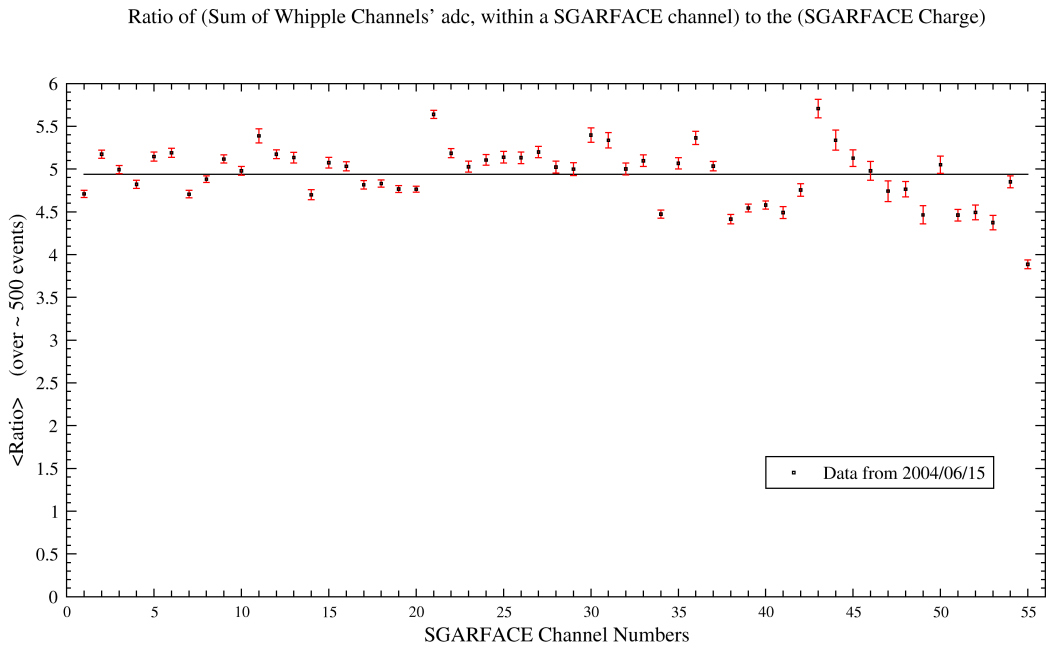

Figure 5.5 Ratio ($\langle r_j \rangle_n$) of integrated Whipple charge to the SGARFACE charge for all 55 SGARFACE channels for one night of observations.

The SGARFACE channels are formed by summing up a number (usually 7, except near the outer periphery of the camera, see figure 3.3) of Whipple channels. Thus the charge in the corresponding Whipple Channels within a SGARFACE channel have to be summed together, before comparing it to the SGARFACE charge.

The ratio of Whipple to SGARFACE charges, its average value over a night's run, and the error in the average value are denoted by the following terms (for j^{th} SGARFACE channel):

$$
\begin{aligned}
r_j &\equiv \left[\frac{\sum_{i=1}^{7} W_{ij}}{S_j}\right];\ \textit{is the ratio of the Whipple to SGARFACE charge},\\
\langle r_j \rangle_n &\equiv \frac{\sum_1^n r_j}{n};\ \textit{is the mean of } r_j \textit{ over } n \textit{ coincident events},\\
\sigma_{jn} &\equiv \sqrt{[\langle r_j^2 \rangle_n - \langle r_j \rangle_n^2]},\ \textit{the standard deviation}\\
\epsilon_{jn} &\equiv \frac{\sigma_{jn}}{\sqrt{n}},\ \textit{the error.}
\end{aligned}
$$

The plot of $\langle r_j \rangle_n$ against the SGARFACE channel number is shown in figure 5.5 (for

data from other days, please see Appendix E); the error bars are ϵ_{jn}.

5.2.2 Deriving d.c./p.e. for SGARFACE

The ratio of charges $\langle r_j \rangle_n$ of a SGARFACE pixel can now be used to find the overall gain of SGARFACE. For the Whipple TeV system the gain of the instrument has been calibrated in the past. The gain of Whipple was $\sim 2.4 \ \pm 0.1 \ d.c./p.e._{(W)}$, during the period of June, 2004. The gain in the electronics of SGARFACE can be found in terms of a d.c./p.e. for each channel or in terms of an average d.c./p.e. for the entire instruments. In the Whipple analysis, since nitrogen flasher events are used to normalize the relative-gain over all pixels, only a single overall d.c./p.e. is used for all the channels. However in the SGARFACE instrument since a similar gain-normalization is not possible (see section 4.1) it would be advantageous to have a d.c./p.e ratio for each individual pixel. By doing so the relative gain of different SGARFACE pixels can be estimated from the d.c./p.e. for the pixels. An overall d.c./p.e for the entire camera is also calculated. The d.c./p.e. for a SGARFACE pixel ($d.c./p.e._{(S,j)}$, for the j^{th} pixel) is obtained by dividing the $d.c./p.e._{(W)}$ by the charge ratio of Whipple to SGARFACE $\langle r_j \rangle_n$ in the same pixel. For example consider channel number 7 and charge ratio from June 15, 2004 data.

$$\begin{aligned} \langle r_7 \rangle \ &= \ 4.706 \pm 0.044; \ So \ d.c./p.e._{(S,7)} \ = \frac{d.c./p.e._{(W)}}{\langle r_7 \rangle} \\ &= \ \frac{2.4 \pm 0.1}{4.706 \pm 0.044} \approx 0.51 \pm 0.02 \approx 0.5 \ d.c./p.e._{(S,7)} \end{aligned}$$

(*errors are lost when we take only the significant digits we can consider*)

Similarly a d.c./p.e. value can be calculated for all the other channels. To get an overall d.c. to p.e ratio for the instrument we can get the mean d.c./p.e from the distribution in all 55 channels; or get the average charge ratio in all the channels and proceed as done above for a individual pixel.

The histogram of the d.c./p.e. value of the 55 channels (calculated from one day of data, of June 15, 2004) is shown in figure 5.6. The Gaussian fit and fit parameters are

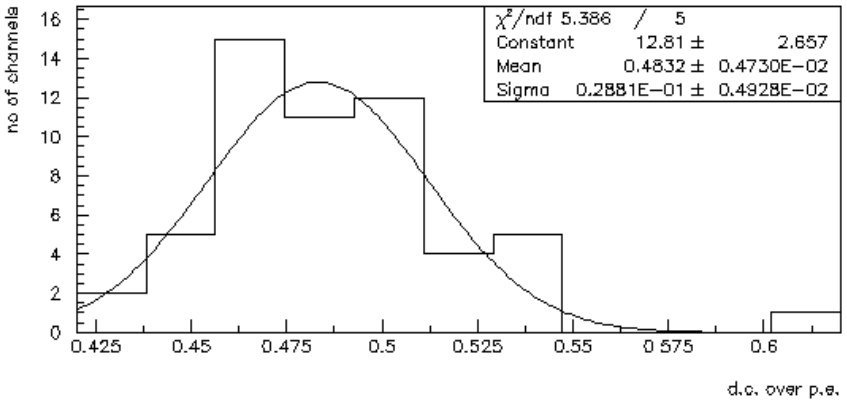

Figure 5.6 Histogram of d.c./p.e. of all 55 channels. The d.c./p.e. for each channel was calculated from an entire day (06/15/2004) of coincident data. The Gaussian fit and the fit parameters are also shown

also shown in the figure. From the mean and standard deviation of the fit, we get an overall d.c/p.e. of $\approx 0.483 \pm 0.005$ $d.c./p.e._S$ for the SGARFACE instrument.

Using the second method, we see that the average $\langle r_j \rangle_n$ over all the 55 SGARFACE pixels, denoted by $R_{(W/S)}$ is $\approx 4.939 \pm 0.045$ (see figure 5.5), from the same day of data. Thus we get

$$average\ over\ all\ SGARFACE\ pixels: \ (\langle r_j \rangle_n)_{avg} \ = \ R_{(W/S)} \ = \ 4.939 \pm 0.045$$

$$Thus\ for\ SGARFACE: \ \frac{d.c./p.e._{(W)}}{R_{(W/S)}} \ = \ \frac{2.4 \pm 0.1}{4.94 \pm 0.05}$$

$$\approx \ 0.5\ d.c./p.e._{(S)}$$

(*again, errors are lost when we take only the significant digits we can consider*)

This concludes the cross-calibration of SGARFACE against Whipple. In practice, the SGARFACE instrument should ideally be calibrated for each day of observation. The variation in the $d.c./p.e._{(S)}$ over different days of observations, would give a measure for the stability of the instrument, as well as enable the data to be accurately analyzed. The variation of $\langle r_j \rangle_n$ for a few channels over a period of five consecutive days is shown in

figure 5.7 (for other channels see Appendix E, figures E.5 through E.13). A first look at the variations suggests that the charge ratio in a channel is quite stable, and the variations are statistical in nature, which means the instrument is reasonably stable.

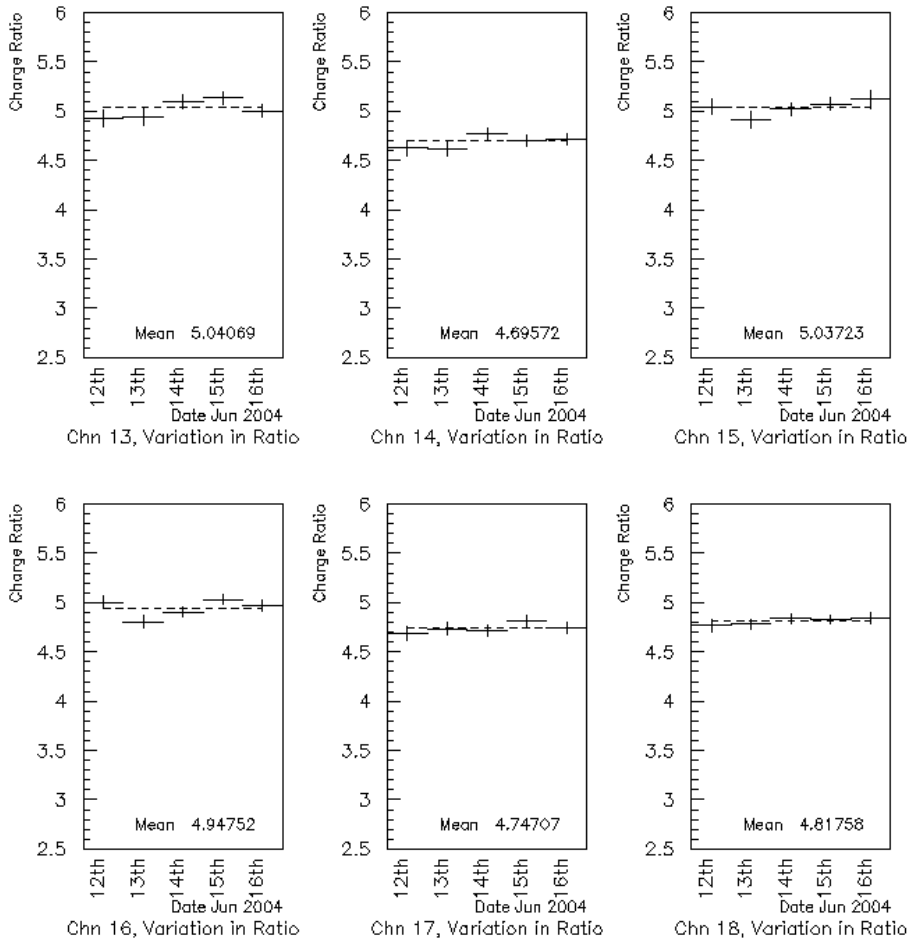

Figure 5.7 Variation of the Ratio ($\langle r_j \rangle_n$) of integrated Whipple charge to the SGARFACE charge, over 5 days of observation, for channels 13 through 18. The average ratio over the five days is displayed in the plots.

CHAPTER 6. CONCLUSION

To conclude a summary of the work done is given, and the result obtained is discussed. This is followed by suggestions for improvement and future work.

6.1 Results form this work

In this work, a software system was developed to analyze SGARFACE events. The analysis gives the charge collected in each pixel, the image parameters, and produces various image displays. Cosmic-ray events triggering both Whipple and SGARFACE, were used to compare the charges recorded by both instruments to derive a ≈ 0.5 d.c./p.e. value for SGARFACE. This overall measure of the electronics gain for SGARFACE has been calculated in two other ways. Stephan LeBohec had done a direct calculation from the electronics, which gave ≈ 0.38 d.c./p.e. (private communication), whereas Martin Schroedter used a laser flasher to get a value of 0.64 ± 0.03 d.c./p.e. (see Schroedter et al. [47]). The direct calculation method is described in Appendix C. In the laser flasher method, the camera is illuminated for a short duration of 4 ns with a special laser flasher. The charge ratio of SGARFACE to Whipple pixels is then calculated, and the d.c./p.e. for SGARFACE is derived in a similar fashion as in this work. With cross calibration accomplished, and the measure of the overall sensitivity of the SGARFACE instrument obtained, the data can now be analyzed to search for long duration burst-like events.

6.2 Future work

From the experience and knowledge gained about the SGARFACE system during the development of the analysis and cross calibration, some improvements that can be implemented in the software and the hardware, are discussed in section 6.2.2, preceded by an outline of the search for long duration events in the existing SGARFACE data.

6.2.1 Search for potential burst events

The immediate task to be done following the cross calibration would be to prepare a software suite to analyze the data and look for burst like events. This work is currently underway and a preliminary search on a subset of SGARFACE data has been done. A very brief description is given in this section.

To look for burst events, first the duration of the events in the SGARFACE data has to be calculated. This is achieved by summing up the signal-trace of all the 55 pixels in the SGARFACE camera, to get the integrated signal trace in the instrument. The pulse due to the Cherenkov flash occurs around the 938th data sample in each pixel that collects photons from the flash. The width of the corresponding pulse in the integrated signal trace is calculated. This width (FWHM of the pulse) is a measure of the duration of the event. The events that have duration greater than 100 ns are then selected for further analysis.

A duration greater than 100 ns is the first requirement for a burst like event, from evaporating black holes according to the Hagedorn model. But this by itself is not a sufficient condition for detection of a PBHs. Sometimes long duration events might be recorded from single particle initiated air-showers, when the primary γ-ray has a large angle of incidence wit respect to the earth's atmosphere. This is because in such cases the shower development takes place over a longer length along the shower axis, and the

[1]The signal-trace in each channel consists of 1753 data samples, see figure 4.1

difference between the time of flight of the Cherenkov photons from the various parts of the shower might arrive at the telescope with a time spread. However, such cases can be easily identified since the time of arrival of the signal in different pixels is likely to show this time spread. Also, for burst-like images we expect to see roughly circular images with a width of around one degree. Currently the code is being developed to calculate the event duration, and select long duration events. The analysis for checking the time-dispersion between different PMTs is also underway. Future work would involve setting up a set of selection criteria for rejecting events based on the size and shape, as well as the time-dispersion.

6.2.2 Software and hardware improvements

Apart from this, the software analysis system can be improved by implementing a flat-fielding for the SGARFACE pixels. It was mentioned in section 4.1, that flat-fielding is not possible by using nitrogen flasher events, due to saturation of the electronics. In the future, for event analysis the relative gain of SGARFACE pixels should be normalized by some means. One possibility would be to use the relative gain of individual Whipple pixels and indirectly estimate the corresponding gains for the SGARFACE pixels.

The SGARFACE instrument was designed to measure low energy extended showers from burst of γ-rays. Thus to detect slight excesses in the signal for low energy events, the data-samples can be aggregated in larger groups before noise cleaning and charge calculation is done. This would compliment the hardware MTS trigger, that has a multiple signal integration time scale.

In terms of the hardware, probably not much can be done with the existing system on Whipple 10 m. But in the future, if a system similar to SGARFACE is installed in the VERITAS array of telescopes, some improvements could be possible. The present system seems to have some capacitive discharge and signal reflection due to impedance mismatch in the circuits. This should be studied in detail and the new system could be

designed to minimize this. The Flash ADC in the current system have a capacity of 8-bits, corresponding to a dynamic range of 0 *to* 255 *d.c.*. Though this should be sufficient for low energy burst events, for cross calibration using bright cosmic-ray events, the system gets saturated and the signal profile cannot be contained. Also due to this reason it becomes impractical to measurement the relative gain of different pixels using nitrogen flasher or similar methods. The new systems should preferably have FADC with larger dynamic ranges.

It remains to be seen if the future work in analyzing the existing SGARFACE data yields any interesting events. Even a null result would be interesting to put stronger upper limits to the PBH evaporation rate. But any such conclusion can only be made after detail analysis of a few years of SGARFACE data.

APPENDIX A. PEDESTAL DISTRIBUTION OF DIFFERENT CHANNELS

Two methods can be used to calculate the pedestal in each channel. One is by finding the mean value of the d.c. in the first 700 data-points, and the second one is by fitting a Gaussian to the histogram of the data in the same range. For a typical event the plots of the 55 channels is shown in figure A.1 through figure A.5. Each plot has the histogram of the signal value in the first 700 data-points, and the Gaussian fit to it (curve fitting and plotting done using PAW). The x-axis is the d.c. value, and the y-axis is the number of data-points. The value given as the boxed parameter "P2" is the pedestal as found by the Gaussian fit, and "code ped" gives the pedestal value found by getting the mean signal in two iterations, as described in chapter 4.

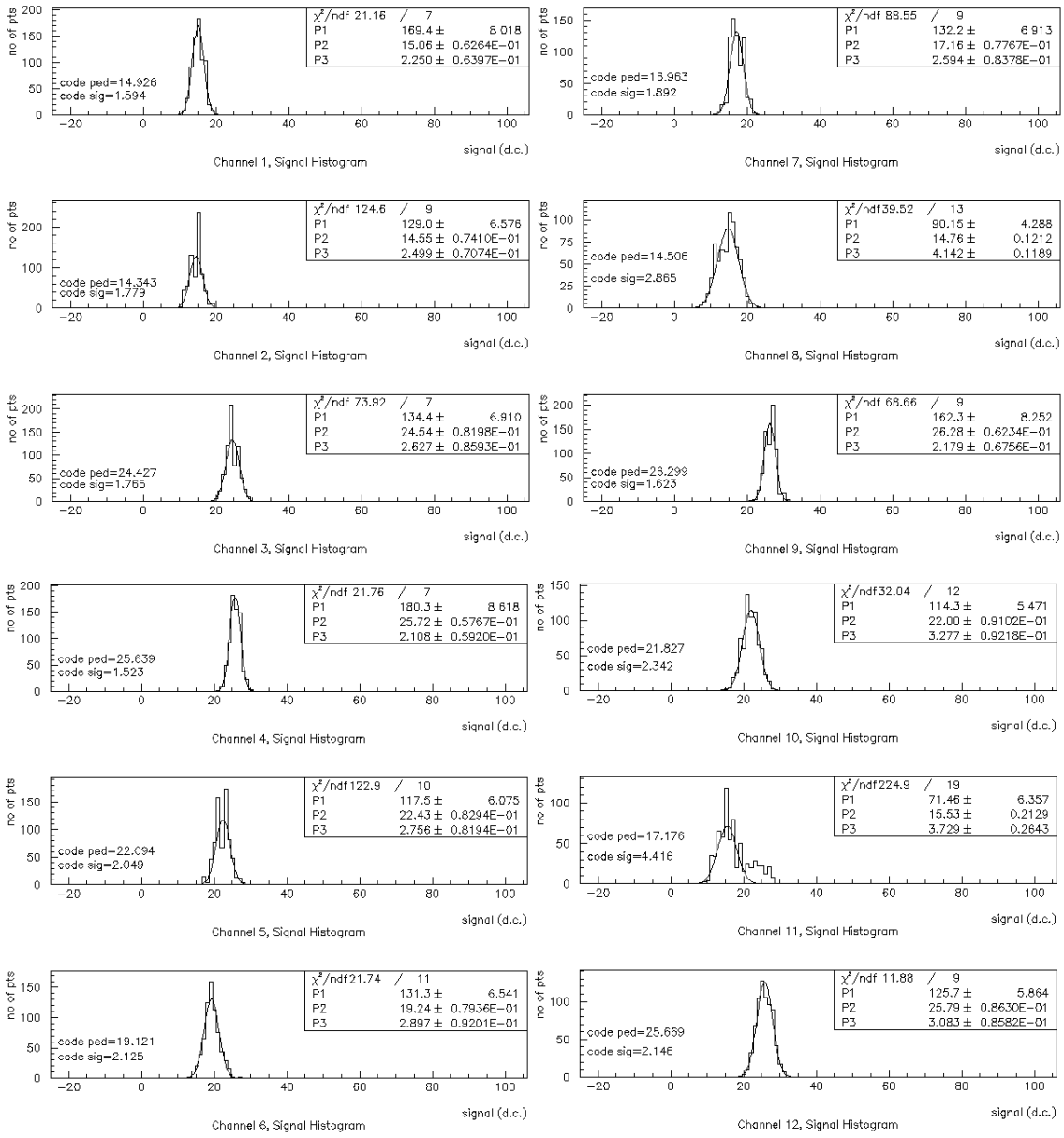

Figure A.1 Histogram and Gaussian fit for channels 1 through 12 for a typical event. The values of the Gaussian curve fitting, are given in the boxes. The goodness of the fit is given by the 'χ^2/ndf'; where 'ndf' is the number of bins used for curve fitting. The parameters P1, P2, and P3 stand for the height, x-position (pedestal value), and the width respectively. The calculated Pedestal and the standard deviation of the pedestal are shown on the left side of the panels as 'code ped' and 'code sig'.

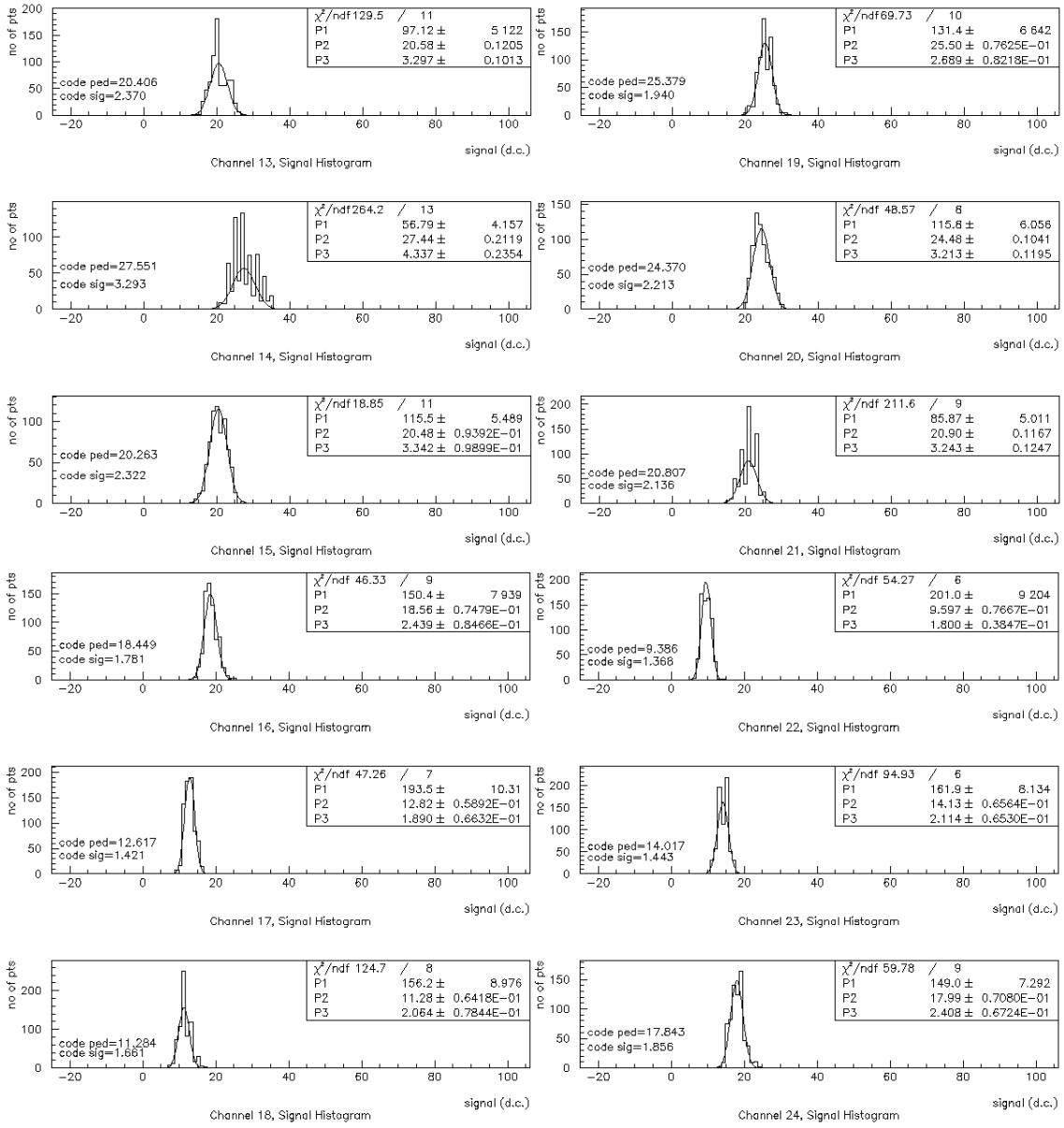

Figure A.2 Histogram and Gaussian fit for channels 13 through 24 for a typical event. The values of the Gaussian curve fitting, are given in the boxes. The goodness of the fit is given by the 'χ^2/ndf'; where 'ndf' is the number of bins used for curve fitting. The parameters P1, P2, and P3 stand for the height, x-position (pedestal value), and the width respectively. The calculated Pedestal and the standard deviation of the pedestal are shown on the left side of the panels as 'code ped' and 'code sig'.

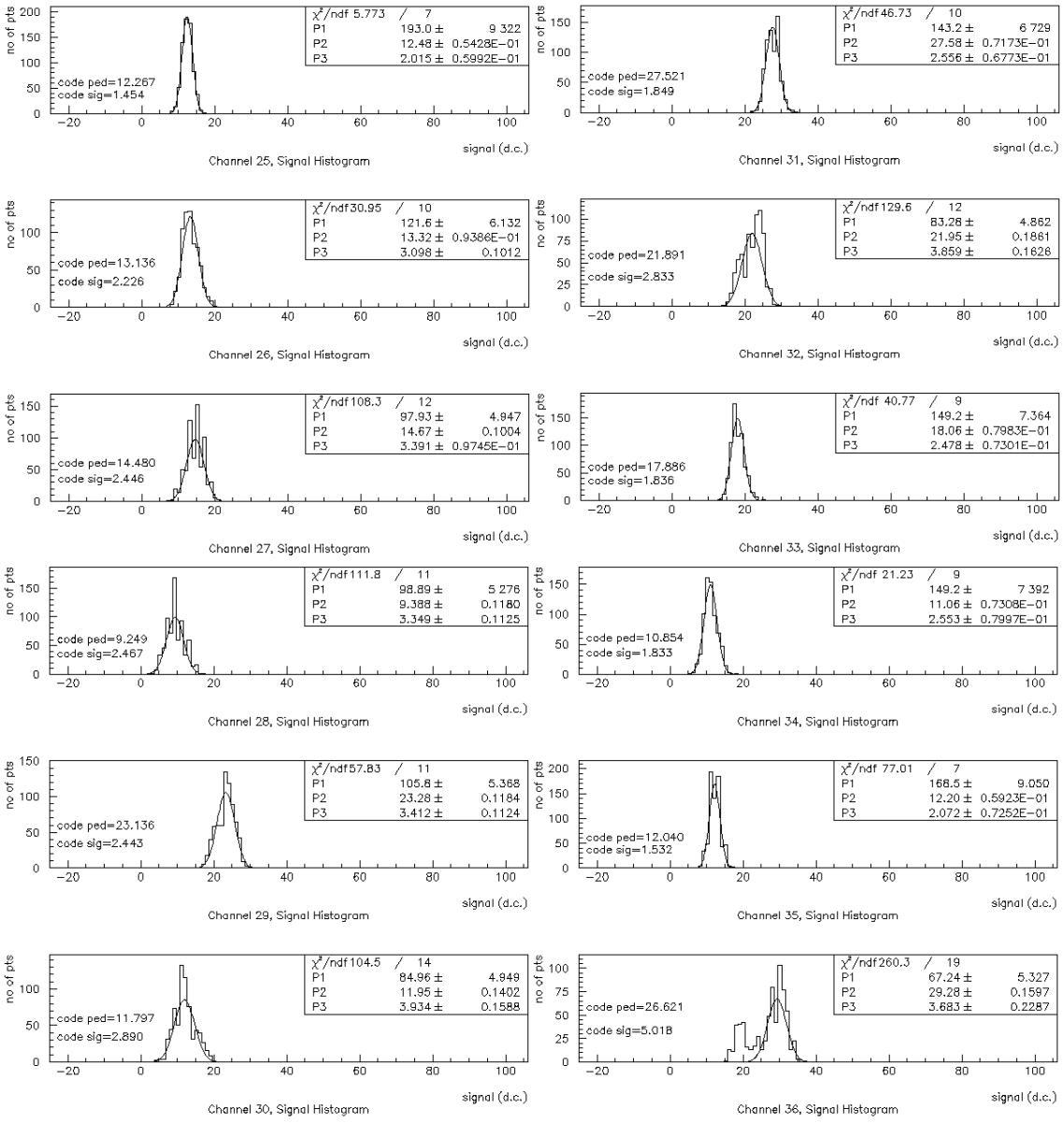

Figure A.3 Histogram and Gaussian fit for channels 25 through 36 for a typical event. The values of the Gaussian curve fitting, are given in the boxes. The goodness of the fit is given by the 'χ^2/ndf'; where 'ndf' is the number of bins used for curve fitting. The parameters P1, P2, and P3 stand for the height, x-position (pedestal value), and the width respectively. The calculated Pedestal and the standard deviation of the pedestal are shown on the left side of the panels as 'code ped' and 'code sig'.

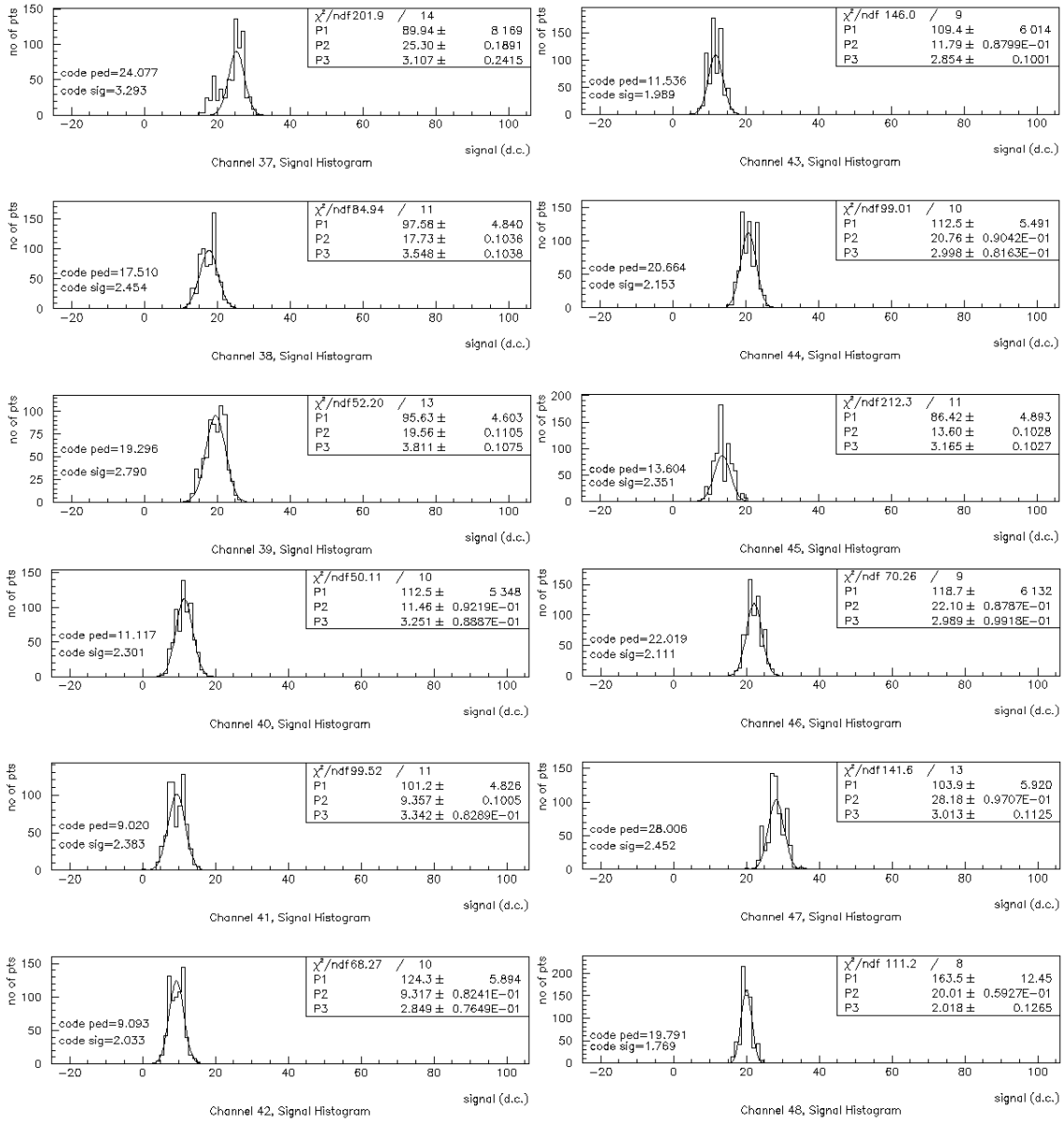

Figure A.4 Histogram and Gaussian fit for channels 37 through 48 for a typical event. The values of the Gaussian curve fitting, are given in the boxes. The goodness of the fit is given by the 'χ^2/ndf'; where 'ndf' is the number of bins used for curve fitting. The parameters P1, P2, and P3 stand for the height, x-position (pedestal value), and the width respectively. The calculated Pedestal and the standard deviation of the pedestal are shown on the left side of the panels as 'code ped' and 'code sig'.

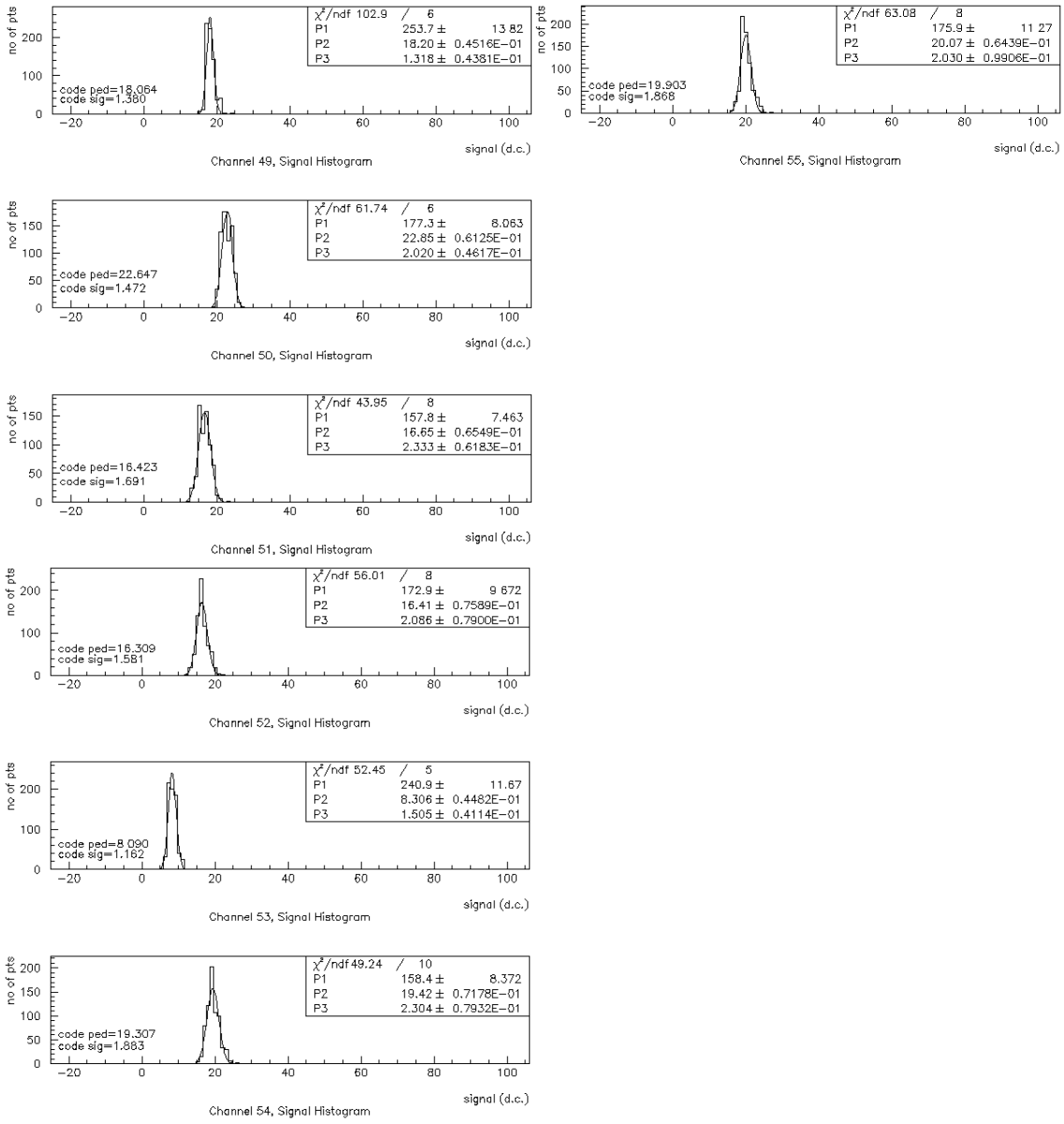

Figure A.5 Histogram and Gaussian fit for channels 49 through 54 for a typical event. The values of the Gaussian curve fitting, are given in the boxes. The goodness of the fit is given by the 'χ^2/ndf'; where 'ndf' is the number of bins used for curve fitting. The parameters P1, P2, and P3 stand for the height, x-position (pedestal value), and the width respectively. The calculated Pedestal and the standard deviation of the pedestal are shown on the left side of the panels as 'code ped' and 'code sig'.

APPENDIX B. IMAGE PARAMETERS

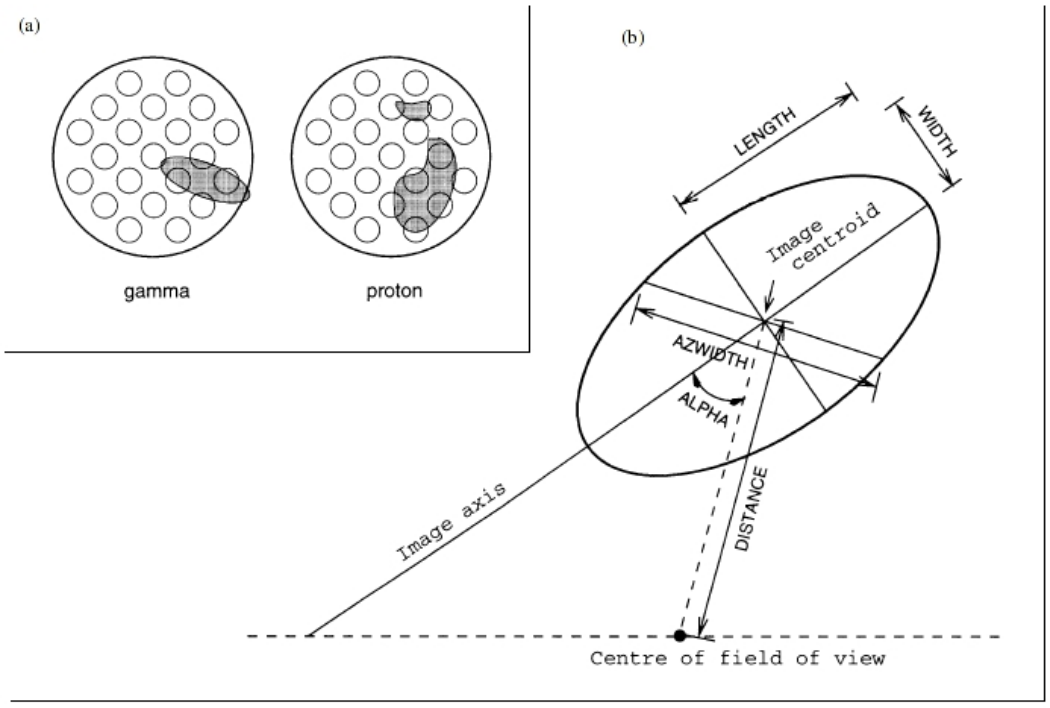

Figure B.1 (a) Schematic representation of the image formed on the focal plane instrument of an IACT due to a γ-ray event and a proton event. Note the smooth elliptical shape of the γ-ray image, and its pointing direction toward the center of field of view. (b) The image parameters of a γ-ray image on the focal plane. Due to their regular shape and orientation, these parameters are used to reject cosmic-ray events from the data. Figure from Ong [41]

The imaging technique uses the shape and orientation of the image formed at the focal plane to differentiate whether the air-shower was initiated by a γ-ray photon or a cosmic-ray particle (mostly protons). The characteristic image-shape and orientation of

a γ-ray initiated air-shower and a proton initiated shower is shown in the figure B.1(a). The narrow and well defined elliptical shape can be parameterized by its length, width, and eccentricity. The orientation of the image is expressed in α, which is the angle between the major axis of the image and the line joining the image centroid to the center of field of view. This was first suggested by Hillas [22].

The coordinates in the focal-plane are defined in terms of x and y in units of degrees in the sky. Some of the moments and parameters are defined below.

moments:

$$\begin{aligned}
\langle x \rangle &= \frac{\sum n_i x_i}{\sum n_i} \\
\langle y \rangle &= \frac{\sum n_i y_i}{\sum n_i} \\
\langle x^2 \rangle &= \frac{\sum n_i x_i^2}{\sum n_i} \\
\langle y^2 \rangle &= \frac{\sum n_i y_i^2}{\sum n_i} \\
\langle xy \rangle &= \frac{\sum n_i x_i y_i}{\sum n_i}
\end{aligned}$$

spreads:

$$\begin{aligned}
\sigma_{x^2} &= \langle x^2 \rangle - \langle x \rangle^2 \\
\sigma_{y^2} &= \langle y^2 \rangle - \langle y \rangle^2 \\
\sigma_{xy} &= \langle xy \rangle - \langle x \rangle \langle y \rangle
\end{aligned}$$

Hillas parameters:

$$\begin{aligned}
d &= \sigma_{y^2} - \sigma_{x^2} \\
s &= \sqrt{d^2 + 4(\sigma_{xy})^2} \\
u &= 1 + \frac{d}{s} \\
v &= 2 - u \\
length &= \sqrt{\frac{\sigma_{x^2} + \sigma_{y^2} + s}{2}}
\end{aligned}$$

$$
\begin{aligned}
width &= \sqrt{\frac{\sigma_{x^2} + \sigma_{y^2} - s}{2}} \\
distance &= \sqrt{\langle x \rangle^2 + \langle y \rangle^2} \\
miss &= \sqrt{\frac{1}{2}(u\langle x \rangle^2 + v\langle y \rangle^2) - \left(\frac{2\sigma_{xy}\langle x \rangle \langle y \rangle}{s}\right)} \\
\alpha &= sin^{-1}\left(\frac{miss}{distance}\right) \\
azwid &= \sqrt{\frac{\langle x \rangle^2 \langle y^2 \rangle - 2\langle x \rangle \langle y \rangle \langle xy \rangle + \langle x^2 \rangle \langle y \rangle^2}{distance^2}}
\end{aligned}
$$

This is not the complete list of Hillas parameters, but these are the parameters that are usually used for image cleaning. For an extensive list refer to [37].

APPENDIX C. DIRECT CALCULATION OF d.c./p.e.

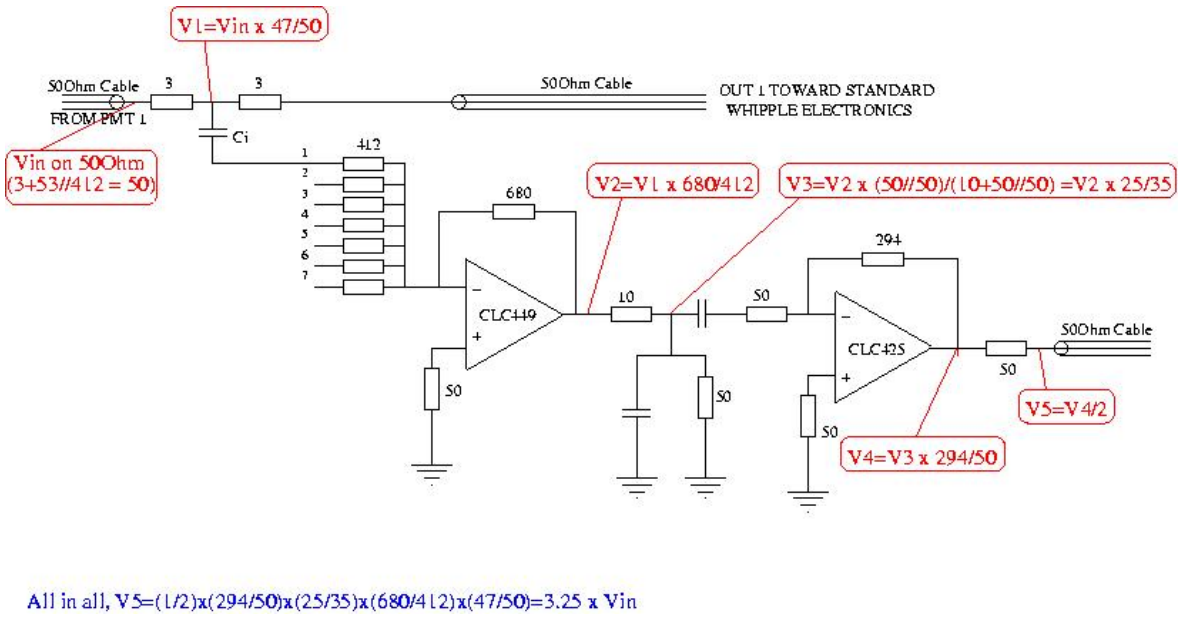

Figure C.1 Schematics of the SGARFACE electronics, showing the various op-amps of the splitter summer module. Here the calculation of the voltage gain, in the circuit is shown. From Stephan LeBohec (personal communication)

The d.c. to p.e. ratio can be calculated from the overall gain in the PMT, the voltage gain in the circuit, the impedance of the cables, the FADC conversion factor, and digitization rate of the FADC. We have

$$Overall\ gain\ in\ splitter\ summer\ =\ 3.25$$

$$PMT\ gain\ =\ 1.1 \times 10^{6}$$

$$FADC\ coversion\ factor\ =\ 7.84 \times 10^{-3}\ Cd.c.^{-1}$$

$$FADC\ board\ gain\ =\ 3.0$$

$$Cable\ Impedance\ =\ 50\ \Omega$$

$$Digitization\ Rate\ =\ 20\ ns$$

$$Thus,\ S_{d.c./p.e.} = (1.1{\times}10^{6}){\times}(1.6{\times}10^{-19}){\times}50{\times}3.25{\times}3.0\left(\frac{1}{7.84\times10^{-3}\times20\times10^{-9}}\right) = 0.547$$

This calculation neglects the signal loss in the cables. Assuming a signal loss of $\approx 30\%$, we would get ≈ 0.38 $d.c./p.e.$ for SGARFACE.

APPENDIX D. EVENT DISPLAYS

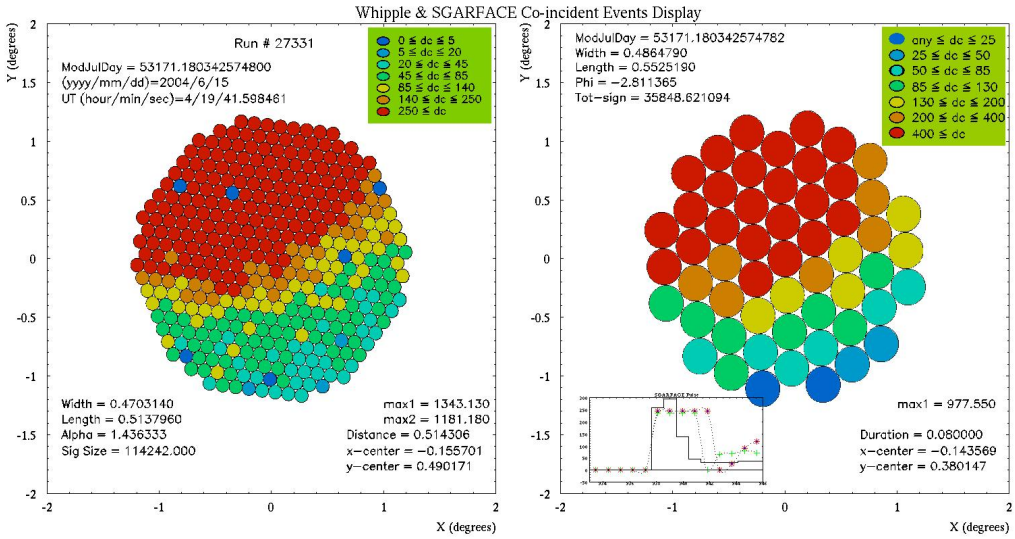

Figure D.1 Coincident event Display

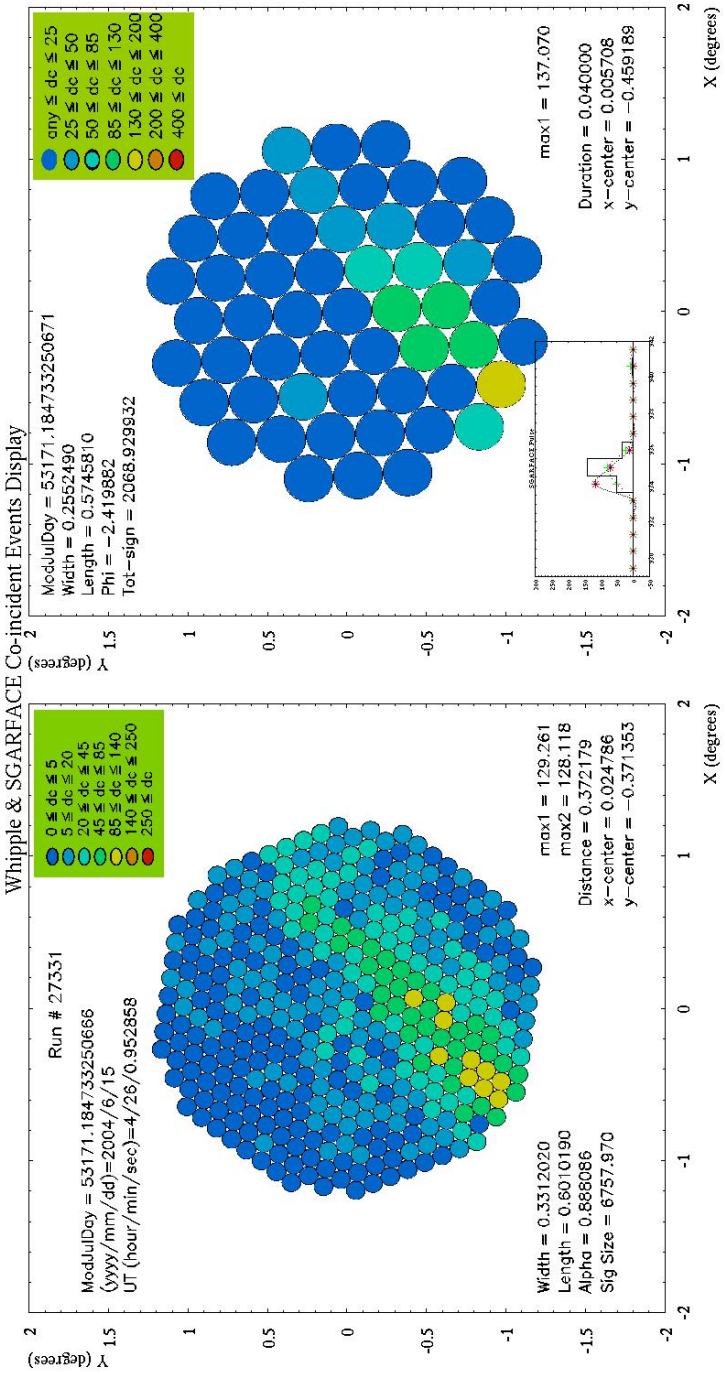

Figure D.2 Coincident event Display

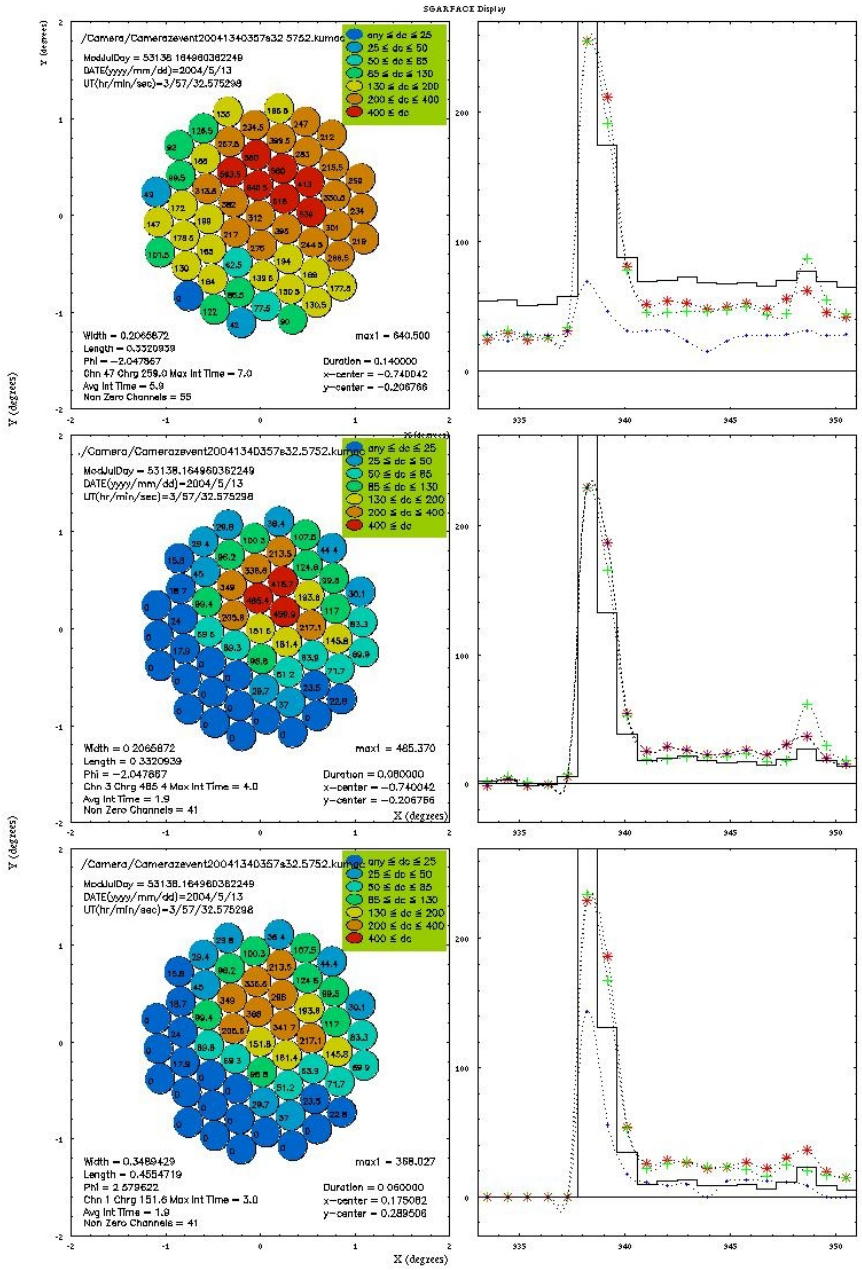

Figure D.3 This SGARFACE event display shows the stages in software analysis. The display of the camera is on the left sides and the right side panels show the three hottest pixels for the corresponding stage. The top images are the raw data, the middle images are after pedestal subtraction, and the bottom images are after pedestal subtraction and signal cleaning of 4σ.

APPENDIX E. CHARGE RATIO

The ratio of charge detected in the SGARFACE pixels and the corresponding Whipple pixels, gives us the ratio of the overall gain in the two instruments. This ratio is then used to cross-calibrate the SGARFACE system. For details see chapter 4, and 5.

Here the ratio of the charges for all the 55 SGARFACE pixels, is shown for 4 days of data, followed by the plots showing how the ratio of charges varies over 5 days. For the data of 2004/06/15 see figure 5.5, and for variations in channels 13 through 18 see figure 5.7.

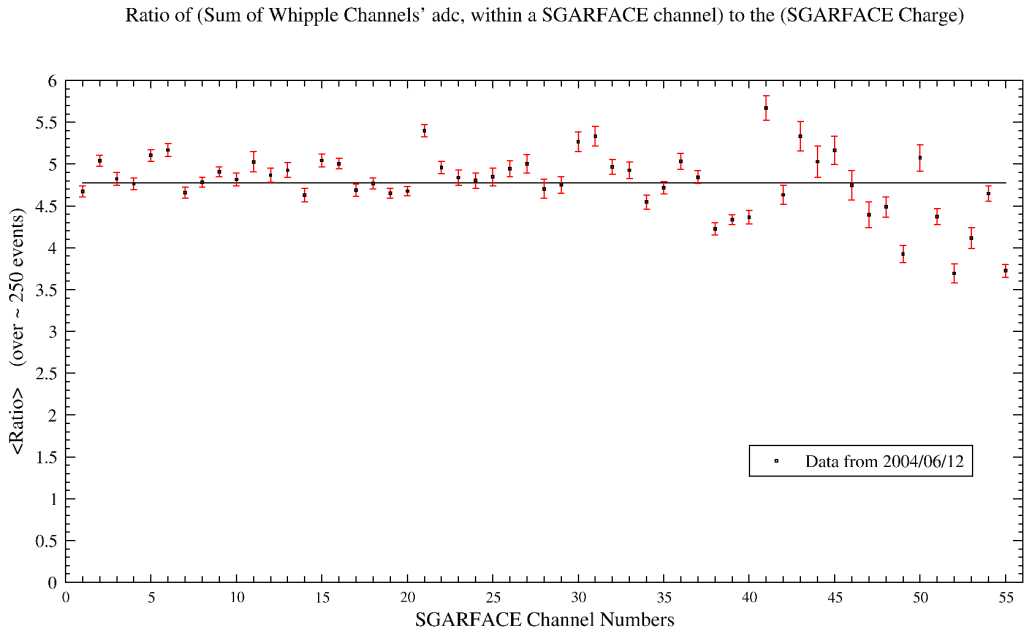

Figure E.1 Ratio ($\langle r_j \rangle_n$) of integrated Whipple charge to the SGARFACE charge for all 55 SGARFACE channels. Data from the date 2004/06/12.

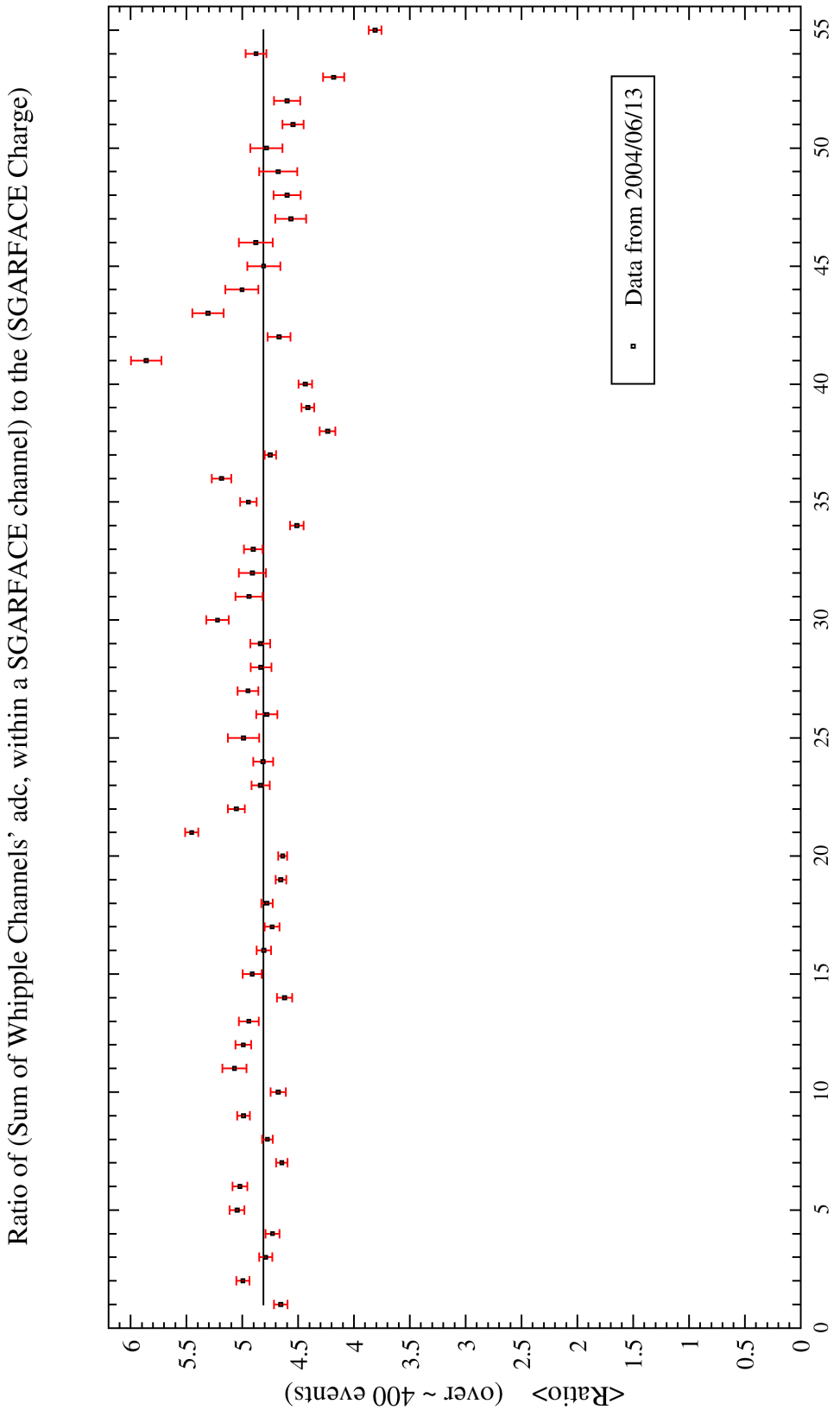

Figure E.2 Ratio ($\langle r_j \rangle_n$) of integrated Whipple charge to the SGARFACE charge for all 55 SGARFACE channels. Data from the date 2004/06/13.

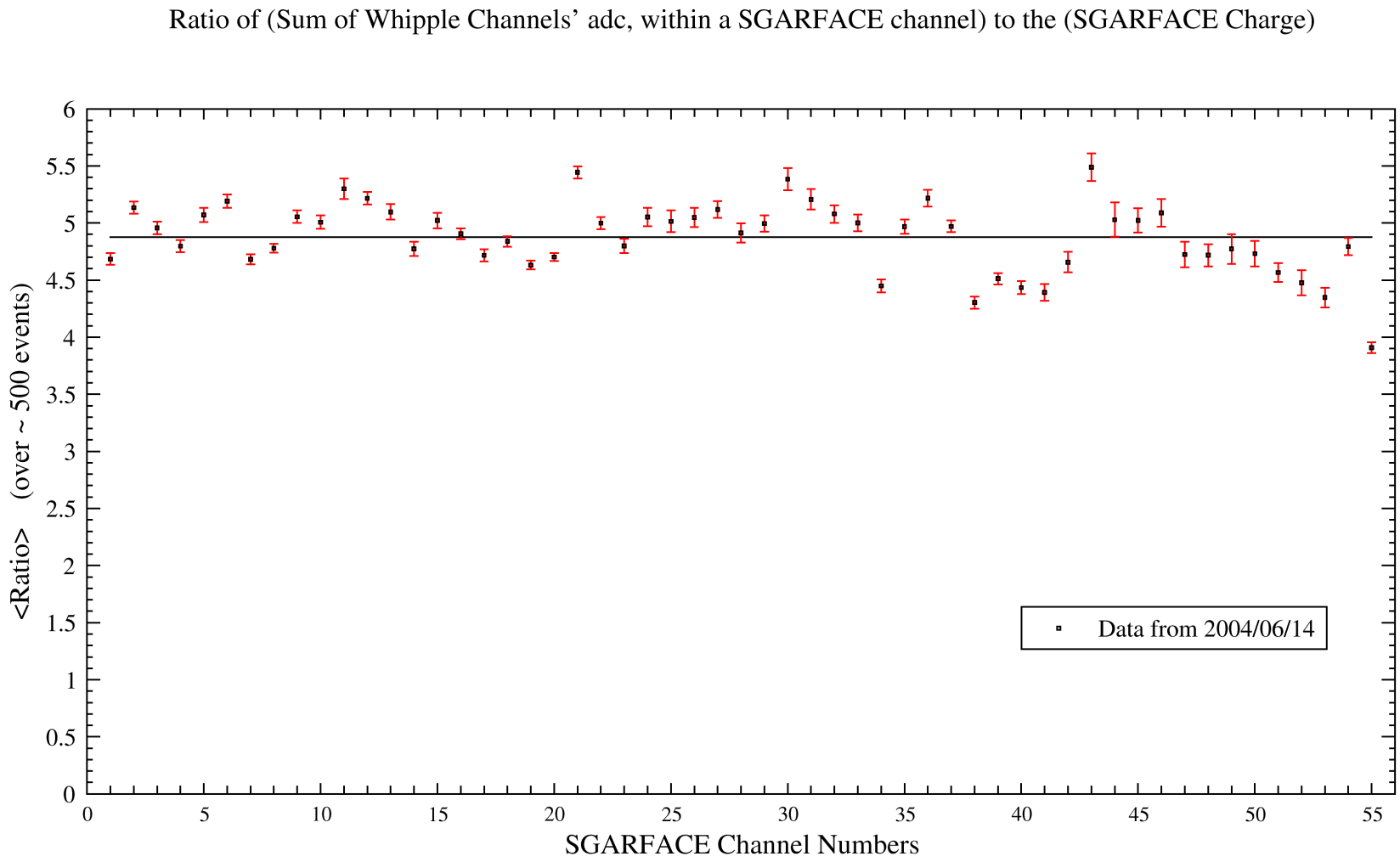

Figure E.3 Ratio ($\langle r_j \rangle_n$) of integrated Whipple charge to the SGARFACE charge for all 55 SGARFACE channels. Data from the date 2004/06/14.

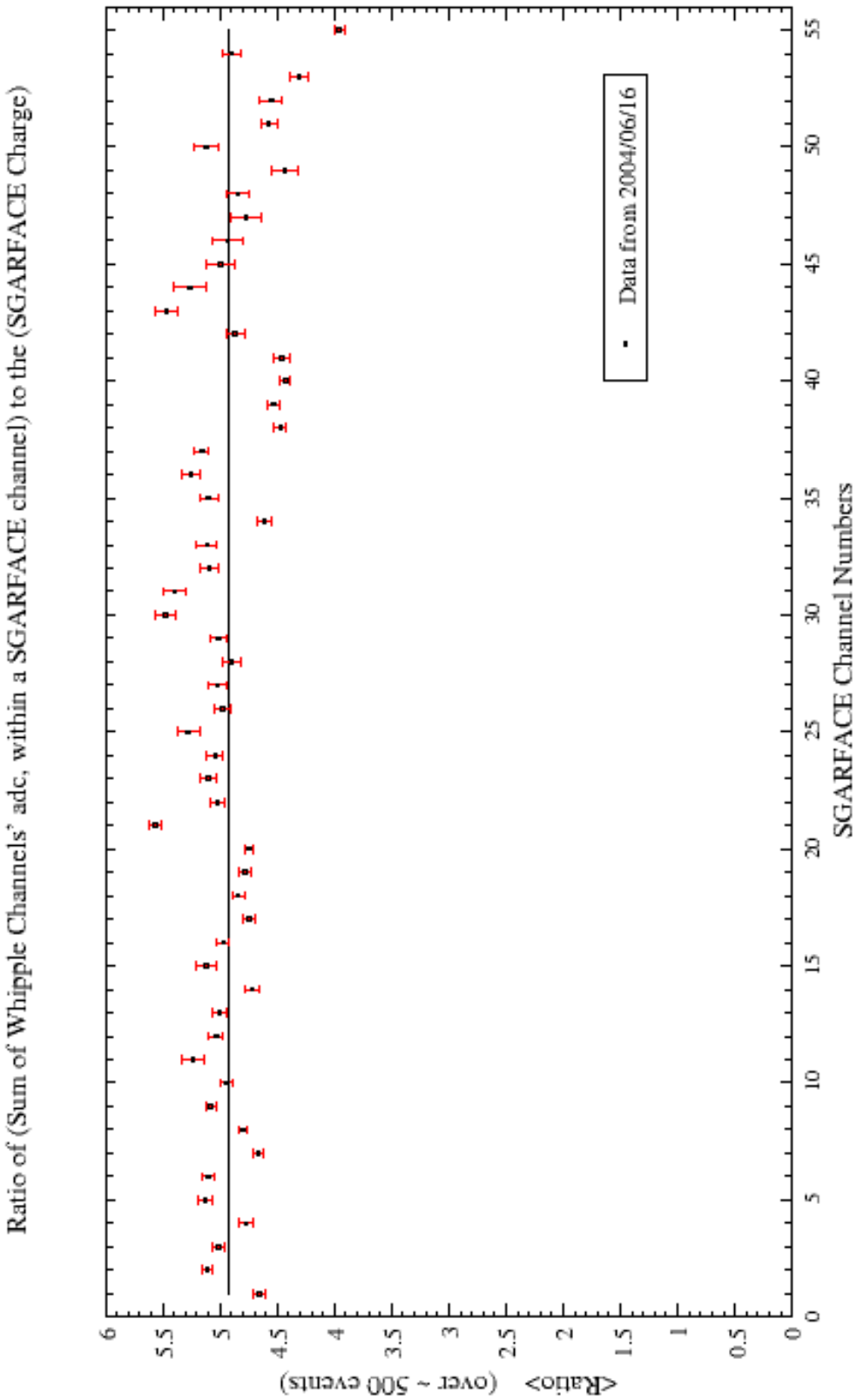

Figure E.4 Ratio ($\langle r_j \rangle_n$) of integrated Whipple charge to the SGARFACE charge for all 55 SGARFACE channels. Data from the date 2004/06/16.

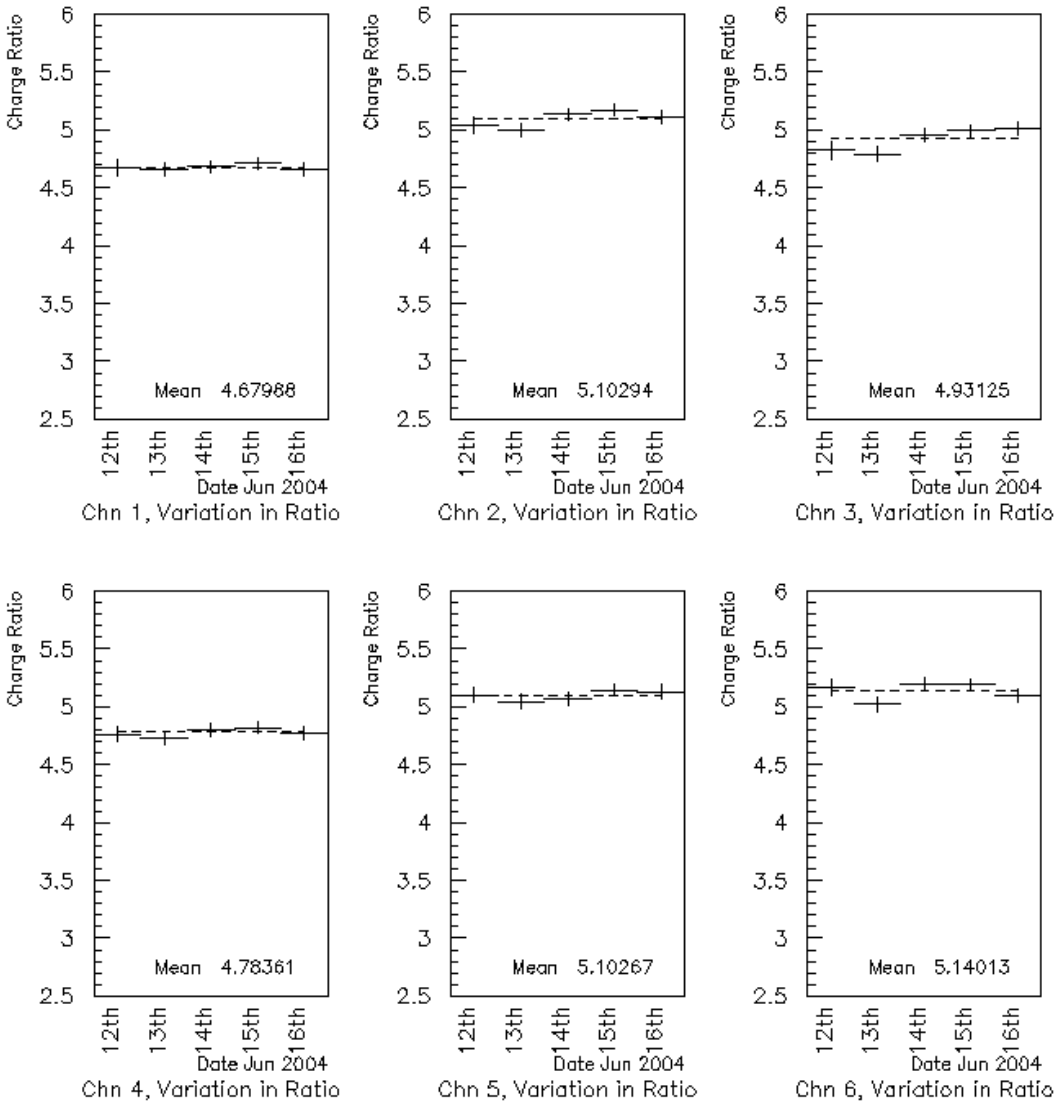

Figure E.5 Variation of the Ratio ($\langle r_j \rangle_n$) of integrated Whipple charge to the SGARFACE charge, over 5 days of observation, for channels 1 through 6. The average ratio over the five days is displayed in the plots.

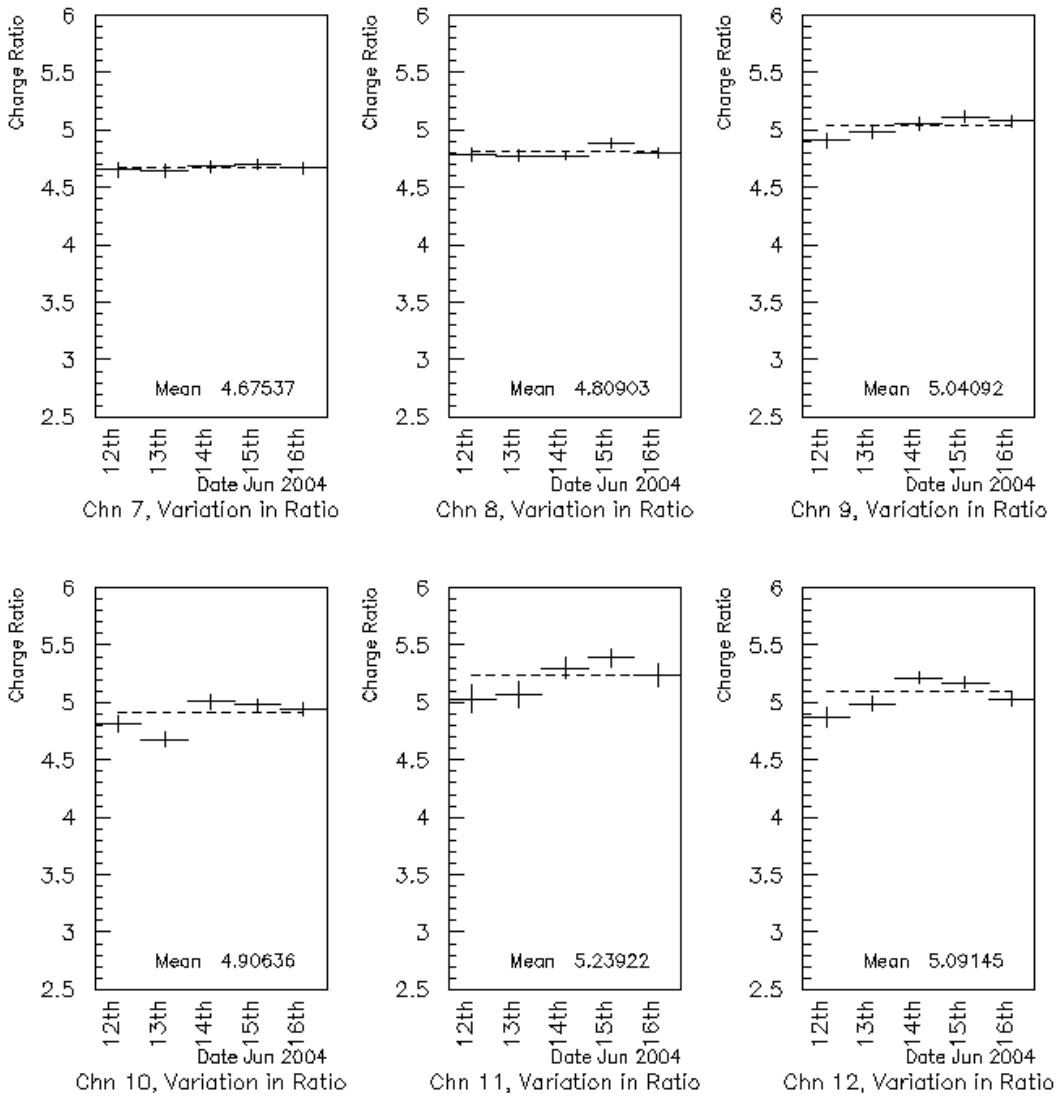

Figure E.6 Variation of the Ratio ($\langle r_j \rangle_n$) of integrated Whipple charge to the SGARFACE charge, over 5 days of observation, for channels 7 through 12. The average ratio over the five days is displayed in the plots.

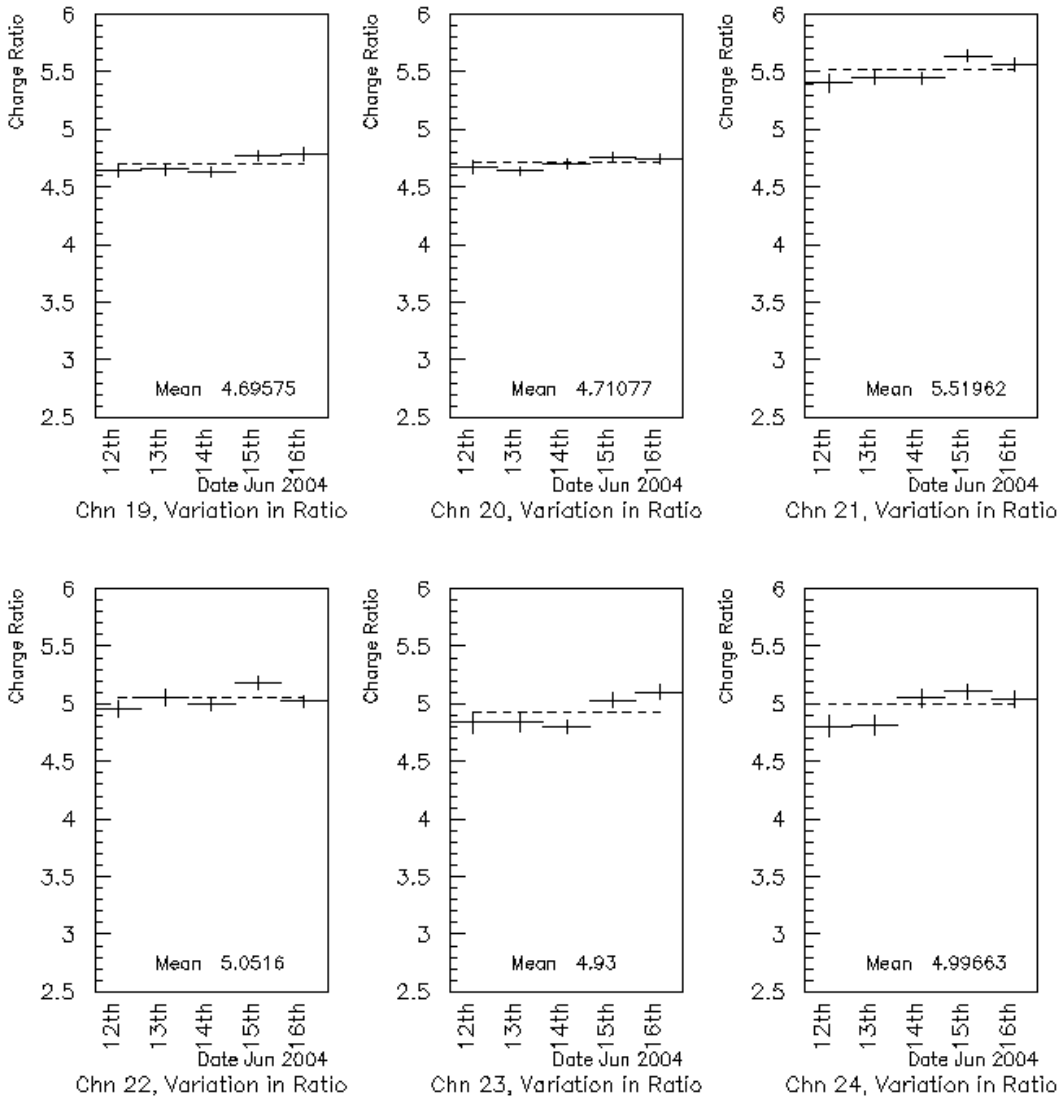

Figure E.7 Variation of the Ratio ($\langle r_j \rangle_n$) of integrated Whipple charge to the SGARFACE charge, over 5 days of observation, for channels 19 through 24. The average ratio over the five days is displayed in the plots.

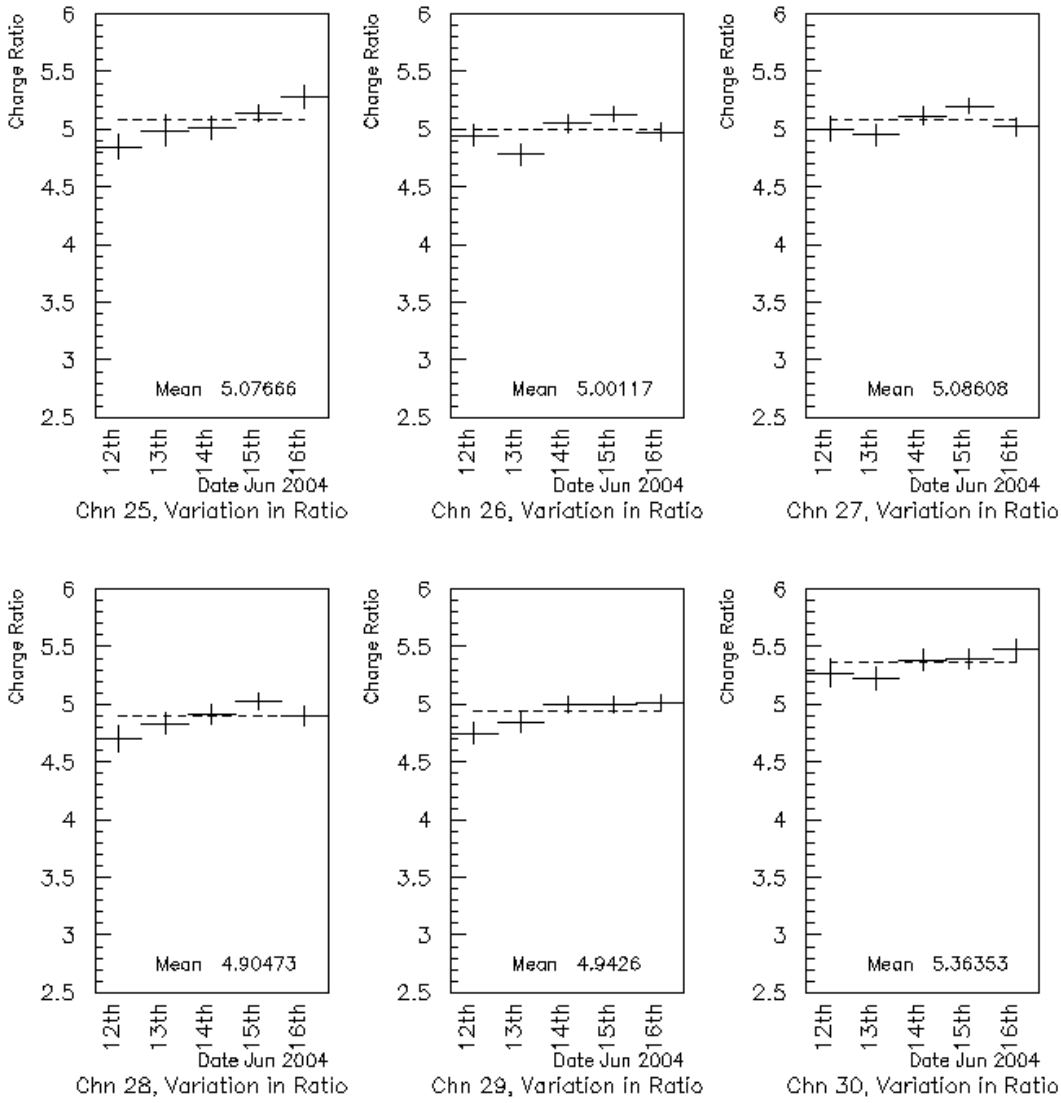

Figure E.8 Variation of the Ratio ($\langle r_j \rangle_n$) of integrated Whipple charge to the SGARFACE charge, over 5 days of observation, for channels 25 through 30. The average ratio over the five days is displayed in the plots.

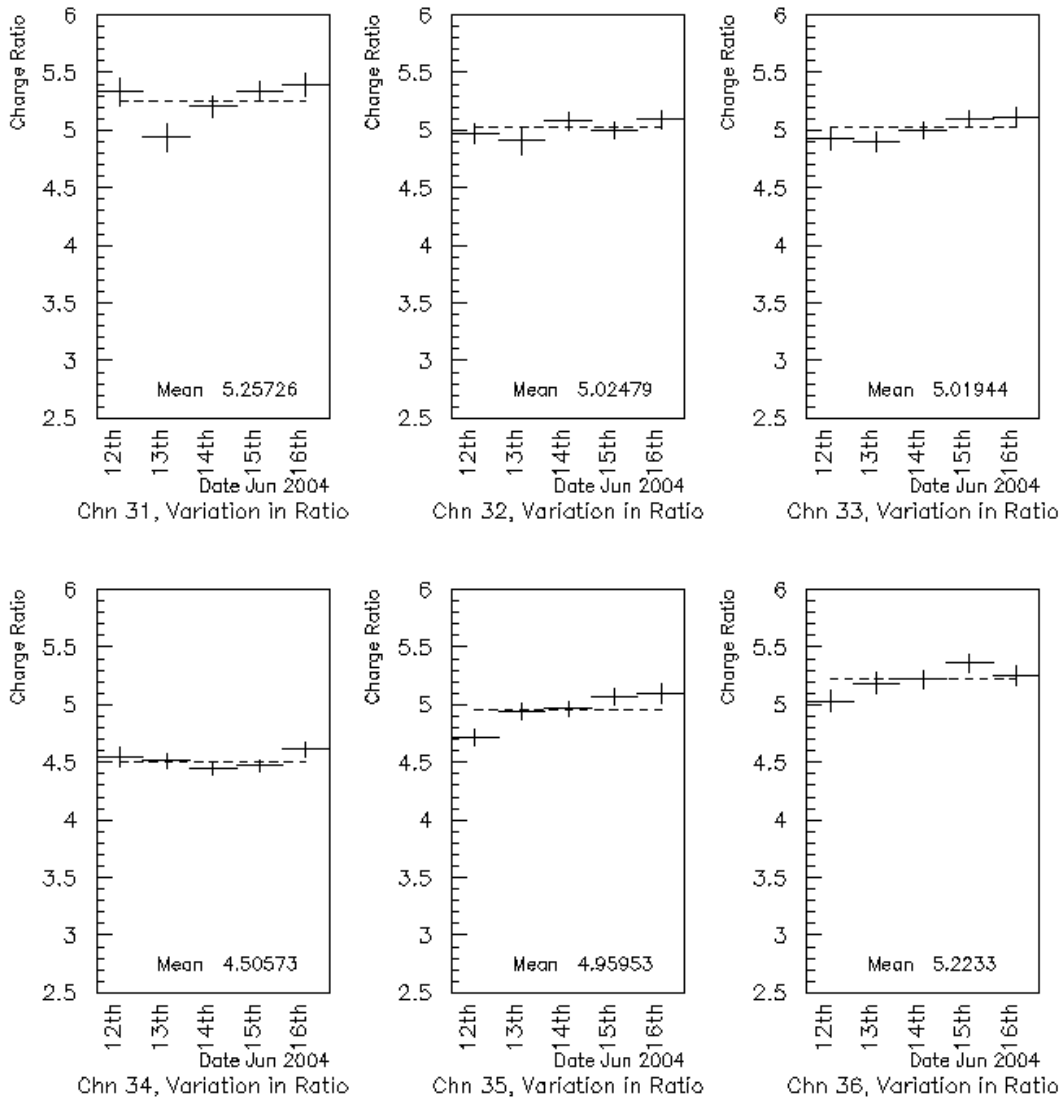

Figure E.9 Variation of the Ratio ($\langle r_j \rangle_n$) of integrated Whipple charge to the SGARFACE charge, over 5 days of observation, for channels 31 through 36. The average ratio over the five days is displayed in the plots.

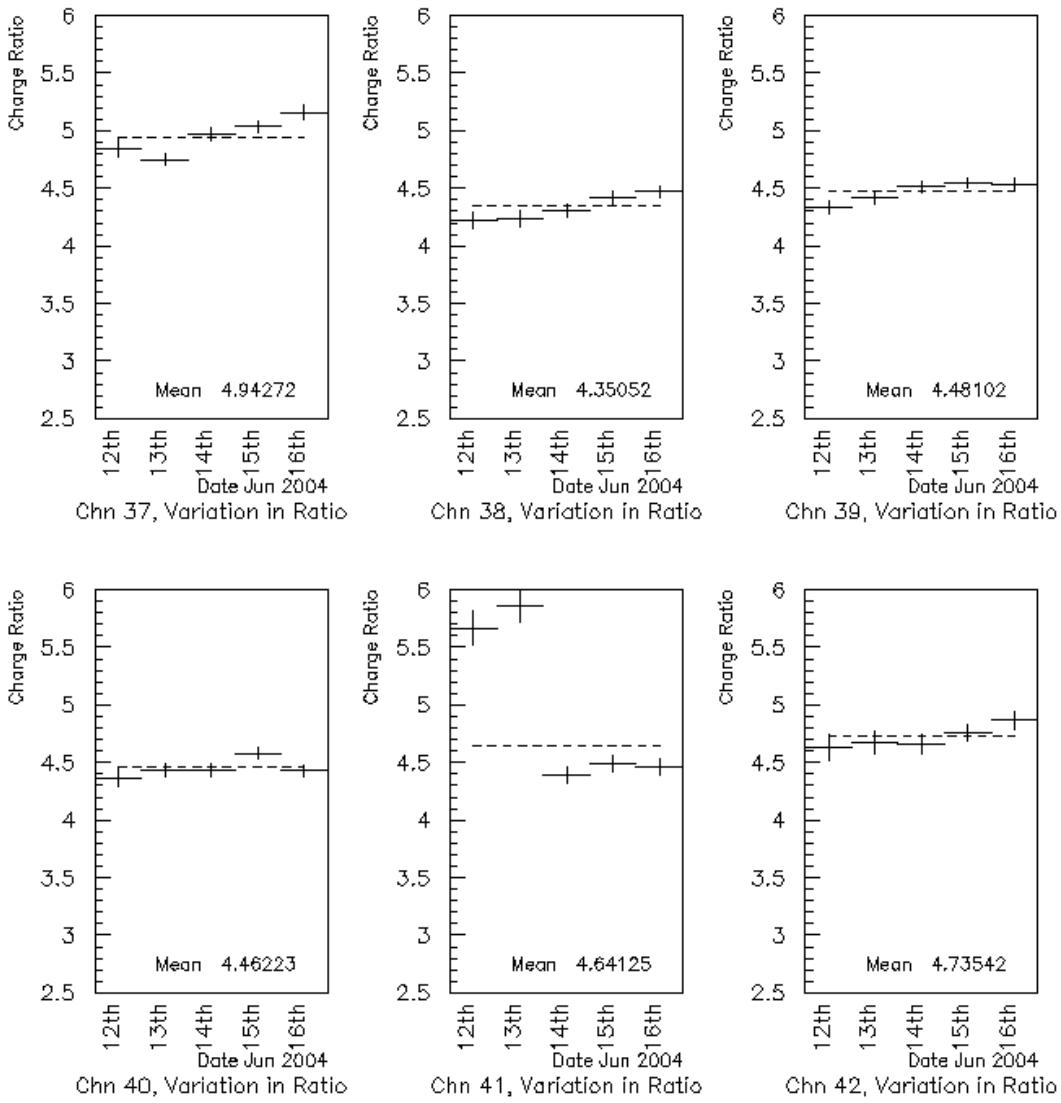

Figure E.10 Variation of the Ratio ($\langle r_j \rangle_n$) of integrated Whipple charge to the SGARFACE charge, over 5 days of observation, for channels 37 through 42. The average ratio over the five days is displayed in the plots.

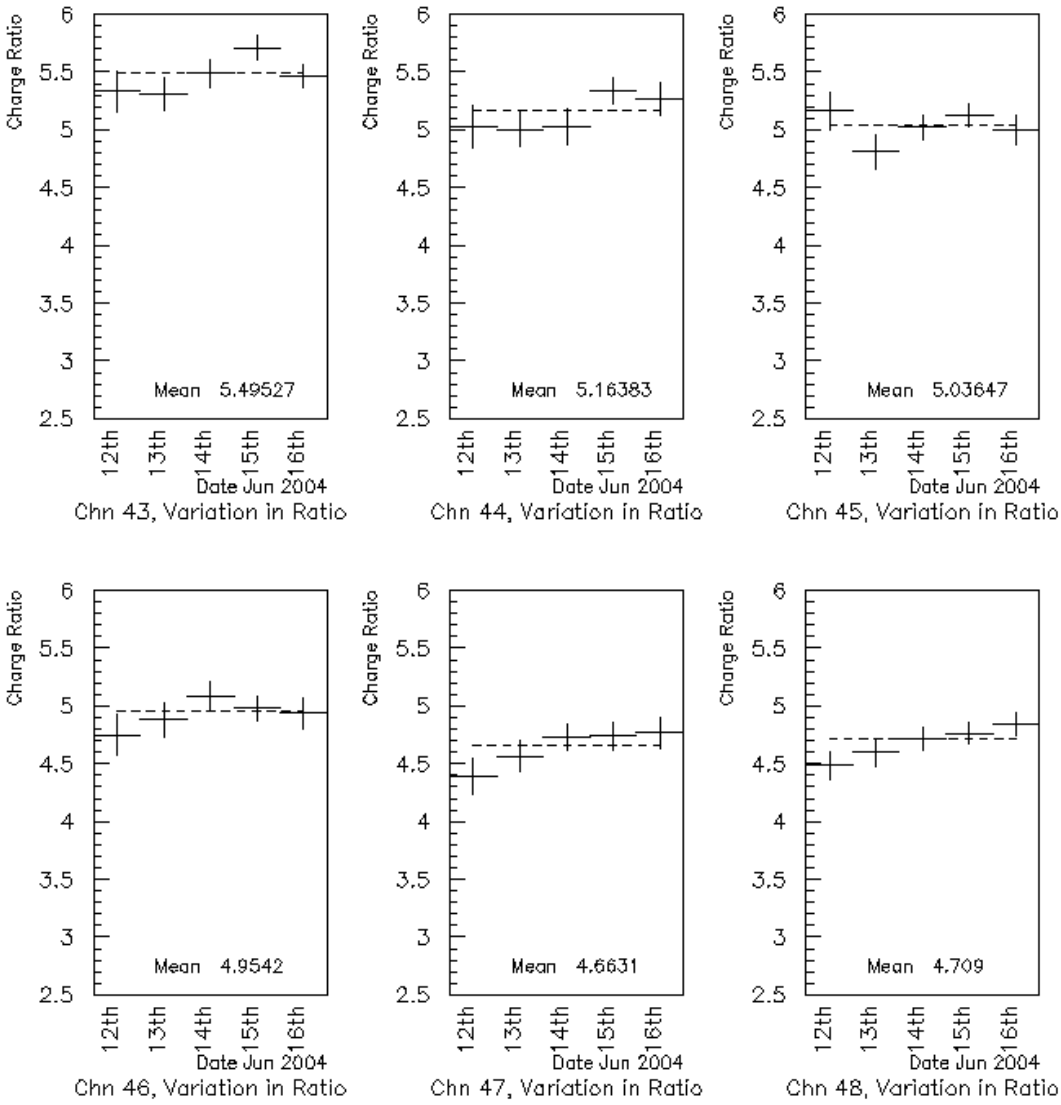

Figure E.11 Variation of the Ratio ($\langle r_j \rangle_n$) of integrated Whipple charge to the SGARFACE charge, over 5 days of observation, for channels 43 through 48. The average ratio over the five days is displayed in the plots.

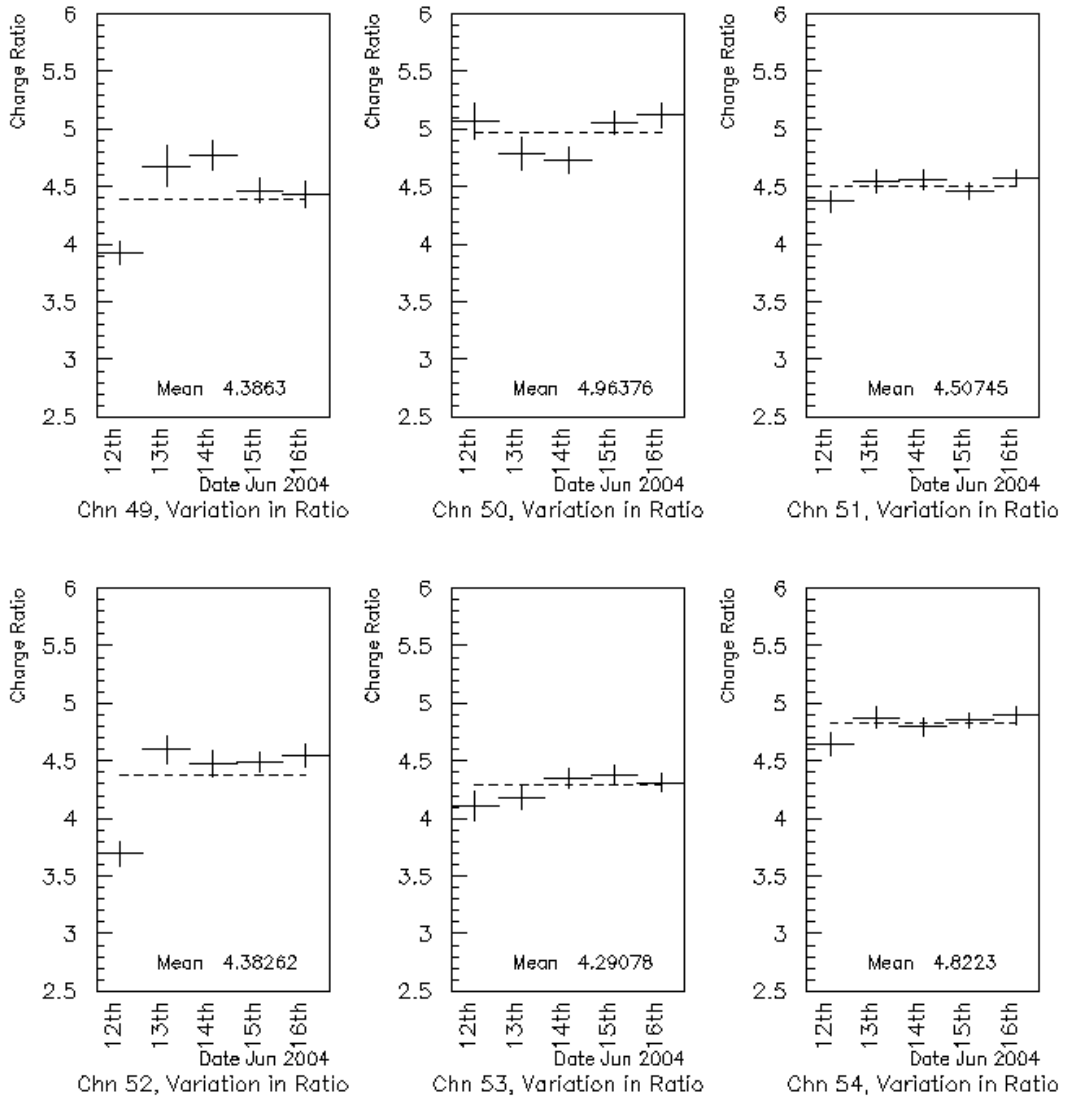

Figure E.12 Variation of the Ratio ($\langle r_j \rangle_n$) of integrated Whipple charge to the SGARFACE charge, over 5 days of observation, for channels 49 through 54. The average ratio over the five days is displayed in the plots.

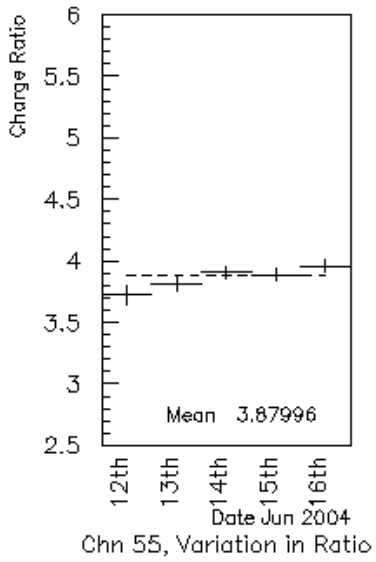

Figure E.13 Variation of the Ratio ($\langle r_j \rangle_n$) of integrated Whipple charge to the SGARFACE charge, over 5 days of observation, for channel 55. The average ratio over the five days is displayed in the plots.

BIBLIOGRAPHY

[1] C. Akerlof, R. Balsano, S. Barthelmy et al. (1999). Observation of contemporaneous optical radiation from a gamma-ray burst. *Nature*, *398*, 400.

[2] D. E. Alexandreas et al. (1993). A new limit on the rate-density of evaporating black holes. *Proceedings of the 24th ICRC (Calgary)*, *1*, 428.

[3] M. Amenomori et al. (1995). Search for 10 TeV burst-like events coincident with the BATSE bursts using the Tibet air shower array. *Astron. & Astrophys.*, *311*, 919T.

[4] F. M.Cawley et al. (1990). An Automated atmospheric Cherenkov telescope for use in TeV gamma-ray astronomy. *Proceedings of the 21st ICRC (OG Sessions)*, *Vol. 4*, 258.

[5] E. L. Chupp, D. J. Forrest, P. R. Higbie (1973). Solar Gamma Ray Lines observed during the Solar Activity of August 2 to August 11. *Nature*, *241*, 333.

[6] David B. Cline, Whoopyo Hong (1996). Very short gamma-ray bursts and primordial black hole evaporation. *Astroparticle Physics*, *5*, 175-182.

[7] David B. Cline, D. A. Sanders, Whoopyo Hong (1997). Further evidence for some gamma-ray bursts consistent with primordial black hole evaporation. *ApJ*, *486*, 169-178.

[8] V. Connaughton (1998). A search for TeV gamma-ray bursts on a 1-second time-scale. *Astroparticle Physics*, *8*, 179-191.

[9] E. Costa, F. Frontera, J. Heise et al. (1997). Discovery of an X-ray afterglow associated with the γ-ray burst of 28 February 1997. *Nature*, *387*, 783.

[10] M. K. Daniel et al. (2005). Spectrum of Very High Energy Gamma-Rays from the blazar 1ES 1959+650 during Flaring Activity in 2002. *ApJ*, *V 621, 1*, pp. 169-178.

[11] S. Fegan (2003). A VHE Survey of Unidentified EGRET Sources. *Ph.D. thesis, The University of Arizona*.

[12] C. E. Fichtel et al. (1994). Search of the Energetic Gamma-ray Experiment Telescope (EGRET) for high-energy gamma-ray microsecond bursts. *ApJ*, *434*, 557-559.

[13] J. P. Finley and the VERITAS collaboration (2001). The Granite III upgrade program of the Whipple observatory. *Proceedings of the 27th ICRC (Hamburg)*, p.2827.

[14] G. J. Fishman et al. (1994). The first BATSE gamma-ray burst catalog. *ApJS*, *92*, 229-283.

[15] N. Gehrels (2004). The SWIFT γ-ray burst mission. *New Astronomy Reviews, Elsevier*, *48*, 431-435.

[16] R. Hagedorn (1970). Thermodynamics of strong interactions at high energy and its consequences for astrophysics. *Astron. & Astrophys.*, *5*, 184-205.

[17] J. P. Halpern, S. S. Holt (1992). Discovery of soft X-ray pulsations from the gamma-ray source Geminga. *Nature*, *357*, 222.

[18] F. Halzen, E. Zas, J. H. MacGibbons, T. C. Weekes (1991). Gamma rays and energetic particles from primordial black holes. *Nature*, *353*, 807.

[19] Stephen Hawking (1971). Gravitationally collapsed objects of very low mass. *MNRAS*, *152*, 75-78.

[20] S. W. Hawking (1974). Black hole explosions? *Nature*, *248*, 30.

[21] D. A. Hill, N. A. Porter (1961). Photography of Cherenkov light from extensive air showers in the atmosphere. *Nature*, *191*, 690.

[22] A. M. Hillas (1985). Cherenkov light images of EAS produced by primary gamma rays and by nuclei. *Proceedings of the 19th ICRC (Denver)*, *Vol. 3*, 445.

[23] R. I. Hulsizer, B. Rossi (1948). Search for Electrons in the Primary Cosmic Radiation. *Phys. Rev.*, *73*, 1402.

[24] C. Kouveliotou (1997). Gamma-Ray Bursts: Observations. *Sci*, *277*, 1257.

[25] R. W. Klebesadel, I. B. Strong, R. A. Olson (1973). Observations of Gamma-Ray Bursts of Cosmic Origin. *Bulletin of the American Astrnomical Society*, *5*, 322.

[26] D. A. Kniffen, C. E. Fichtel (1981). The diffuse galactic gamma radiation - The Compton contribution and component separation by energy interval and galactic coordinates. *ApJ*, *250*, 389.

[27] W. L. Kraushaar, G. W. Clark, G. P. Garmire, H. Helmken et al. (1965). Explorer XI Experiment on Cosmic Gamma Rays. *ApJ*, *141*, 845.

[28] W. L. Kraushaar, G. W. Clark, G. P. Garmire et al. (1972). High-Energy Cosmic Gamma-Ray Observations from the OSO-3 Satellite. *ApJ*, *177*, 341.

[29] F. Krennrich, S. LeBohec, T. C. Weekes (2000). Detection Techniques of Microsecond Gamma-Ray Bursts using Ground-Based Telescopes. *ApJ*, *529*, 506-512.

[30] F. Krennrich et al. (2001). Cutoff in the TeV energy spectrum of Markarian 421 during strong flares in 2001. *ApJ*, *560*, L45-L48.

[31] F. Krennrich et al. (2004). VERITAS: the Very Energetic Radiation Imaging Telescope Array System. *New Astronomy Reviews, Elsevier*, *48*, 345-349.

[32] S. LeBohec, F. Krennrich, G. Sleege (2005). SGARFACE: a novel detector for microsecond gamma ray bursts. *Astropart. Phys.*, *23(2005)*, 235-248.

[33] S. Lebohec,P. Jordan, F. Krennrich, D. Carter-Lewis, G. Sleege (2001). A multi-time-scale trigger to search for sub-millisecond burst phenomena. *Proceedings of ICRC 2001.*

[34] S. Lebohec, F. Krennrich (2001). Short GAmma Ray Front Air Cherenkov Experiment. *Proceedings of ICRC 2001*, *Vol 1.*

[35] S. Lebohec, F. Krennrich, Gary Sleege (2003). Toward Ultra Short Gamma Ray Burst Ground Based Detection, SGARFACE status. *The universe viewed in gamma-rays, University of Tokyo Symposium*, p451.

[36] M. D. Leising, G. H. Share (1990). The gamma-ray light curves of SN 1987A. *ApJ*, *357*, 638.

[37] G. Mohanty (1995). The properties of Very High Energy gamma ray sources observed using the air Cherenkov technique. *Ph.D. thesis, Iowa State University.*

[38] W. A. Mahoney, J. C. Ling, W. A. Wheaton, A. S. Jacobson (1984). HEAO 3 discovery of Al-26 in the interstellar medium. *ApJ*, *286*, 578.

[39] J. E. McEnery, I. V. Moskalenko, J. F. Ormes (2004). GLAST: Understanding the High Energy Gamma-Ray Sky. *2004 Cgrs. Conf.*, *361M.*

[40] J. E. McEnery, W. B. Atwood, S. W. Digel, T. H. Burnett (2004). The GLAST Large Area Telescope. *American Astronomical Society Meeting 205*, *#06.07.*

[41] Rene A. Ong (1998). Very high-energy gamma-ray astronomy. *Physics Reports*, *305*, 93-202.

[42] G. J. Perlow, C. W. Kissinger (1951). Cosmic Ray Measurements in Rockets. *Phys. Rev.*, *81*, 552.

[43] N. A. Porter, T. C. Weekes (1978). A search for high energy gamma-ray bursts from primordial black holes or other astronomical objects. *MNRAS*, *183*, 205-210.

[44] F. G. Rest, L. Reiffel, C. A. Stone (1951). Note on Soft Gamma-Component of Cosmic Rays. *Phys. Rev.*, *81*, 894.

[45] Volker Schönfelder (2001). The Universe in Gamma Rays. *Astronomy and Astrophysics Library, Springer (http://www.springer.de/phys/).*

[46] M. Schroedter (2004). The very high energy gamma ray spectra of AGN. *Ph.D. thesis, The University of Arizona*.

[47] M. Schroedter, B. Behera, F. Krennrich, S. LeBohec, H. Manseri. (2005). Cross-Calibration between the Light Level Measured with SGARFACE. and the Whipple 10 m Telescope. *Proceedings of the 29th ICRC Pune (2005)*, *Vol. 3*, 445.

[48] M. Vargas, J. Paul, A. Goldwurm et al. (1997). Sigma Observations of High Energy Steady Sources and Transients in the Milky Way. *Proc. of 2nd INTEGRAL workshop (St. Mayo)*, *ESA-SP-382*, 129.

[49] Andreas von Kienlin et al. (2004). The GLAST burst monitor. *Proceedings of the SPIE*, *Volume 5488*, pp. 763-770.

[50] T. C. Weekes et al. (1972). A search for discrete sources of cosmic gamma rays of energy $10^{11} - 10^{12}$ eV. *ApJ*, *174*, 165-179.

[51] T. C. Weekes, R. F. Cawley, D. J. Fegan et al. (1989). Observations of TeV gamma rays from the Crab nebula using the atmospheric Cerenkov imaging technique. *ApJ*, *342*, 379-395.

[52] T. C. Weekes (2003). Very High Energy Gamma-Ray Astronomy. *Institute of Physics Publishing*.